JOURNAL OF APPLIED PHYSICS

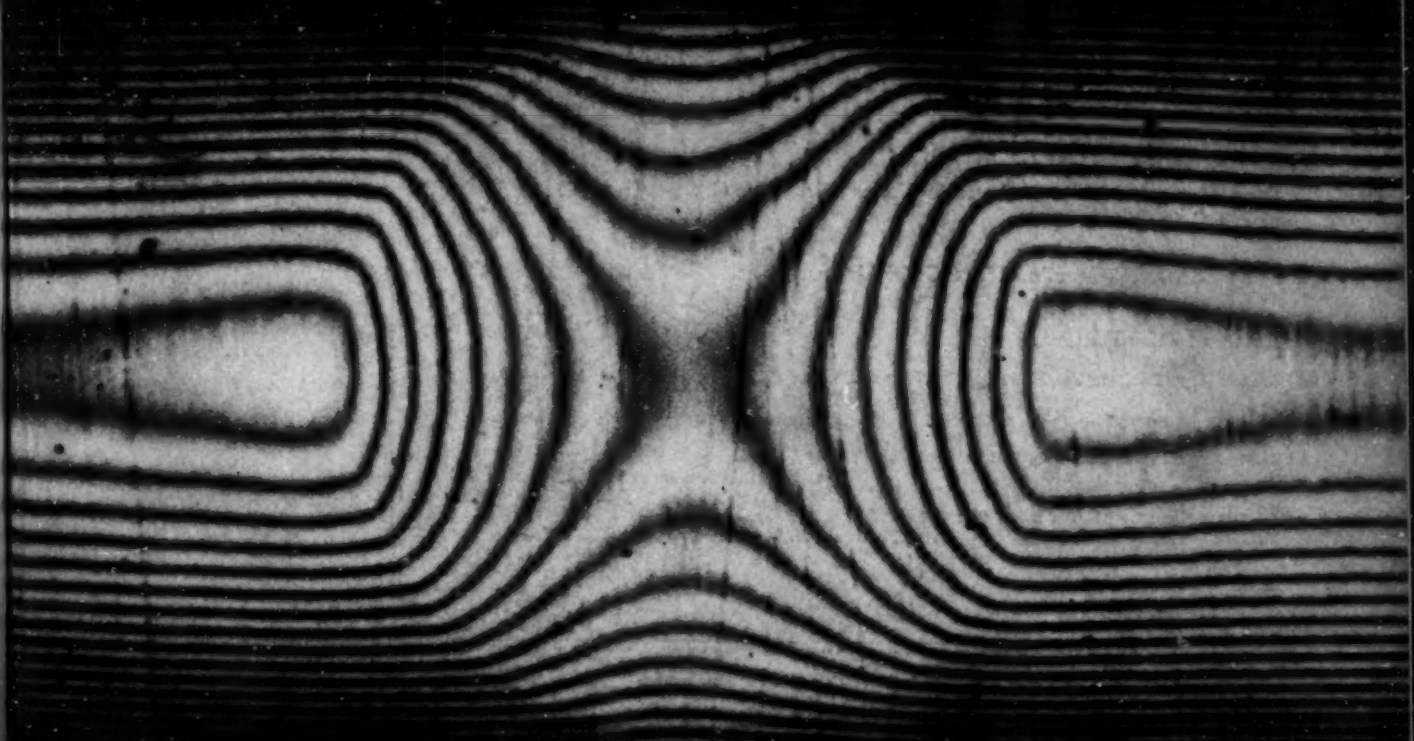

JOURNAL OF APPLIED PHYSICS

Vol. 20, No. 9 SEPTEMBER, 1949

In This Issue

Page

Aerodynamics of Golf Balls JOHN M. DAVIES 821

Projection of Crystal Structure Factors on the Reciprocal Lattice DAN MCLACHLAN, JR. AND C. L. CHRIST 829

Antennas and Open-Wire Lines. Part I. Theory and Summary of Measurements RONOLD KING 832

Potential Functions for a Thermionic Vacuum Tube E. C. OKRESS 850

Application of Thermodynamics to Chemical Problems Involving the Oxide Cathode ADDISON H. WHITE 856

Time Constants for Vacuum Gage Systems S. A. SCHAAF AND R. R. CYR 860

Generalization of Nyquist's Stability Criteria A. VAZSONYI 863

Comment on Dr. Vazsonyi's Paper, "A Generalization of Nyquist's Stability Criteria" S. J. MASON 867

Propagation of Electromagnetic Waves in a Tube Containing a Coaxial D.C. Discharge PHILIP ROSEN 868

Magnetically Controlled Wave Guide Attenuators THEODORE MILLER 878

Letters to the Editor:

Electron Emission and Conduction Mechanism of Oxide-Coated Cathodes R. LOOSJES AND H. J. VINK 884

Note on Some Plastic Flow Effects in Steel ORRIN H. CLARK AND ERNEST M. LYMAN 884

Interpretation of X-Ray Patterns of Cold-Worked Metal B. L. AVERBACH AND B. E. WARREN 885

Zirconium Carbide as a Thermionic Emitter R. E. HADDAD, D. L. GOLDWATER, AND F. H. MORGAN 886

Index to Advertisers xxx

BOARD OF EDITORS
ELMER HUTCHISSON, *Editor*

Associate Editors
R. BOWLING BARNES
OTTO BEECK
W. JAMES LYONS
PHILIP MORRISON
PAUL E. SABINE
RAYMOND J. SEEGER
FREDERICK SEITZ
CHARLES S. SMITH
J. R. TOWNSEND

Publication of the American Institute of Physics

OFFICERS
GEORGE R. HARRISON, *Chairman*
WALLACE WATERFALL, *Secretary*
GEORGE B. PEGRAM, *Treasurer*
JOHN T. TATE, *Adviser on Publications*

GOVERNING BOARD
LUIS W. ALVAREZ
J. W. BEAMS
WALLACE R. BRODE
E. U. CONDON
W. F. FAIR, JR.
HARVEY FLETCHER
GEORGE R. HARRISON
W. V. HOUSTON
PAUL KIRKPATRICK
PAUL E. KLOPSTEG
F. W. LOOMIS
PHILIP M. MORSE
J. R. OPPENHEIMER
GEORGE B. PEGRAM
HAROLD K. SCHILLING
JOHN T. TATE
WALLACE WATERFALL
M. W. WHITE
A. G. WORTHING

Consultant on Printing
MELVIN LOOS

ADMINISTRATIVE STAFF
HENRY A. BARTON, *Director*
THEODORE VORBURGER, *Business Manager*
RUTH F. BRYANS, *Publication Manager*
BETTY HOFSTADTER, *Office Manager*
EILEEN B. NEUBERGER, *Circulation Manager*

The JOURNAL OF APPLIED PHYSICS, published monthly at Prince and Lemon Sts., Lancaster, Pa., is devoted to physics in its role as the science basic to other natural sciences and to the arts and industries. Previous to 1937 this publication was known as PHYSICS. The JOURNAL OF APPLIED PHYSICS publishes editorials, news of physicists, and reviews, as well as technical papers of applied physics. Articles appearing in it are indexed regularly, according to their field, by Physics Abstracts, Chemical Abstracts, Engineering Index, Inc., Industrial Arts Index, etc.

Manuscripts should be submitted to Elmer Hutchisson, Editor, Case Institute of Technology, Cleveland 6, Ohio. The authors' institutions are requested to pay a **publication charge** of $4 per page which, if honored, entitles them to 100 free reprints. Instructions will be sent with galley proofs.

Subscriptions and orders for back numbers should be addressed to Prince and Lemon Streets, Lancaster, Pa. or to the American Institute of Physics, 57 East 55 Street, New York 22, N. Y.

Subscription Price	U.S. and Canada	Elsewhere
To members and associate members of the American Institute of Physics	$7.00	$ 8.00
To all others	9.00	10.00

Back Number Prices
Complete set: Vol. 1, July, 1931–Vol. 19, 1948—$140.00
Yearly back number rate: $10.00
Single copies: $1.00 each.

Changes of address should be sent to the Business Manager, American Institute of Physics; **corrected proofs** should be sent to the Publication Manager, American Institute of Physics.

Advertising rates supplied on request. Orders, advertising copy, and cuts should be sent to the American Institute of Physics.

Entered as second class matter January 22, 1937, at the Post Office at Lancaster, Pennsylvania, under the Act of March 3, 1879.
Accepted for mailing at the special rate of postage provided for in the Act of February 28, 1925, authorized May 2, 1932.

Copyright 1949, by the American Institute of Physics.

Journal
of
Applied Physics

Volume 20, Number 9 September, 1949

The Aerodynamics of Golf Balls

JOHN M. DAVIES
Akron, Ohio
(Received May 23, 1949)

The aerodynamic forces on golf balls were studied by dropping spinning balls through the horizontal wind stream of the B. F. Goodrich wind tunnel. The lift, L, and drag, D, were calculated from the drift of the balls, rotating at speeds, N, up to 8000 r.p.m. while falling through a wind stream having a velocity of 105 feet per second. For a standard dimple or mesh golf ball weighing 0.1 lb., the lift varied with the rotational speed as $L=0.064\times[1-\exp(-0.00026N)]$, with a maximum observed value of 0.055 lb. or more than half the weight of the ball. The drag increased nearly linearly from about 0.06 lb. for no spin to about 0.1 lb. at 8000 r.p.m.

For a smooth ball the lift was negative at all rotational speeds below 5000 r.p.m. Above this speed, the lift was positive but was less than for the standard ball. The drag for these balls was nearly constant at about 0.08 lb. Balls with shallower dimples than standard gave intermediate results. Driving tests were consistent with the wind tunnel results.

These results explain why a golfer cannot obtain long drives with a ball having a smooth surface and why the standard dimple or mesh surface gives him greater distance and better control of the ball.

INTRODUCTION

THE force acting on a sphere or cylinder rotating in a wind stream about an axis perpendicular to the stream is generally not in the direction of the wind. It may be resolved into two components, one in the direction of the wind and one perpendicular to the wind and to the axis of rotation. Magnus[1] and Newton[1] discussed the transverse force and gave the accepted explanation for its existence many years ago but apparently only a limited number of experimental studies have been made. Several measurements[2–8] have been made of the forces acting on rotating cylinders in air and photographs have been taken of the flow around cylinders in air[3] and in water.[9,10] The Flettner rotor ship[7] was an attempt to make a practical application of these forces. Robins[11] observed the effect of such forces on bullets fired from gun barrels curved in such a way as to produce rotation of the bullet. Maccoll[12] measured the forces on a 6-inch diameter sphere rotating at speeds up to about 1800 r.p.m. in a wind stream having velocities up to 34 feet per second.

These forces are important in many ball games, for example, baseball, tennis, and golf, but little definite information seems to be available. Measurements on non-rotating golf balls have been made at the Bureau of Standards[13] and by Derieux,[14] but in both cases relatively low velocities were used. Thomson[1] measured the difference in pressure between opposite sides of a golf ball rotating in a wind stream and showed qualitatively how the forces would affect the flight of the ball.

[1] (a) Magnus, Poggendorf's Ann. d. Physik Chemie **88**, 1 (1853); (b) Newton, Phil. Trans. **6**, 3078 (1672); (c) Rayleigh, Messenger of Math. **7**, 14 (1877); (d) Thomson, Nature **85**, 251 (1910), reviewed in Sci. Am. p. 136 (February 11, 1911); (e) Goldstein, *Modern Developments in Fluid Dynamics* (Oxford University Press, New York, 1938), Vol. 1, p. 83; (f) Prandtl, Tietjens, and den Hartog, *Applied Hydro and Aeromechanics* (McGraw-Hill Book Company, Inc., New York, 1934), first edition, pp. 82–85.

[2] (a) Lafay, Rev. Mécanique **30**, 417 (1912); (b) Int. Crit. Tab. **1**, 408 (1926).

[3] (a) Reid, N.A.C.A. Tech. Note 209 (1924); (b) see reference 2(b); (c) see reference 1(e), Vol. 2, p. 545.

[4] (a) Betz, Zeits. des Vereines deutscher Ingenieure **69**, 11 (1925); (b) see reference 1(e), Vol. 2, p. 545.

[5] Thom, Brit. Aero. Res. Comm. Rep. and Memo. No. 1018, Annual Reports 1925–26, p. 82 (1927).

[6] Acheret, Zeits. f. Flugtech. Motorluftschiffahrt **16**, 45 (1925).

[7] Flettner, Zeits. f. Flugtech. Motorluftschiffahrt **16**, 52 (1928).

[8] Thom, Brit. Aero. Res. Comm. Rep. and Memo. No. 1082, Annual Reports 1926–27, p. 66 (1928).

[9] See reference 1(f) pp. 281–287.

[10] Relf and Lavender, Brit. Aero. Res. Comm. Rep. and Memo. No. 1009, Annual Reports 1925–26, p. 74 (1927).

[11] Robins, "New principles of gunnery," p. 206 (1805); presented before the Royal Society in 1747, discussed in reference 15(d).

[12] (a) Maccoll, J. Roy. Aeronautical Soc. **32**, 777 (1928); (b) see reference 1(e), Vol. 2, p. 504.

[13] Unpublished results by Dr. H. L. Dryden, now at N.A.C.A.

[14] Derieux, J. Elisha Mitchell Soc. **51**, 207 (1935).

Tait[15] calculated the forces on a golf ball in flight by observing the trajectory and the time of flight and then attempted to explain the trajectory in terms of these forces. However, he had no convenient way of determining the ball velocities and, in general, the values he assumed were too high and the air forces correspondingly high but he was able to show that the transverse force had a significant effect on the trajectory.

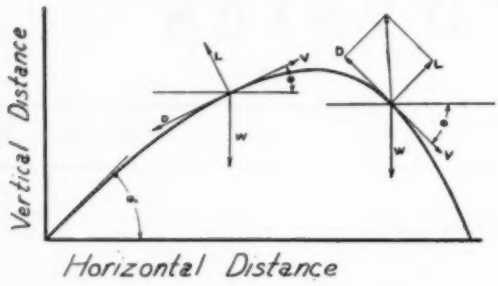

FIG. 1. Forces on a golf ball in flight.

A typical golf ball trajectory is shown in Fig. 1, with a convenient way of defining the aerodynamic forces. The total force, R, is resolved into two components, a drag, D, in the line of and opposite to the motion, and a lift, L, perpendicular to the motion. The lift is upward for the usual case of under spin and downward for over spin. Frequently the axis of rotation is not exactly horizontal and then these forces have horizontal components which cause "hooking" and "slicing." In play velocities vary over a wide range; translational velocities of more than 225 feet per second and rotational velocities up to 8000 r.p.m. have been observed at the A. G. Spalding and Brothers laboratory[16] with Edgerton's high speed photographic technique.[17] To learn more about the lift and drag under flight conditions, the motions of different types of golf balls spinning in a wind stream were studied in the B. F. Goodrich wind tunnel.

METHOD OF MEASURING LIFT AND DRAG

The spinning device is shown in Figs. 2 and 3. The ball was held between shallow cups and rotated about a horizontal axis perpendicular to the wind stream with a variable speed motor whose speed was measured with a tachometer. When the trigger was released, the springs pulled the cups apart, allowing the ball to fall freely through the wind stream.

The wind tunnel[18] is of the horizontal, open type, with the throat about 18 inches high and 36 inches wide. It was modified somewhat for these tests by adding the top and bottom sections, A and B, and a screen, as indicated in Fig. 4. The ball was rotated at C and the landing spot was marked on waxed paper at B. In some cases the ball struck the screen before falling to B and for those tests a raised platform, $\frac{1}{8}$ inch thick, was used at E. The various heights of fall were from 0.67 to 1.3 feet. The wind speed was 105 feet per second.

The motion of the ball under the action of gravity and the aerodynamic forces is indicated in Fig. 5. With no spin, the ball is pulled down by its weight and horizontally by the drag, so that it travels a horizontal distance x_0 while dropping a vertical distance y. With the ball spinning, the value of the drag is different and there is an additional vertical force, ordinarily up for clockwise rotation and down for counterclockwise rotation. This increases or decreases the rate of fall, allowing the ball to travel a horizontal distance x_1 or x_2 while falling the vertical distance y in a time t_1 or t_2. Neglecting any variation in lift and drag arising from the increase in ball velocity during fall and the variation in wind velocity throughout the testing space, the equa-

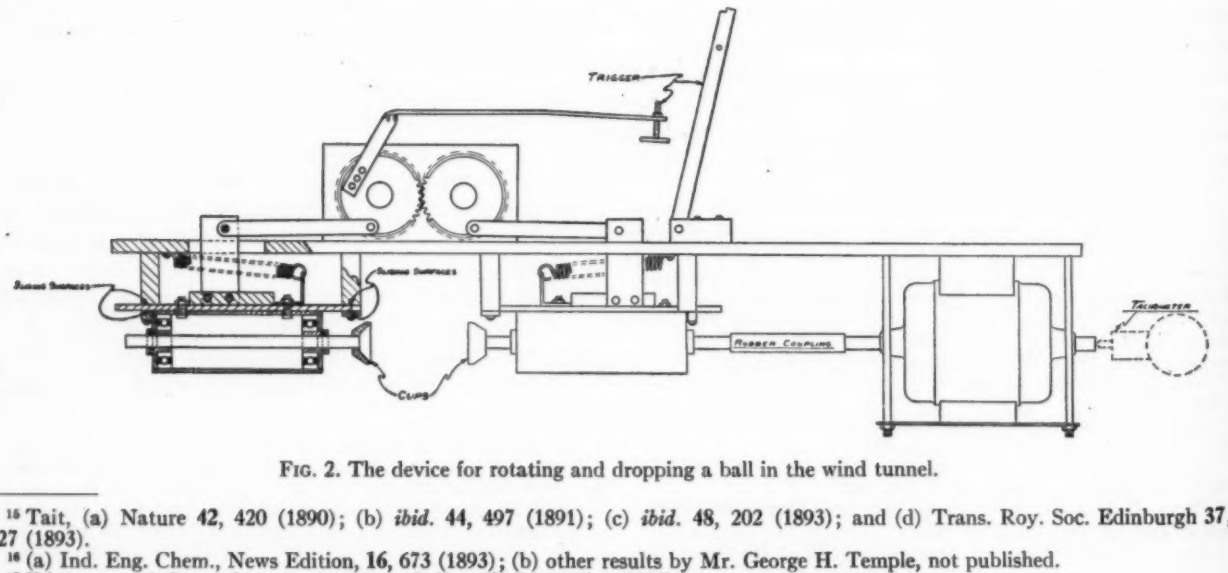

FIG. 2. The device for rotating and dropping a ball in the wind tunnel.

[15] Tait, (a) Nature **42**, 420 (1890); (b) *ibid.* **44**, 497 (1891); (c) *ibid.* **48**, 202 (1893); and (d) Trans. Roy. Soc. Edinburgh **37**, 427 (1893).
[16] (a) Ind. Eng. Chem., News Edition, **16**, 673 (1893); (b) other results by Mr. George H. Temple, not published.
[17] Edgerton and Germeshausen, American Golfer, 17 (November 1933).
[18] Geer, Aero. Eng. 4, 33 (1932).

tions of motion are:

Clockwise spin

$$(W/g)(d^2x/dt^2)=D, \quad (1)$$

$$(W/g)(d^2y/dt^2)=-W+L, \quad (2)$$

$$x_1=Dgt_1^2/2W, \quad (3)$$

$$y=-(W-L)gt_1^2/2W, \quad (4)$$

Counterclockwise spin

$$(W/g)(d^2x/dt^2)=D, \quad (5)$$

$$(W/g)(d^2y/dt^2)=-W-L, \quad (6)$$

$$x_2=Dgt_2^2/2W, \quad (7)$$

$$y=-(W+L)gt_2^2/2W, \quad (8)$$

$$D=-2Wx_1x_2/y(x_1+x_2), \quad (9)$$

$$L=W(x_1-x_2)/(x_1+x_2). \quad (10)$$

By spinning the ball first in one direction and then the other, values of the drag and lift can be obtained.

RESULTS

Some typical results are given in Fig. 6 for standard golf balls with dimple and mesh markings and for smooth balls. Each result is the average of three tests of each of two dimple or mesh balls or of four smooth balls. The dimples were spherical segments about 0.013 inch deep and $\frac{1}{8}$ inch in diameter and the mesh surface consisted mostly of approximate squares about 0.011 inch deep and $\frac{1}{8}$ inch wide. The smooth balls were standard with the exception that the covers were applied in a highly polished smooth mold. All the balls were very close to the standard diameter, 1.68 inches, and weight, 1.62 ounces.

The values for the lift and drag for the standard balls show the effects of dimple and mesh markings to be very similar. This might be expected as a result of experience in play. The values for the lift fall close to the curve represented by the equation

$$L=0.064[1-\exp(-0.00026N)], \quad (11)$$

where N is the rotational speed in r.p.m. and L is the lift in pounds. At the higher rotational speeds, the lift was just about half the weight of the ball. The drag increased nearly linearly from about 0.06 lb. at zero spin to just about the weight of the ball at 8000 r.p.m.

The most surprising result is the lift curve for the smooth ball. Up to about 5000 r.p.m., or an equatorial surface speed of 37 feet per second, the lift is negative, just opposite in direction to that expected from the Magnus effect. Above that speed it assumes the normal direction. The lift is much smaller than for the standard balls but there is an indication that at still higher rotational speeds it will be at least nearly as great. The drag of the smooth ball changes very little with change in rotational speed; above 4000 r.p.m. it is less than that of the standard balls.

In Fig. 7 smooth and standard balls are compared with a ball with intermediate marking, i.e., shallower dimples with rounded edges. Each result is the average of five tests on one ball. The results on the smooth ball agree roughly with those of the previous test but are not as consistent. For the standard dimple ball, the lift curve is nearly identical with the previous curve, except possibly at 1000 r.p.m., but the drag curve is somewhat lower at the higher speeds. These standard balls were similar to those of Fig. 6 but the markings were slightly different. For the ball with the shallower dimples, the lift was intermediate between that of the standard and smooth balls, with the drag somewhat lower than for either. It is interesting that for a bramble ball, with reversed or protruding dimples, the lift and drag curves are nearly identical with those for the normal or recessed dimples.

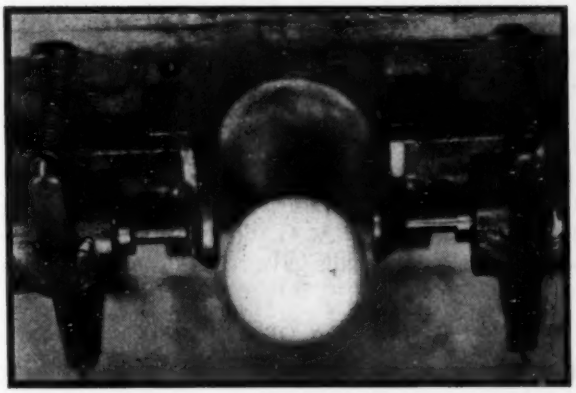

FIG. 3. Photograph of a falling ball just after release.

As a check on the validity of the method, photographs were obtained of the ball paths. The camera shutter was set for an exposure of one-fifth to one-half second and was opened by a solenoid tripped by the dropping mechanism. Figures 8, 9, and 10 show comparisons of the paths for standard and smooth balls. The paths are essentially straight and the directions are in agreement with the other tests.

DRIVING TESTS

Driving tests on smooth balls are consistent with the wind tunnel results. The B. F. Goodrich driving machine consists essentially of a mallet-type club, rotated about a horizontal axis by a motor. The club speed and face angle can be varied. The results plotted in Fig. 11 were obtained with the smooth and standard balls for which the wind tunnel results are given in Fig. 7.

Each result is the average of six dimple balls or of three smooth balls. The distance is the carry or the horizontal distance from the tee to the spot where the ball struck the ground. The roll was not measured. The measurement of trajectory height was rather arbitrary, the figures representing the apparent maximum angle

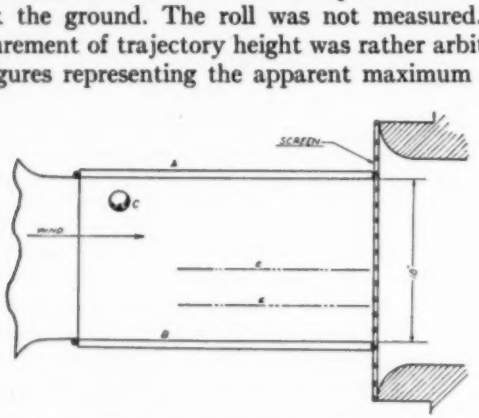

FIG. 4. Diagram of the wind tunnel, showing the location of equipment.

of the ball observed from a point about ten feet directly above the tee.

For the standard balls, the carry and trajectory height increased with the club speed and varied with the club face angle in the usual manner. With the smooth balls, however, as the speed and face angle increased, the balls started out at a higher angle but curved downward more rapidly. Consequently, neither the carry nor the trajectory height changed appreciably with variation in club speed or face angle. The magnitude of the negative lift seemed to increase rapidly with linear speed of the ball.

Driving tests at the A. G. Spalding and Brothers laboratory on similar balls gave results consistent with these tests.[19]

DISCUSSION OF ERRORS

The free fall method of studying lift and drag was selected because it eliminated the uncertain corrections for the effect of the ball supports. However, the results were subject to some other errors.

The wind stream had some turbulence and was affected by the equipment in the tunnel. Pitot tube measurements showed that the variation in wind velocity throughout the testing region was, at the most, about ± 4 feet per second.

Near the end of the path, the ball velocity was appreciable and this changed the magnitude and direction of the drag and lift. Corrections for this effect are small because of the short time in this part of the path. Calculations show that for counterclockwise spin the errors tend to cancel and the path is practically straight.

Also, in its initial position, the ball is close to the top of the tunnel and the wind velocity between the ball and the top of the tunnel is increased, with a resulting vertical force on the ball.

[19] Unpublished results by Dr. J. B. Dickson at the A. G. Spalding Brothers, Inc., Laboratory.

The dropping mechanism had a slight effect on the direction of fall in some cases but this was not serious. In tests with dimple balls at 5000 r.p.m. with no wind, the average path deviated from the vertical by no more than ± 0.007 feet with individual variations of no more than ± 0.014 feet, for a drop of 1.33 feet.

A combination of these effects, especially the first three, causes some curvature of the ball paths, as shown in the photographs. However, the photographs and also tests made with the landing platform at various heights show that these effects are not large. The extent of the over-all error is probably less than 10 percent.

COMPARISON WITH OTHER TESTS

For the smooth ball with no spin, the Reynolds' number is about 9×10^4 and the drag coefficient, C_D,

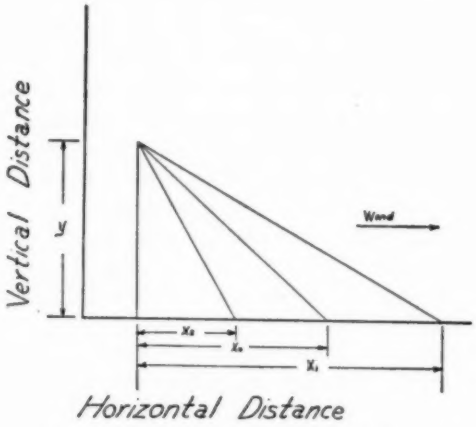

FIG. 5. Motion of a ball in the wind tunnel.

about 0.44, where C_D is defined by the equation

$$C_D = D/(\rho/2AV^2), \tag{12}$$

where V is the velocity, ρ the air density, A the projected area, and D the drag. Tests in wind tunnels having low turbulence give slightly higher values for C_D, for example, Weiselberger[20] at Göttingen found $C_D=0.48$ at this Reynolds' number. In a more turbulent air stream, the critical region where the drag coefficient decreases rapidly is reached at lower air velocities and this is a reasonable explanation for the above difference.

Apparently the only quantitative data on rotating spheres are those of Maccoll[12] at the National Physical Laboratory. Over the same range of rotational speeds, his drag and lift curves resemble those in Fig. 6, especially in showing a negative lift at low rotational speeds. The lift becomes normal in direction at equatorial speeds of about half the wind speed or less.

Negative lift has been observed also for smooth cylinders. Lafay[2] found a negative lift at surface speeds of less than half the wind speed and Reid[3] and Thom[5]

[20] See reference 1(f), p. 100.

indicated a slight negative lift at a slightly lower speed. In testing models to study the ground handling forces on airships, Knoblock and Troller[21] at the Guggenheim Airship Institute and Silverstein and Gulick[22] at Langley Field found that for certain conditions, the force on a model near a flat surface was negative.

In Derieux's experiment, a non-rotating golf ball was suspended by a thread in a horizontal wind stream at velocities of 24 to 45 feet per second and the drag determined from the angle of deflection. His data at low velocities and the present results at 105 feet per second fit the equation

$$D=23\times10^{-6}V^{1.67}. \tag{13}$$

This agreement may not be significant because unpublished results from the Bureau of Standards[13] show that the critical region for golf balls is reached at velocities of 75 to 90 feet per second and extrapolation through the critical region is not justified. It is difficult to compare the present results with the measurements at the Bureau of Standards. A velocity of 105 feet is in the critical region and in this region the drag seems to depend very much on the surface of the ball. There is a small difference in size, the ball diameter being 1.68

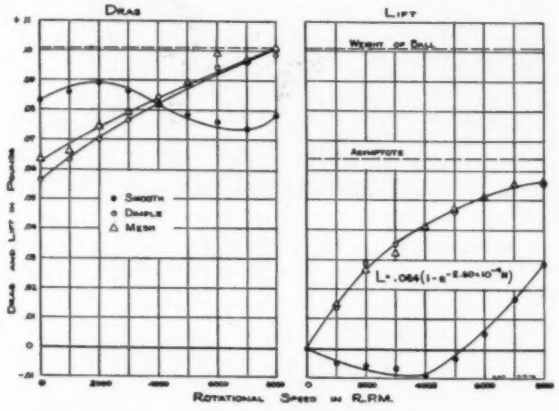

FIG. 6. Drag and lift for smooth and standard dimple and mesh balls. Wind velocity about 105 feet per second.

inches in the present case and 1.62 inches for their experiments. Interpolating their results at 105 feet per second and making allowance for this difference in size, their values of D for two different balls were 0.063 and 0.050 lb., one a little higher and the other a little lower than the present value of 0.06 lb.

It is also difficult to make a comparison with Tait's[15] results. He attempted to measure the initial ball speed and the trajectory. By assuming a particular dependence of D and L on translational speed, $D\propto V^2$ and $L\propto V$, and of L on rotational speed, $L\propto N$, he was able to calculate both forces. He was uncertain about both the translational and rotational speeds and for the most part gave his results in terms of assumed values of V. Generally these assumed values were too high and the values of D and L correspondingly high. Calculated for a velocity of 105 feet per second, his values of D are between 0.10 and 0.19 lb. and the values of L between 0.06 and 0.12 lb. Considering the possible differences in size and surface condition of the balls, the agreement is reasonably good and undoubtedly better agreement would be found by substituting accepted values for the velocities.

[21] Knoblock and Troller, Guggenheim Airship Inst. Pub. No. 2, p. 53 (1935).
[22] Silverstein and Gulick, N.A.C.A. Rep. No. 556 (1936).

DISCUSSION OF NEGATIVE LIFT

Bernoulli's theorem states that for ideal frictionless flow, along any stream line the total energy is constant, i.e.,

$$p+\rho V^2/2+\rho gh=\text{a constant}. \tag{14}$$

A qualitative explanation of the Magnus effect can be given on this basis. With the sphere rotating clockwise as in Fig. 12, the velocity at a on stream line A is higher than at b on stream line B. Since the kinetic energy is higher at a than at b, the pressure is lower at a than at b and there is a resultant upward force. The wake is deflected downward. This accounts for the experience with a rough sphere such as a standard golf ball and with a smooth sphere at high rotational speeds but not for the opposite effect with a smooth sphere at low rotational speeds.

At low velocities this situation is disturbed by friction and turbulence. With a non-rotating sphere in a wind stream, at low velocities the flow follows the surface for a short distance and then breaks away. As the velocity increases, the laminar boundary layer changes gradually into a turbulent layer and since such a turbulent layer is able to follow the surface better than

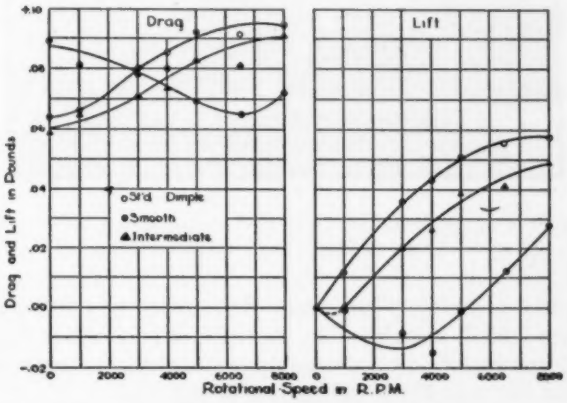

FIG. 7. Drag and lift for balls with reduced dimple depth compared with smooth and standard dimple balls. Wind velocity about 105 feet per second.

a laminar one, the breakaway point is moved in the direction of the wind stream. Relatively, the inertia forces increase faster than the frictional forces. Conditions approach those of ideal flow and there is a decrease in the drag coefficient during this transition.

These effects are illustrated by the pressure distri-

bution around a sphere, for example, the measurements by Fage[23] on a 6-inch diameter sphere at various velocities, as shown in Fig. 13. The critical range was from velocities of 50 to 95 feet per second, the curve for $V_0=35$ feet per second corresponding to nearly laminar flow and that for $V_0=135$ feet per second to

FIG. 8. Photograph of ball paths in the wind tunnel. Standard dimple ball, 8000 r.p.m. A. Clockwise. B. Counterclockwise.

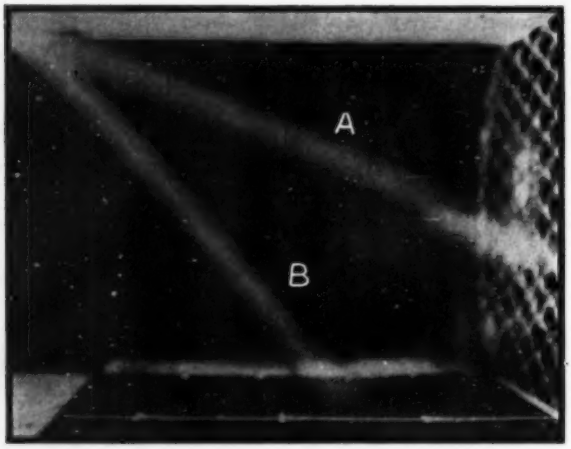

FIG. 9. Photograph of ball paths in the wind tunnel, 8000 r.p.m. clockwise. A. Dimple ball. B. Smooth ball.

nearly completely turbulent flow. Another curve has been added, calculated for the case of frictionless flow. This is based on the Bernoulli law and the assumption that the velocity at the surface is given by

$$V=\tfrac{3}{2}V_0\sin\phi, \qquad (15)$$

where V_0 is the undisturbed velocity and ϕ the angle measured from the stagnation point.[24] Below the critical region the pressures deviate considerably from the ideal curve but above the critical region the experimental curves approach the ideal case rather closely.

To a reasonable approximation, the conditions on the opposite sides of a rotating sphere may be represented by the pressure curves for a stationary sphere, using the appropriate velocities for each side. On the side rotating against the wind stream, the effective Reynolds' number is high and on the side rotating with the wind stream it is low. For low rotational speeds, the conditions at a in Fig. 12 might correspond roughly to the curve for $V_0=35$ feet per second in Fig. 13 and the conditions at b to the curve for $V_0=135$ feet per second. This analogy does not hold for the whole surface but fits fairly well in the region near $\phi=90°$ which is of most importance in determining the lift since the effec-

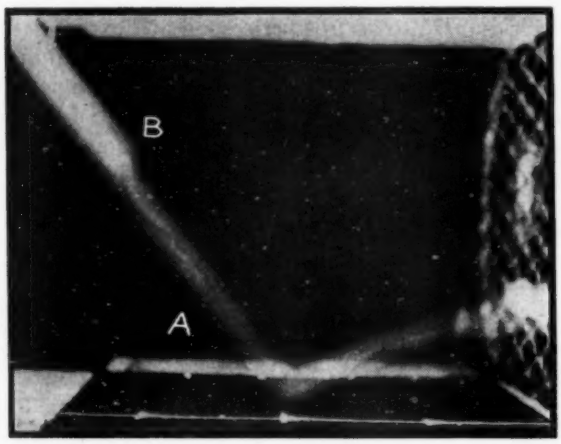

FIG. 10. Photograph of ball paths in the wind tunnel, smooth ball, 1000 r.p.m. A. Clockwise. B. Counterclockwise—rest of path cut off by short exposure.

tive vertical component of the normal pressure is high in this region. On this basis it is evident that the pressure at b is lower than at a and the transverse force will be downward or the lift is negative.

Some care is needed in arriving at this conclusion as the ordinate in Fig. 13 is the dimensionless quantity $(p-p_0)/\frac{1}{2}\rho V_0^2$ and the absolute pressure depends on the velocity. The velocity at b will be somewhat lower than

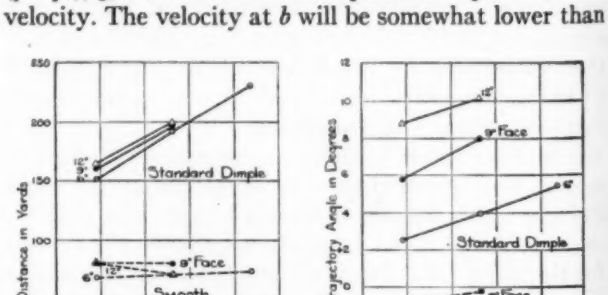

FIG. 11. Driving distances (Carry) and trajectory heights for dimple and smooth balls.

[23] (a) Fage, Brit. Aero. Res. Comm. Rep. and Memo. No. 1766 (1937); (b) see reference 1(e), Vol. 2, p. 497; (c) similar curves by Eiffel in Int. Crit. Tab. 1, 407 (1926).

[24] Milne-Thomson, *Theoretical Hydrodynamics* (MacMillan Company, Ltd., London, 1928), p. 417.

at a. The lift will be negative if the equivalent velocity for the lower side is less than 0.6 that for the upper side, positive if it is more than that.

Obviously conditions are rather critical and it would not take a very great change in the state of turbulence or velocities to reverse the direction of the resultant force. Presumably this is just what happens when the rotational surface speed becomes about half the wind speed. As the surface speed becomes higher, there may be a tendency to approach the ideal curve on both sides of the spinning sphere, but for different reasons. On the side rotating against the wind, the effective Reynolds' number becomes high; on the side rotating with the wind, with the ball surface moving faster than the wind stream, the flow follows the sphere very well and the pressures may approach the ideal curve even with a laminar boundary layer. In such a case, the direction of the resultant force would be determined by the usual Magnus explanation.

This does not explain the nature of the flow and the resulting pressure distribution but accepting that distribution, it does account for both the positive and

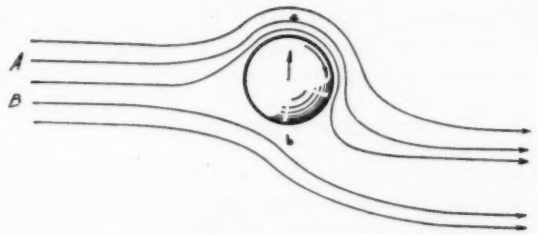

FIG. 12. Flow around a rotating sphere.

negative lift for a smooth sphere. Undoubtedly the situation would be considerably clearer if more pressure distribution data were available, for example, for a non-rotating rough sphere and for a rotating smooth sphere.

CALCULATED TRAJECTORIES

Trajectories for given typical conditions would be interesting but without additional information the calculations cannot be made with any certainty. Neither the manner in which L and D vary with translational speed nor the time rate of change of rotational speed are known. Consequently, only a few calculations have been made, for the conditions assumed in Table I, and the results are shown in Fig. 14.

The equations of motion are:

$$d^2x/dt^2 = (gD/W)\cos\theta - (gL/W)\sin\theta \qquad (16)$$

$$d^2y/dt^2 = -g - (gD/W)\sin\theta + (gL/W)\cos\theta, \qquad (17)$$

where the various terms have the meaning indicated in Fig. 1. The values of L, D and $\theta[\tan\theta = (dy/dt)/(dx/dt)]$ for the various cases were substituted in these equations and the values of x and y obtained by Moulton's method of successive approximations.[25]

[25] Moulton, *New Methods in Exterior Ballistics* (University of Chicago Press, Chicago, 1926).

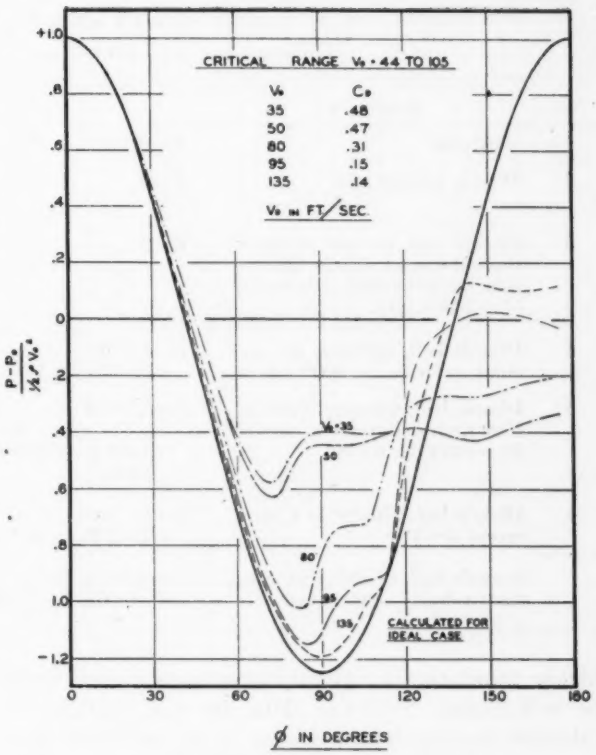

FIG. 13. Pressure distribution around a sphere in a wind stream—experimental curves by Fage.

Data for a direct check on these trajectories are not available but the results are reasonable. For all the cases, air resistance reduces the maximum theoretical carry by at least one-third. For an initial angle of 20°, the lift increases the carry appreciably even with increased drag. The effect of loss of spin is surprisingly small. The carry for the smooth balls seems to be too high, very likely because the magnitude of the negative lift increases more rapidly with linear speed than was assumed.

The forces acting on a ball at the beginning, near the middle and at the end of the flight, calculated for Case 6, are given in Table II. It is apparent that after it leaves the club, a ball is acted upon by relatively large forces. In this case, the aerodynamic forces are from one-third to more than twice the weight of the ball and with

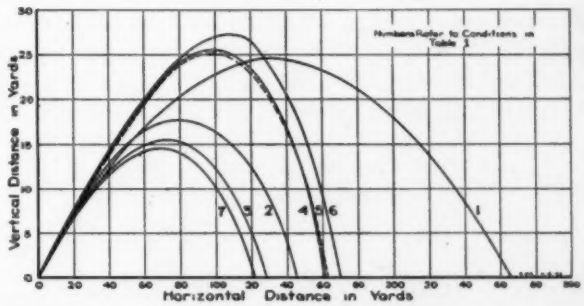

FIG. 14. Calculated golf ball trajectories.

TABLE I. Conditions for calculated trajectories.

Initial velocity, $V_0=200$ feet per second. Initial angle with horizontal $\theta_0=20^\circ$.

No.	Description	Lift	Drag
1	Ideal case	$L=0$	$D=0$
2	Dimple ball, no spin	$L=0$	$D=5.2\times10^{-6}V^2$ $=0.057$ lb. at 105 feet per second
3	Smooth ball, no spin or hypothetical case of dimple ball, no spin, but same drag as ball spinning 4000 r.p.m.	$L=0$	$D=7.5\times10^{-6}V^2$ $=0.083$ lb. at 105 feet per second
4	Dimple ball, spinning at constant velocity of 4000 r.p.m.	$L=4\times10^{-4}V$ $=0.042$ lb. at 105 feet per second	$D=7.5\times10^{-6}V^2$ $=0.083$ lb. at 105 feet per second
5	Dimple ball, spinning. Start at 4000 r.p.m., decrease at rate of 10 percent per second.	$L=6.2\times10^{-4}V$ $\times\{1-\exp[-2.6\times10^{-4}\times4000\exp(-0.1t)]\}$ $=0.042$ lb. at 105 feet per second and 4000 r.p.m.	$D=9.5\times10^{-5}V^2$ $\cdot\times[0.057+6.5\times4000\exp(-0.1t)]$ $=0.083$ lb. at 105 feet per second
6	Dimple ball. Similar to Case 4 except $D\propto V^{5/3}$	$L=4\times10^{-4}V$ $=0.042$ lb. at 105 feet per second	$D=3.54\times10^{-6}V^{5/3}$ $=0.083$ lb. at 105 feet per second
7	Smooth ball, spinning at constant velocity, 4000 r.p.m.	$L=-0.75\times10^{-4}V$ $=-0.0079$ lb. at 105 feet per second	$D=7.5\times10^{-6}V^2$ $=0.083$ lb. at 105 feet per second

higher translational and rotational speeds they would be still higher. Sufficient data are not available to calculate accurately the effects of a transverse force but such a force of 0.04 lb., resulting, for example, from rotation about an axis at an angle to the horizontal, would cause a hook or slice of roughly 50 yards in a 200 yard drive. A following, head, or transverse wind changes the trajectory appreciably. The magnitude of these lift and drag forces illustrates the extreme precision necessary for satisfactory control of a golf ball in play and, at the same time, the degree of control that can be exerted by an expert player with precise swinging.

TABLE II. Lift and drag for a calculated trajectory.

Time in seconds	Velocity, ft./sec. $\dot{y}$	$\dot{x}$	v	Distance from origin, ft. y	x	Lift lb.	Drag lb.
0	68	188	200	0	0	0.080	0.242
2.6	0	83	83	82	320	0.033	0.056
5.5	−53	55	83	0	512	0.033	0.056

ACKNOWLEDGMENTS

This work was done while the author was a member of the Physical Research Laboratory of the B. F. Goodrich Company and several members of that staff contributed to its success. The work was started under the direction of the late Dr. E. O. Dieterich and completed under the direction of Dr. W. F. Busse. Mr. S. H. Hahn designed the spinning device, Mr. Frank Herzegh took the photographs and Mr. K. B. Sherbondy helped with the experiments and calculations. Discussions with Dr. T. Troller, then of the Guggenheim Airship Institute in Akron, concerning the negative lift, were especially appreciated.

The Projection of Crystal Structure Factors on the Reciprocal Lattice

DAN MCLACHLAN, JR.
Department of Metallurgy, University of Utah, Salt Lake City, Utah

AND

C. L. CHRIST
Stamford Research Laboratories, American Cyanamid Company, Stamford, Connecticut

(Received August 3, 1948)

A discussion of the use of the wave addition method for making projections of the crystal structure factor, F_{hko}, upon the reciprocal lattice, in a fashion similar to that used in making electron density projections in real space, through the use of the "sand machine" and devices operating on similar principles, has been developed.

INTRODUCTION

IN recent years, several devices more or less specifically designed for the computation of electron densities in crystal structure analysis have been reported in the literature. These machines, all based fundamentally upon the idea of wave addition originally proposed by W. L. Bragg,[1] include the photographic method[2,3] the sand deposition method,[4] and the oscillographic method.[5] With these devices the function which is computed is of the type[1]

$$\rho(x, y)=\sum_h \sum_k |F_{hko}| \cos[2\pi(hx+ky)-\alpha_{hko}]. \quad (1)$$

The Fourier equation used for the computation of the crystal structure factor is quite analogous to that used for the computation of electron density, and has, for the centro-symmetric cell containing M atoms, the form

$$F_{hko}=\sum_{i=1}^{M} f_i \cos 2\pi(hx_i+ky_i). \quad (2)$$

By virtue of this analogy, it would seem to be of interest to inquire into the feasibility of using the machines referred to above† for the purpose of calculating structure factors, rather than electron densities. This paper presents an analysis of this problem.

ELECTRON DENSITY COMPUTATIONS

A rather general description of the nature of the wave addition involved in such devices as the "sand machine" has been given.[4] We may write, for example, for the projected electron density $\rho(x, y)'$

$$\rho(x, y)'=\sum_{h=-\infty}^{\infty} \sum_{k=-\infty}^{\infty} (S_{xy})_{hko}, \quad (3)$$

where

$$(S_{xy})_{hko}=|F_{hko}| \cos[2\pi(hx+ky)-\alpha_{hko}]. \quad (4)$$

The wave $(S_{xy})_{hko}$ is shown in projection in Fig. 1. Its wave-length λ_{hko} is precisely the interplanar spacing d_{hko}, which may be computed by Bragg's Law, or from the unit cell constants of the crystal under consideration. Using the latter, d_{hko} has, for the general case, the form

$$d_{hko}=\frac{\sin\beta}{[(h/a)^2+(k/b)^2-(2hk\cos\beta/ab)]^{\frac{1}{2}}}. \quad (5)$$

The direction of the wave front may be referred to the angle ψ_{hko}, which may be calculated from the equation

$$\psi_{hko}=\arcsin(hd_{hko}/a). \quad (6)$$

The quantities d_{hko} and ψ_{hko} may be readily determined graphically by a construction such as is given in Fig. 1. The constants d_{hko} and ψ_{hko}, the experimentally determined $|F_{hko}|$, and the phase angles α_{hko}, obtained by other means, then completely define $(S_{xy})_{hko}$.

RECIPROCAL LATTICE PROJECTIONS FROM CENTRO-SYMMETRIC STRUCTURES

For structures having a center of symmetry at the origin, and including those structures having a center of symmetry *in projection*, we may write

$$F_{hko}=2\sum_{i=1}^{M/2} f_i \cos 2\pi(hx_i+ky_i), \quad (7)$$

taking account explicitly of those atoms related by the center. The atomic coordinates x_i and y_i are now to be considered as constants fixed by the structure for which the F_{hko} are to be computed, while the Miller indices h and k are the variables. Similarly to Eqs. (3) and (4), we may write

$$F_{hko}=2\sum_{i=1}^{M/2} (\mathfrak{F}_{hko})_i, \quad (8)$$

and

$$(\mathfrak{F}_{hko})_i=f_i \cos 2\pi(hx_i+ky_i). \quad (9)$$

At this point, however, the analogy between Eqs. (4)

[1] W. L. Bragg, Zeits. f. Krist. **A70**, 475 (1929).
[2] M. L. Huggins, J. Am. Chem. Soc. **63**, 66 (1941).
[3] M. L. Huggins, J. Chem. Phys. **12**, 520 (1944).
[4] D. McLachlan, Jr. and E. F. Champaygne, J. App. Phys. **17** 1006 (1946).
[5] R. Pepinsky, J. App. Phys. **18**, 601 (1947).
† Although, by means of certain modifications, the discussion which follows may be made to apply to some of the numbered strip methods, these will not be given consideration.

and (9) is not complete. While $|F_{hko}|$ is a fixed constant independent of the real plotting area defined by x and y, f_i is not similarly independent of the reciprocal plotting area defined by h and k. This difficulty may be resolved, if the assumption is made that the atomic scattering factor curves, for the particular set of atoms involved, all have the same shape as that of some conveniently chosen reference atom. Choosing some reference atom r whose atomic scattering curve constitutes the best average of those involved in the computation at hand, we may write

$$f_r(hko)=Z_r g(hko). \tag{10}$$

Here, the left-hand member is the atomic scattering factor written explicitly as a function of hko, the function $g(hko)$ defines the shape of the scattering curve, and Z_r is the atomic number of atom r. Proceeding with the assumption that the scattering curves for the i atoms all have the same shape as that of atom r, we may write

$$f_i(hko)=Z_i g(hko), \tag{11}$$

and Eq. (9) becomes

$$(\mathfrak{F}_{hko})_i/f_r(hko)=Z_i/Z_r\cos 2\pi(hx_i+ky_i). \tag{12}$$

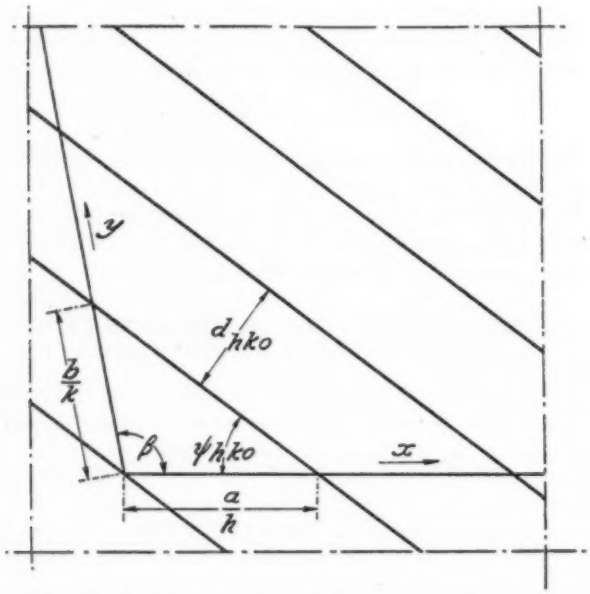

FIG. 1. Projection of the wave $(S_{xy})_{hko}$, showing the wave crests only. The symbols used have the usual crystallographic meanings: a and b are the unit cell lengths, β the interedge angle of the unit cell, d_{hko} the interplanar spacing and h and k the Miller indices. ψ_{hko} gives the direction of the wave front. For the wave shown $\alpha_{hko}=0$.

Making the definition

$$(G_{hko})_i=Z_i/Z_r\cos 2\pi(hx_i+ky_i), \tag{13}$$

then

$$F_{hko}/2f_r(hko)=\sum_{i=1}^{M/2}(G_{hko})_i. \tag{14}$$

The wave $(G_{hko})_i$ is shown in projection in Fig. 2. Comparison of this with Fig. 1 for $(S_{xy})_{hko}$ shows that a one-to-one correspondence between the two waves exists, except that the α_{hko} of $(S_{xy})_{hko}$ has no counterpart in $(G_{hko})_i$. The wave-length λ_i^* for $(G_{hko})_i$ is given for the general case by

$$\lambda_i^*=d_i^*=\frac{\sin\beta^*}{[(x_i/a^*)^2+(y_i/b^*)^2-(2x_iy_i\cos\beta^*/a^*b^*)]^{\frac{1}{2}}} \tag{15}$$

and the direction of the wave front by

$$\psi_i^*=\arcsin(x_i d_i^*/a^*). \tag{16}$$

Again, the type of construction given in Fig. 2 may be profitably employed for the graphical determination of

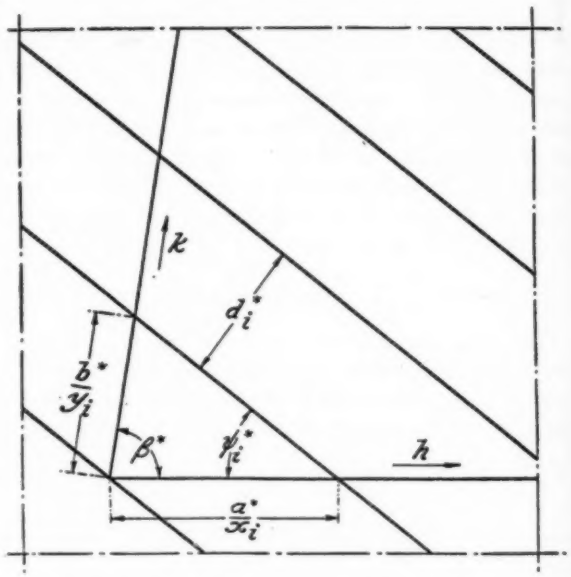

FIG. 2. Projection of the wave $(G_{hko})_i$, showing the wave crests only. The symbols used have the usual crystallographic meanings: a^* and b^* are the reciprocal cell lengths, β^* the interedge angle of the reciprocal cell, d_i^* the wave-length of $(G_{hko})_i$, and h and k the Miller indices.

d_i^* and ψ_i^*. These latter quantities, together with Z_i/Z_r then completely define $(G_{hko})_i$.

If the computation defined by Eq. (14) is carried out according to the scheme outlined above, i.e., with h and k as the continuous variables in reciprocal space, using the constants x_i and y_i for one unit cell only, such a projection will exhibit measurably large values of F_{hko} at fractional, as well as integral values of h and k. This projection will have the same distribution of F_{hko} in reciprocal space as would be given by the x-ray diffraction pattern of the crystal containing one unit cell only, if this were experimentally realizable. However, since only the values of F_{hko} at integral values of h and k are usually of concern only these need be measured.

It is at least of academic interest, however, and possibly of practical interest in considerations of very

small crystals, to investigate briefly the method for obtaining the $F_{hko}/2f_r(hko)$ projection as a function of the number of unit cells considered. Figure 3 shows a calculation of F_{hoo}/f_{Zn} for $n=1, 2, 3$, and N (very large) unit cells of $\beta-ZnS$, as a function of h. It will be noted from this figure that although the function F_{hoo}/f_{Zn} has, for n small, non-zero values at non-integral values of h, the values of F_{hoo}/f_{Zn} at integral values of h are independent of n.

Taking the above facts into consideration, we may recast Eq. (14) in the form

$$F_{hko}/2f_r(hko)=1/n\sum_{i=1}^{nM/2}(G_{hko})_i. \tag{17}$$

The summation limits are then taken to mean that the atomic coordinates of all the atoms (not related by the center of symmetry) of the n unit cells are included in the summation. An example will make this clear: consider an atom p in the unit cell containing the origin, the first unit cell; its coordinate in the x direction is x_p, while the equivalent atom in the nth unit cell along the positive x direction will have the atomic coordinate $(n-1)+x_p$. Thus, the coordinates of all the atoms involved are obtained by adding the appropriate integers (negative or positive) to the coordinates of the atoms in the first unit cell.

RECIPROCAL LATTICE PROJECTIONS FROM STRUCTURES NOT HAVING A CENTER OF SYMMETRY

The computation of the crystal structure factor for the centro-symmetric case has been given in some detail above. For those structures not having such a center, even in projection, a quite analogous treatment may be made. The crystal structure factor for the general case is given, in the present notation, by

$$F_{hko}/f_r(hko)=\sum_{i=1}^{M}(Z_i/Z_r)e^{2\pi i(hx_i+ky_i)}, \tag{18}$$

or

$$F_{hko}/f_r(hko)=\sum_{i=1}^{M}\{(Z_i/Z_r)\cos 2\pi(hx_i+ky_i) +i(Z_i/Z_r)\sin 2\pi(hx_i+ky_i)\}. \tag{19}$$

We may rewrite this as

$$F_{hko}/f_r(hko)=C(hko)+iS(hko). \tag{20}$$

The sums $C(hko)$ and $S(hko)$ may be plotted separately. Simple vector addition, on the Argand diagram, of the real and imaginary contributions to each F_{hko} will then yield $|F_{hko}|/f_r(hko)$ and α_{hko}.

GENERAL CONSIDERATIONS

So far in the discussion presented, we have neglected the fact that several of the devices under consideration[1,2,3,4] give for each wave a sinusoidal distribution which follows the law[1] (neglecting phase shifts

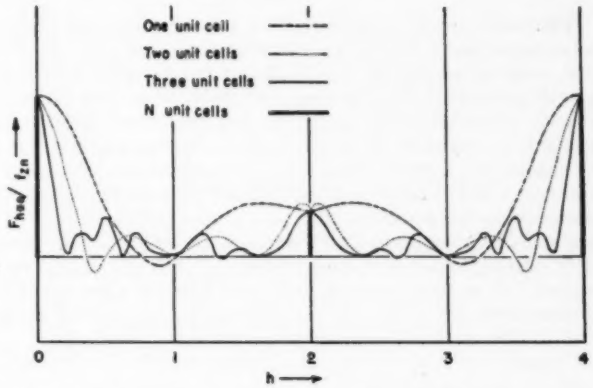

FIG. 3. F_{hoo}/f_{Zn} vs. h for $\beta-ZnS$, as a function of the number of unit cells used in the calculation.

for the electron density case)

$$|a_p|+|a_p|\left\{\begin{matrix}\sin\\ \cos\end{matrix}\right\}\theta_p, \tag{21}$$

rather than

$$|a_p|\left\{\begin{matrix}\sin\\ \cos\end{matrix}\right\}\theta_p. \tag{22}$$

For the projections under consideration, the effect of the term $\sum_p|a_p|$ is to introduce a constant background which may be quantitatively subtracted from the resulting projection.

The factors which affect the accuracy of projections of the type $\rho'(x, y)$, made with the "sand machine," have been discussed previously.[4] These same considerations apply to projections of the type presently considered, when made with this device.

It should be pointed out that, in general, the parameters x_i and y_i are irrational numbers. It is quite easy to prepare wave-length templates appropriate to these, within the necessary accuracy, for the "sand machine." It would appear that this would be less convenient in the case of the other published methods, cited above.

ACKNOWLEDGMENT

It is a pleasure to acknowledge our indebtedness to Professor A. L. Patterson for his constructive criticism of this paper.

Antennas and Open-Wire Lines. Part I. Theory and Summary of Measurements*

RONOLD KING
Cruft Laboratory, Harvard University, Cambridge, Massachusetts
(Received December 20, 1948)

Theoretical models of antennas driven by hypothetical generators are contrasted with antennas driven from transmission lines. The coupling between an antenna and a two-wire line driving it, as well as end-effects on the line, are considered in their relationship to the definition of an independent impedance for the antenna. It is concluded that a physically significant impedance can be defined only outside a terminal zone near the junction of load and line. The derivation and approximate solution of generalized transmission-line equations that take account of coupling-effects and end-effects are given for (1) antenna as end-load in the plane of a two-wire line with and without a high impedance-stub support; (2) antenna as center-load in the plane of a two-wire line symmetrically driven at each end; (3) antenna as end-load in the plane perpendicular to the line with stub support. Theoretical predictions of measured impedances defined outside a terminal zone on a feeding line in these several arrangements may differ greatly from one another and from the ratio of scalar potential difference to current for an isolated antenna with gap. These differences are due primarily to capacitive end-effects and coupling-effects of which account may be taken by a lumped positive or negative capacitance across the load terminals of an ideal transmission line. Inductive effects are also involved but are relatively small. Methods for evaluating the elements in a terminal-zone network are given. The theoretical results are verified experimentally with good agreement in all cases.

1. INTRODUCTION

THE essential quality of a radiating circuit is to maintain an electromagnetic field at distant points. Such a field is due to currents strictly in *all parts* of the circuit, but the contributions due to currents in the several parts may vary widely. In some circuits, the currents in *all* parts contribute significantly so that the entire circuit is both antenna and complete transmitting system. In others, the contributions by currents in most of the circuit may cancel and be negligible compared with the contributions from currents in a specified part, that is designated as the antenna; obviously, this part is not a complete transmitting system.

The electromagnetic energy-transfer function (defined as the integral,

$$T=\int_{\Sigma(\text{closed})} (n', \mathbf{S})d\sigma, \tag{1.1}$$

over a completely closed surface of the normal component of the real part of the Poynting vector) cannot be used to define or even locate an antenna. For, if the surface of integration, Σ, in (1.1) is progressively contracted and moved to maintain the same value of T as when Σ is a great sphere, it is *always the generator and never the antenna that is located*. The value of T when Σ encloses an antenna but not a generator (as when the antenna is driven from a two-wire line) is the net energy dissipated *in* the antenna.

Theoretical studies of the impedance of straight antennas and of its practical significance have been confused by a failure to distinguish between (1) the physical problem of an antenna as an actual circuit element in a complete system that also includes a transmission line and a generator with its coupling network, and (2) the *analytically convenient abstraction* of a rotationally symmetrical conductor that is itself a complete transmitting system by virtue of a fictitious source of e.m.f. at its center.

If an antenna is the load on a long transmission line (Fig. 1), the physically significant and practically useful impedance is measured between two rings, C and D, around the surfaces of the two conductors at a cross section far from both the generator and the load. Each of the rings is an equipotential contour, and on a balanced line the cross sections they bound are traversed by equal and opposite currents. If C and D are far from *both load and generator*, and the transmission line is straight, there is no *significant* transverse component, A_t, of the vector potential, A, along any contour t in the transverse plane containing C and D, so that the transverse electric field is given by

$$E_t=-\partial\phi/\partial t-j\omega A_t\doteq-\partial\phi/\partial t, \tag{1.2}$$

where ϕ is the scalar potential. With (1.2), the voltage across CD is defined by

$$V_{DC}=\phi_D-\phi_C\doteq\int_D^C E_t dt. \tag{1.3}$$

Only when the line integral of the electric field is sensibly equal to the scalar potential difference, as in (1.3), is it possible to introduce a unique voltage independent of the path of integration.

$$Z_{DC}=V_{DC}/I_C=V_{DC}/I_D. \tag{1.4}$$

This impedance is independent of the distant generator, so that the actual oscillator with its coupling network may be replaced by an impedance in series with a fictitious, localized e.m.f. that maintains the same voltage across CD.

* Presented, Joint Meeting, U.R.S.I.–I.R.E., Washington, D. C., May 4, 1948. Abridged from R. King, "Theory of antennas driven from a two-wire line," Cruft Lab. Tech. Rep. No. 41 (June 5, 1948). This research was supported in part by the Navy Department (ONR) and the Signal Corps, U. S. Army under Contract N5ori-76, T.O. 1.

If the antenna is assumed to be driven *at its center* by a fictitious, self-contained generator, the impedance of the antenna must be defined with respect to terminals that are a part of the generator and involve its structure and dimensions. A reasonable mathematical problem is obtained only if the properties of the generator are idealized to yield convenient boundary conditions. Two types of fictitious generators have been used: The "conducting-slice" generator shown in Fig. 2 and the "dielectric-gap" generator of Fig. 3.

The "conducting-slice" generator is an e.m.f. concentrated at the center of a continuous, straight conductor or at the base of half of this conductor erected vertically on an infinite, perfectly conducting plane. It is the impedanceless and dimensionless generator familiar to electric circuit analysis. Since the conductor is unbroken, the e.m.f. must be maintained by forces acting from the *outside*, much as in a conventional alternator in which part of a continuous conductor is in a varying magnetic field. In practice, such forces can be maintained only along finite sections of the conductor, and it is in assuming a potential difference maintained across an infinitely thin ring or belt that the physically possible is violated to achieve mathematical simplicity. Impedances for cylindrical antennas driven essentially by this type of fictitious generator are given in the literature.[1-3] It is shown later that the impedance seen by a "conducting-slice" generator can be determined *experimentally*, and hence given operational significance, by measuring the physically meaningful impedance defined in (1.4) for a number of different spacings of a two-wire line and then extrapolating these results to zero line-spacing.

In the "dielectric-gap" generator the fictitious e.m.f. is across a dielectric gap between the halves of the antenna or between a vertical antenna and an infinite, perfectly-conducting, horizontal plane. This voltage is assumed to be maintained by *rotationally symmetrical* forces *within* the gap. In practice, a voltage can be maintained across a dielectric gap only by an externally attached transmission line, since generators built inside the antenna must be connected to its terminals by current-carrying conductors *which cross the gap*. The voltage across the gap may be defined either as the line integral of the electric field along a specified path across the dielectric (Fig. 3a), or as the scalar potential difference (Fig. 3b). Since the vector potential necessarily has a non-vanishing tangential component, the two definitions are not equivalent. Infeld[4] has discussed the former definition in terms of an assumed, rotationally symmetrical field across a gap that is a physical abstraction. King and Winternitz[5] have used the latter definition in terms of scalar potential difference. Note that the ratio of voltage across the gap (using either definition) to the current into the antenna is not a physically meaningful or experimentally measurable impedance, so long as the current and voltage are due to generators with fictitious properties. However, since the ratio of scalar potential difference to current is not limited to the particular electric field and path of integration appropriate to a fictitious generator in the gap (as is the line integral of the electric field) it may be used as a boundary condition at the load point of an open-wire transmission line actually driving the antenna by maintaining this potential difference and current. This is a step in the approximate determination of the measurable impedance defined in (1.4) as carried out in the following analysis.

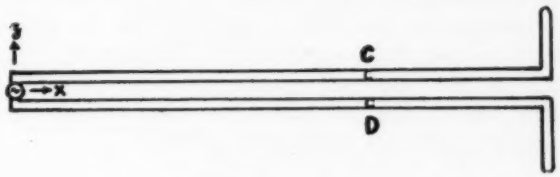

FIG. 1. Antenna driven from two-wire line.

2. TWO-WIRE TRANSMISSION-LINE THEORY; GENERALIZED EQUATIONS

The derivation of the transmission-line equations from fundamental electromagnetic theory involves assumptions and approximations that are often overlooked, but that are of great importance in the definition, the theoretical determination, and the experimental measurement of impedances terminating the line, especially if these are antennas. One method of obtaining the transmission line equations is given in the literature[6] for a two-wire line of finite conductivity immersed in an imperfect dielectric. This method does

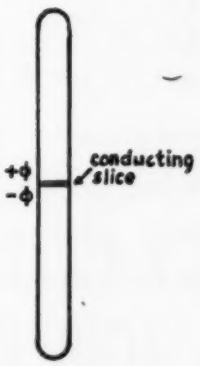

FIG. 2. Antenna with fictitious, "conducting-slice" generator maintaining a scalar potential difference.

[1] E. Hallén, "Theoretical investigations into the transmitting and receiving qualities of antennas," Nova Acta (Upsala) **11**, (November, 1938).

[2] R. King and F. G. Blake, Jr., "The self-impedance of a symmetrical antenna," Proc. I.R.E. **30**, 335–349 (1942).

[3] R. King and D. Middleton, "The cylindrical antenna, current and impedance," Quart. App. Math. **3**, 302–335 (January, 1946); pp. 200–201 (July, 1946).

[4] L. Infeld, "Influence of width of gap upon theory of antennas," Quart. App. Math., **5**, 113–132 (July, 1947).

[5] R. King and T. W. Winternitz, "Cylindrical antenna with gap," Quart. App. Math. **5**, 403–416 (January, 1948).

[6] R. W. P. King, *Electromagnetic Engineering, I*, (McGraw-Hill Book Company, Inc., New York, 1945). Chapter VI.

not separate effects due to non-uniformity of current on the line and radiation since both effects are ultimately neglected. In order to analyze conditions near the end of a line terminated in an antenna, it is necessary to take account of the non-uniformity of current.

The electromagnetic foundations of the transmission-line equations are the defining equation for the scalar potential ϕ, and the equation of continuity for potentials. If the two-wire line is parallel to the x axis in the xz plane, with the x axis midway between its two conductors, the following forms are involved:

$$E_x = z^i I_x = -\partial\phi/\partial x - j\omega A_x, \tag{2.1}$$

$$\partial A_x/\partial x + \partial A_y/\partial y + \partial A_z/\partial z + j\beta_0^2\phi/\omega = 0, \tag{2.2}$$

where z^i is the internal impedance per unit length and $\beta_0 = 2\pi/\lambda_0$. The components A_y, and A_z, and their derivatives $\partial A_y/\partial y$, $\partial A_z/\partial z$, are zero everywhere on the two conductors if *the line is infinitely long or has open ends*. A_y and A_z and their derivatives *may* differ from zero near the end of a line terminated in a coil, a straight wire, an antenna, etc., in which currents are perpendicular to the x axis. Hence, $\partial A_y/\partial y$ and $\partial A_z/\partial z$ *may not be omitted from* (*2.3*) unless shown to be zero or negligible, if the resulting equations are to be valid near the ends of the line.

Let (2.1) and (2.2) be written successively with subscripts 1 and 2 for the two conductors of the line and

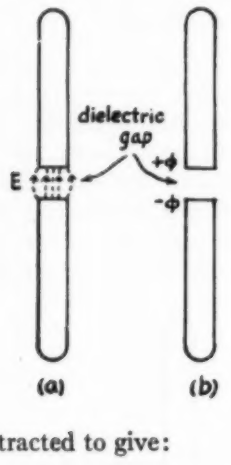

FIG. 3. Antenna with fictitious "dielectric-gap" generator maintaining in (a), a rotationally symmetrical electric field, in (b), a scalar potential difference.

subtracted to give:

$$-(\partial/\partial x)(\phi_1 - \phi_2) = z_1^i I_{1x} - z_2^i I_{2x} + j\omega(A_{1x} - A_{2x}); \tag{2.3}$$

$$-\left[\left(\frac{\partial A_x}{\partial x}\right)_1 - \left(\frac{\partial A_x}{\partial x}\right)_2\right] - \left[\left(\frac{\partial A_y}{\partial y}\right)_1 - \left(\frac{\partial A_y}{\partial y}\right)_2\right]$$

$$-\left[\left(\frac{\partial A_z}{\partial z}\right)_1 - \left(\frac{\partial A_z}{\partial z}\right)_2\right] = j\frac{\beta_0^2}{\omega}[\phi_1 - \phi_2]. \tag{2.4}$$

If the potentials and their derivatives in (2.3) and (2.4) are defined on the equipotential surfaces of identical conductors 1 and 2 with centers at $(x, 0, b/2)$, $(x, 0, -b/2)$, and the impedances terminating both ends of the line are symmetrical with respect to the xy plane, it follows that

$$z_1^i = z_2^i \equiv z^i/2, \quad I_{2x} = -I_{1x} \equiv -I_x, \tag{2.5}$$

where z^i is the internal impedance per loop unit length of the two-conductor line. The x component of the vector potential is an odd function of z calculated from

$$A_x(x) = A_x = \frac{1}{4\pi\nu_0}\int I_{x'}\frac{e^{-i\beta_0 R}}{R}dx', \tag{2.6}$$

where $R = [(x-x')^2 + (y-y')^2 + (z-z')^2]^{\frac{1}{2}}$ and $\nu_0 = 10^7/4\pi$ meters/henry. If there is a z component of current in the symmetrical termination, it must be an even function of z, and hence the z component of the vector potential must also be an even function. It follows that, $(\partial A_z/\partial z)_1 - (\partial A_z/\partial z)_2 = 2(\partial A_z/\partial z)_1$. Note that $(\partial A_z/\partial z)_{z=0} = -(\partial A_z/\partial z)_{z=0} = 0$.

For terminations that are symmetrical with respect to the xz plane as are here required, $(\partial A_y/\partial y)_1 = (\partial A_y/\partial y)_2$. For the antenna of Fig. 1, A_y and its derivatives are zero everywhere. With the notation** $V = \phi_1 - \phi_2 = 2\phi_1$; $W_x = A_{1x} - A_{2x} = 2A_{1x}$, (2.3) and (2.4) become:

$$-(\partial V/\partial x) = z^i I_x + j\omega W_x; \tag{2.7a}$$

$$-(\partial W_x/\partial x) = 2(\partial A_z/\partial z)_1 + j(\beta_0^2/\omega)V. \tag{2.7b}$$

Differentiation of (2.7a,b) and separation of variables gives

$$(\partial^2 W_x/\partial x^2) + \beta_0^2 W_x = j(\beta_0^2/\omega)z^i I_x - 2(\partial/\partial x)(\partial A_z/\partial z)_1 \tag{2.8a}$$

$$(\partial^2 V/\partial x^2) + \beta_0^2 V = -z^i(\partial I_x/\partial x) + j2\omega(\partial A_z/\partial z)_1, \tag{2.8b}$$

where

$$W_x = W_x(x) = 2A_{1x}(x)$$

$$= \frac{1}{2\pi\nu_0}\int_0^s I_x(x')\left(\frac{e^{-i\beta_0 R_a}}{R_a} - \frac{e^{-i\beta_0 R_b}}{R_b}\right)dx' \tag{2.9}$$

$$R_a = [(x'-x)^2 + a^2]^{\frac{1}{2}}; \quad R_b = [(x'-x)^2 + b^2]^{\frac{1}{2}}. \tag{2.10}$$

The length of the line is s. In expressing W_x as in (2.9) it is implied that the only significant x components of current are the currents in the transmission line itself. If there are x components of current in the terminations, these are assumed to be so oriented and arranged that the resultant contribution to A_x along the conductors of the transmission line is zero.

The z component of the vector potential in (2.8) is defined at the surface of line conductor 1. It is

$$A_z(x) \equiv A_z = \frac{1}{4\pi\nu_0}\int I_z(z')\frac{e^{-i\beta_0 R}}{R}dz', \tag{2.11}$$

** Conventional transmission-line theory arbitrarily assigns a positive direction to its current that is the opposite of that logically derived from the field equations. Hence, it is necessary to set $V = \phi_1 - \phi_2$ instead of $V = \phi_2 - \phi_1$, as is usual.

where R is the distance between a point $(x, 0, b/2)$ where the vector potential is evaluated to the element dz' at a point (x', y', z') in the termination where $I_z(z') \neq 0$.

$$V = V(x) = V_L(x) + V_T(x) \tag{2.12}$$

$$V_L(x) = \frac{j\omega}{\beta_0^2}\frac{\partial W_z(x)}{\partial x} = \frac{1}{2\pi\epsilon_0}\int_0^s q(x')\left(\frac{e^{-i\beta_0 R_a}}{R_a} - \frac{e^{-i\beta_0 R_b}}{R_b}\right)dx' \tag{2.13}$$

$$V_T(x) = \frac{j2\omega}{\beta_0^2}\left(\frac{\partial A_z}{\partial z}\right) = \frac{1}{2\pi\epsilon_0}\int q(z')\frac{e^{-i\beta_0 R}}{R}dz', \tag{2.14}$$

where $q(x')$ and $q(z')$ are the charge per unit length in the line and in the termination, respectively. With this notation, (2.8a,b) may be written as follows:

$$\frac{\partial^2 W_z(x)}{\partial x^2} + \beta_0^2 W_z(x) = j\frac{\beta_0^2}{\omega}\left[z^i I_z(x) + \frac{\partial V_T(x)}{\partial x}\right] \tag{2.15a}$$

$$\frac{\partial V(x)}{\partial x^2} + \beta_0^2 V(x) = -z^i\frac{\partial I_z(x)}{\partial x} + \beta_0^2 V_T(x). \tag{2.15b}$$

$V(x)$ is the potential difference between the wires of the line at the cross section specified by the coordinate x, due to all the charges in the line *and* in the terminations; $V_T(x)$ is that part of $V(x)$ due to the charges in the terminations alone. For a line with conductors that are sufficiently closely spaced, $V_T(x)$ is significant only over short distances near each termination. Over most of the line $V_T(x) \doteq 0$; $V(x) \doteq V_L(x)$.

Equations (2.15a,b) are integrodifferential equations for determining the current $I_z(x)$. The scalar potential difference $V(x)$ must be a solution of (2.15b), but if (2.15a) involves I_z in the terminations through $A_z(x)$, it is clear that an equation similar to (2.15a) in $A_z(z)$ and $I_z(z)$ must be obtained from the boundary conditions of the termination and solved simultaneously with (2.15a) for $I_z(x)$ in the line and $I_z(z)$ in the termination. Such an equation has been derived in the literature for an antenna.[3,5] Clearly, an *exact* solution of such a pair of simultaneous integrodifferential equations is involved.

For perfect conductors (for which $z^i = 0$) and at distances from the termination at which the terms in $A_z(x)$ are negligible, $W_z(x)$ and $V(x)$ individually satisfy the *homogeneous* wave equation with no restriction to make radiation negligible. Unlike the potential functions, $I_z(x)$ satisfies the homogeneous wave equation *only if radiation is made negligible* by imposing the following condition on the distance b between centers of the conductors of the transmission line:

$$(2\pi b/\lambda_0)^2 = \beta_0^2 b^2 \ll 1. \tag{2.16a}$$

This restriction is sufficiently severe to make radiation negligible in determining the amplitude and the distribution of voltage and current along the line even when not loaded. For a line with a load, and even for determining the approximate distribution of voltage or current on an unloaded line, (2.16a) is more severe than necessary. It is sufficient to require the average radiation resistance per loop unit length to be small compared with the inductive reactance per loop unit length. The condition is

$$\beta_0^2 b^2 \ll 4\pi \ln(b/a). \tag{2.16b}$$

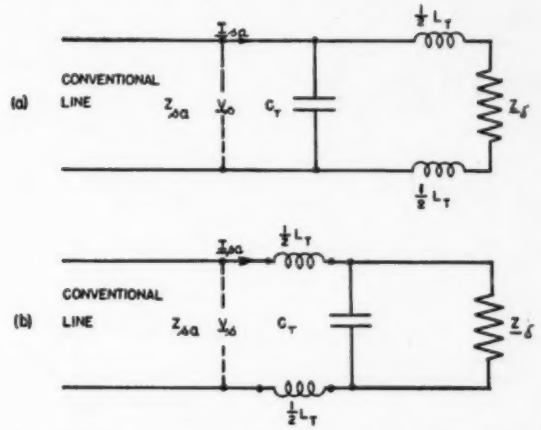

FIG. 4. Lumped networks for use with a fictitious uniform line in the terminal zone to simulate an actual line with variable parameters.

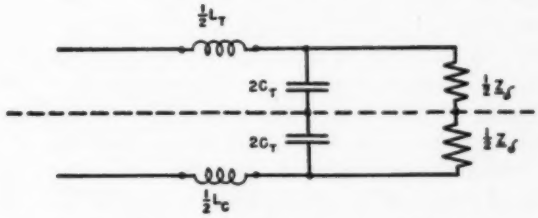

FIG. 5. Like Fig. 4b, but arranged for use with image-plane line.

Let the variables $w \equiv s - x$, $w' \equiv s - x'$ be introduced in (2.9) and (2.13). Since the contributions to $W_z(w)$ and $V(w)$ at a point w, due to currents and charges at w', are significant only for distances $(w' - w)$ that are not large compared with b, it is a good approximation to expand the current $I_z(w')$ in terms of $I_z(w)$, and the charge per unit length $q(w')$ in terms of $q(w)$, and to retain only the first two terms. Thus,

$$I_z(w') \doteq I_z(w) + (w' - w)(\partial I_z(w')/\partial w')_{w'=w} \tag{2.17}$$

$$q(w') \doteq q(w) + (w' - w)(\partial q(w')/\partial w')_{w'=w}. \tag{2.18}$$

Using the equation of continuity in the form

$$j\omega q(w) = \partial I_z(w)/\partial w, \tag{2.19}$$

the following expressions may be derived

$$W_z(w) = \frac{1}{2\pi\nu_0}[I_z(w)k_0(w) + jq(w)k_1(w)/\beta_0] \tag{2.20}$$

$$V_L(w) = \frac{1}{2\pi\nu_0}\left[q(w)k_0(w) + \frac{k_1(w)}{j\omega\beta_0}\frac{d^2 I_z(w)}{dw^2}\right], \tag{2.21}$$

where

$$k_0(w)\equiv\int_0^s\left(\frac{1}{R_a}-\frac{1}{R_b}\right)dw'+\int_0^a\left(\frac{e^{-j\beta_0R_a}-1}{R_a}-\frac{e^{-j\beta_0R_b}-1}{R_b}\right)dw' \quad (2.22a)$$

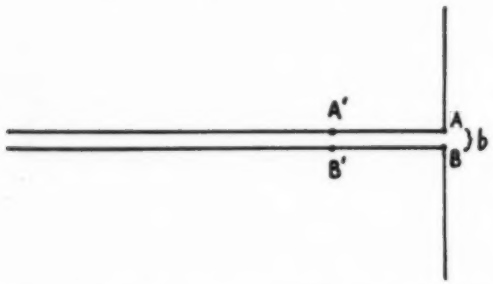

FIG. 6. Measurable impedance must be defined at $A'B'$, not at AB.

$$k_1(w)\equiv\beta_0\int_0^s(w'-w)\left(\frac{1}{R_a}-\frac{1}{R_b}\right)dw'+\beta_0\int_0^s(w'-w)\times\left(\frac{e^{-j\beta_0R_a}-1}{R_a}-\frac{e^{-j\beta_0R_b}-1}{R_b}\right)dw'. \quad (2.22b)$$

The second integrals (2.22a) and (2.22b) take account of radiation. They are negligible when $(w'-w)$ is large compared with b since then $R_a\doteq R_b$. On the other hand, when $(w'-w)$ is of the order of magnitude of small multiples of b or less, β_0R_a and β_0R_b are necessarily small compared with unity if (2.16a) is satisfied. If the exponentials are expanded in series, all terms below those of third power cancel. Hence, subject to (2.16a), these integrals, and with them radiation, are always negligible compared with the first integrals in (2.22a) and (2.22b). These latter are readily evaluated as follows:

$$k_0(w)=\sinh^{-1}\frac{w}{a}-\sinh^{-1}\frac{w}{b}+\sinh^{-1}\frac{x}{a}-\sinh^{-1}\frac{x}{b} \quad (2.23)$$

$$k_1(w)=\beta_0[(w^2+b^2)^{\frac{1}{2}}-(w^2+a^2)^{\frac{1}{2}}-(x^2+b^2)^{\frac{1}{2}}+(x^2+a^2)^{\frac{1}{2}}]. \quad (2.24)$$

The greatest value of $k_1(w)/k_0(w)$ is for $w=0$. Subject to (2.16a) or (2.16b),

$$p^2(w)\equiv\frac{k_1^2(w)}{k_0^2(w)}\leqq\frac{k_1^2(0)}{k_0^2(0)}=\frac{\beta_0^2(b-a)^2}{[\ln b/a]^2}. \quad (2.25)$$

Let the following symbolism be introduced:

$$l_0^e(w)\equiv\frac{k_0(w)}{2\pi\nu_0};$$

$$l_0^e\equiv[l_0^e(w)]_{w^2\gg b^2}=\frac{1}{\pi\nu_0}\ln\frac{b}{a} \quad (2.26)$$

$$c_0(w)\equiv\frac{2\pi\epsilon_0}{k_0(w)};$$

$$c_0\equiv[c_0(w)]_{w^2\gg b^2}=\frac{\pi\epsilon_0}{\ln(b/a)} \quad (2.27)$$

$$R_c(w)\equiv\left[\frac{l_0^e(w)}{c_0(w)}\right]^{\frac{1}{2}}=\frac{\zeta_0}{2\pi}k_0(w);$$

$$R_c\equiv\left(\frac{l_0^e}{c}\right)^{\frac{1}{2}}=\frac{\zeta_0}{\pi}\ln\frac{b}{a}. \quad (2.28)$$

Note that $\zeta_0=1/(\nu_0\epsilon_0)^{\frac{1}{2}}=376.7$ ohms and that

$$v_0\equiv\left(\frac{\nu_0}{\epsilon_0}\right)^{\frac{1}{2}}=\frac{1}{[l_0^e(w)c_0(w)]^{\frac{1}{2}}}=\frac{1}{[l_0^ec_0]^{\frac{1}{2}}} \quad (2.29)$$

$$\beta_0\equiv\frac{\omega}{v_0}=\omega[l_0^e(w)c_0(w)]^{\frac{1}{2}}=\omega[l_0^ec_0]^{\frac{1}{2}}. \quad (2.30)$$

With (2.23)–(2.27), and after eliminating $q(w)$, (2.20) and (2.21) lead to

$$I_x(w)=\frac{\partial V(w)/\partial w+\beta_0p(w)V_L(w)}{z^i+j\omega l_0^e(w)}. \quad (2.31)$$

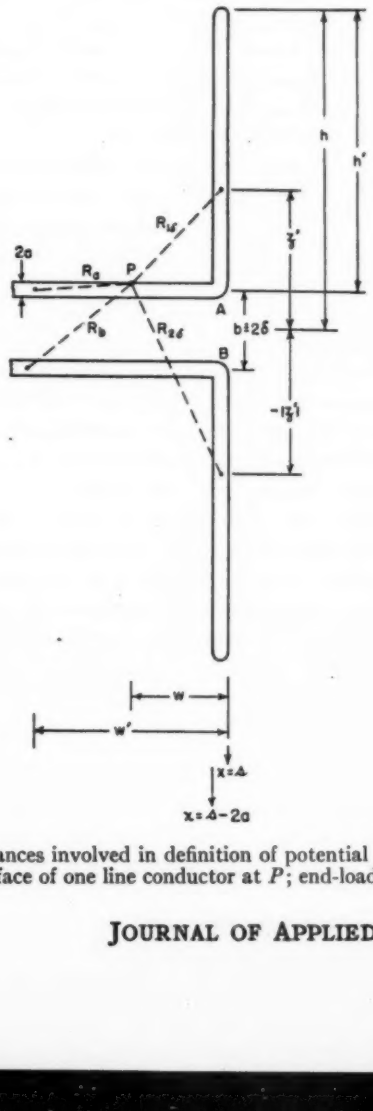

FIG. 7. Distances involved in definition of potential functions on the surface of one line conductor at P; end-loaded line.

The generalized transmission-line equations for the voltage $V(w)$ and the current $I_x(w)$ are (2.31) together with (2.15b) with w replacing x. Since z^i for good conductors is small, only an insignificant error is involved if the correction term with the factor $p(w)$ in (2.31) is neglected in evaluating $z^i(\partial I_x(w)/\partial w)$, and $l_0^e(w)$ is treated as constant in the differentiation. These approximations involve errors only very near the ends, and they are tolerated only in the small term in z^i. Thus,

$$z^i\frac{\partial I_x(w)}{\partial w}\doteq\frac{z^i}{z^i+j\omega l_0^e(w)}\frac{\partial^2 V(w)}{\partial w^2}. \tag{2.32}$$

Let the complex propagation constant be defined as follows:

$$\gamma^2=\frac{-\beta_0^2[z^i+j\omega l_0^e(w)]}{j\omega l_0^e(w)}=j\omega c_0(w)[z^i+j\omega l_0^e(w)]. \tag{2.33}$$

Since z^i is small,

$$z^i+j\omega l_0^e(w)\doteq[z^i+j\omega l_0^e][k_0(w)/k_0(\infty)]\equiv z(w), \tag{2.34}$$

so that

$$\gamma^2\doteq j\omega c_0(z^i+j\omega l_0^e), \tag{2.35}$$

which is independent of w.

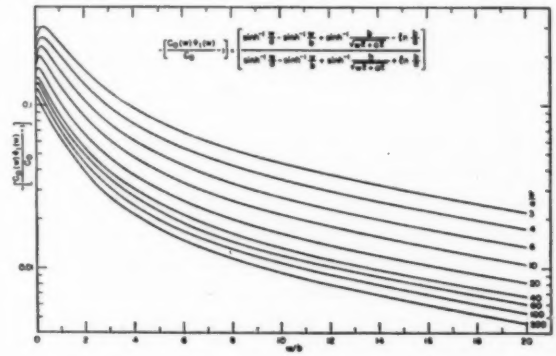

FIG. 8. Plot of function involved in determining the equivalent lumped capacitance of terminal zone with end-loaded line.

Using (2.32)–(2.35) in (2.15b) with $w=s-x$ replacing x, this becomes

$$\frac{\partial^2 V(w)}{\partial w^2}-\gamma^2\phi_1(w)V(w)=0, \tag{2.36}$$

where

$$\phi_1(w)\equiv\frac{V(w)-V_T(w)}{V(w)}=\frac{V_L(w)}{V(w)}=\frac{V_L(w)}{V_L(w)+V_T(w)} \tag{2.37}$$

is the ratio of the scalar potential difference across the line due to the charges on the line to the scalar potential differences across the line due to the charges on the line *and on the termination*. $\phi_1(w)$ reduces to unity except near the ends of the line. Moreover, near these ends, $V_T(w)$ is essentially in phase with $V_L(w)$ since the charges that contribute *significantly* to $V_T(w)$ and $V_L(w)$ cannot be separated more than a fraction of a wave-length. Accordingly, $\phi_1(w)$ is essentially real. It is regarded conveniently as a variable scale factor for the capacitance $c_0(w)$ that appears in the expression (2.33) for γ^2. Thus, let

$$c_T(w)\equiv c_0(w)\phi_1(w) \tag{2.38}$$

$$\gamma^2(w)\equiv\gamma^2\phi_1(w)=j\omega c_T(w)z(w), \tag{2.39}$$

so that (2.36) becomes

$$[\partial^2 V(w)/\partial w^2]-\gamma^2(w)V(w)=0. \tag{2.40}$$

With (2.34) and (2.37), (2.31) reduces to

$$I_x(w)=1/z(w)\{[\partial V(w)/\partial w]+\beta_0 p(w)\phi_1(w)V(w)\} \tag{2.41}$$

Equations (2.40) and (2.41) are the final equations from which the scalar potential difference and the current in the two-wire line must be determined.

At distances from the ends of the line specified by the conditions, $w^2\gg b^2$, $x^2\gg b^2$, it is readily verified that (2.40) and (2.41) reduce to the well-known formulas of conventional transmission-line theory. Also,

$$W_x(w)=I_x(w)l_0^e;\quad V_L(w)=V(w)=q(w)/c_0. \tag{2.42}$$

Evidently, the distributions of current and axial vector potential difference are the same as are the distributions of charge per unit length and scalar potential difference, *except near the ends of the line where these simple proportionalities are not true.*

The results thus far obtained imply $a^2\ll b^2$. They are readily generalized to permit unrestricted values of a/b by substituting $b^e=(b/2)[1+(1-(2a/b)^2)^{\frac{1}{2}}]$ for b.[7]

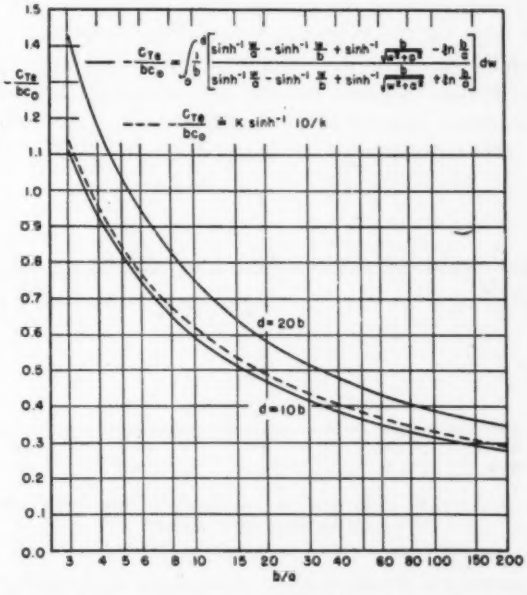

FIG. 9. Plot of equivalent lumped capacitance C_{Te} for end-loaded line for two lengths d of the terminal zone as a function of b/a. Broken line curve is C_{Te} computed from approximate formula.

[7] See reference 6, p. 440.

Conventional line theory assumes the consequences of $w^2 \gg b^2$, $x^2 \gg b^2$ *to be valid for all values of* w *and* x. That this leads to serious errors whenever $\beta_0 b$ is not extremely small is shown in the following sections.

3. APPROXIMATE SOLUTION OF THE GENERALIZED TRANSMISSION-LINE EQUATIONS

The generalized transmission-line equations that are to be solved for the scalar potential difference V and the current I_z are (2.40) and (2.41). Their solution cannot be carried out directly since $\gamma^2(w)$ is not a constant parameter independent of w in the terminal zones defined by

$$0 \leqq x \leqq d \sim 10b; \quad 0 \leqq w \leqq d \sim 10b, \tag{3.1}$$

but is a complicated function of x or w, different for each termination. However, $\gamma^2(w)$ reduces to the constant γ^2 at all points outside the terminal zones. For distances b between the conductors of the line that satisfy $\beta_0^2 b^2 \ll 1$, the length d of the terminal zone does not exceed small multiples of b. Accordingly, if the solution of (2.40) along the principal line outside the terminal zone is expressed as follows,

$$V(w) = A \cosh\gamma w + B \sinh\gamma w, \tag{3.2}$$

A, B, and γ are constants outside the terminal zones. In the terminal zones a solution in the form (3.2) is not helpful, since A, B, and γ would have to be complicated functions of the variable w (or x). This suggests the following method for determining an approximate solution at all points outside the terminal zones. The physical basis of the method is straightforward. It involves reducing (2.40) and (2.41) to conventional form at *all* points along the line by replacing $\gamma^2(w)$, $z(w)$, and and $p(w)$ by the constant values these functions have outside the terminal zone, *viz.* γ^2, z, and zero. This substitution is exact outside the terminal zone; it is increasingly in error as the terminal zone is entered and the terminated end of the line is approached. This error

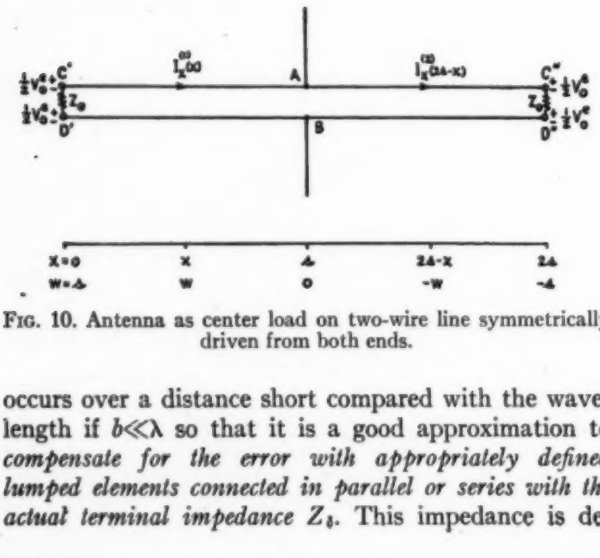

FIG. 10. Antenna as center load on two-wire line symmetrically driven from both ends.

occurs over a distance short compared with the wavelength if $b \ll \lambda$ so that it is a good approximation to *compensate for the error with appropriately defined lumped elements connected in parallel or series with the actual terminal impedance* Z_s. This impedance is defined as the ratio of scalar potential difference to current; (the discussion is confined to the load at $w=0$ or $x=s$ with the understanding that a parallel procedure applies at $x=0$). In other words, the analytical method is equivalent to replacing the actual terminal zone with its terminating impedance Z_s by an equal length of *conventional line with constant parameters* and a fictitious, apparent load Z_{sa} that is a combination of lumped elements in parallel or series with Z_s. (Note that Z_{sa} is the impedance actually *measured* on the line at $\lambda_0/2$ from the load, if the line is lossless.) These lumped elements, C_T and $Z_T \doteq j\omega L_T$ are defined as follows:

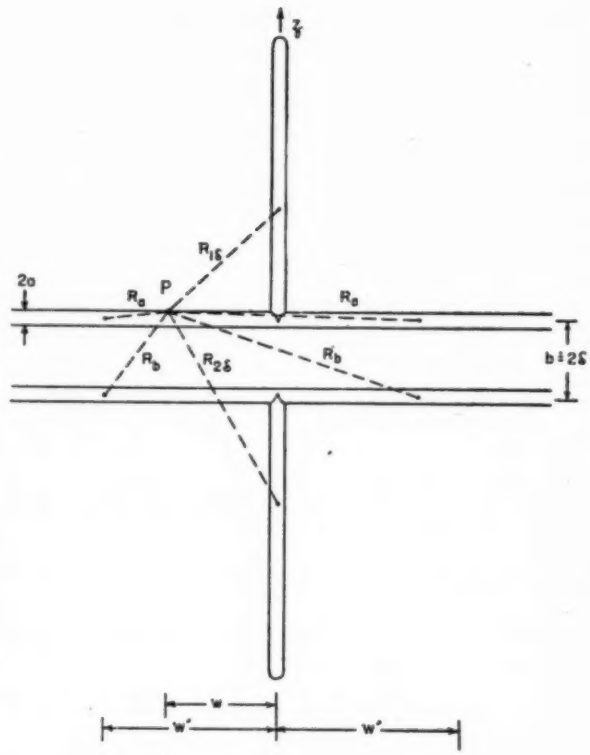

FIG. 11. Distances involved in definition of potential functions on the surface of one line conductor at P; center-loaded line.

$$C_T \equiv \int_0^d [c_T(w) - c_0]dw = \int_0^d [c_0(w)\phi_1(w) - c_0]dw. \tag{3.3}$$

That is, a constant-distributed capacitance per unit length, c_0, and a lumped capacitance, C_T, at $w=0$ are made approximately equivalent to a distributed capacitance per unit length $c_T(w)$. Since C_T takes account of the coupling between the termination and the line, it can be evaluated only if the structure of the termination is given.

$$Z_T \equiv \int_0^d [z(w) - z]dw. \tag{3.4a}$$

Since a small error in z^i is insignificant if confined to the

terminal zone, (3.4a) is practically equivalent to

$$L_T \equiv \int_0^d [l_0^e(w) - l_0^e] dw. \qquad (3.4b)$$

Thus, a lumped inductance L_T must be assumed connected in series with Z_s at $w=0$ if the constant parameter z is substituted for the actual, variable parameter $z(w)$.

The lumped series inductance defined in (3.4b) is readily evaluated. Near the end $w=0$ or $x=s$, x is very great compared with b; furthermore, $d^2 \gg b^2$. With (2.23) the result is

$$L_T \doteq -(b-a)/2\pi v_0. \qquad (3.5)$$

Since the lumped network of C_T and L_T is designed to make the terminated transmission line like an infinite line, it follows that $p(w)$ must assume the appropriate value, *viz.* zero. Accordingly, for determining currents and voltages at points outside the terminal zone, the actual line with variable parameters may be replaced by a fictitious line with constant parameters and a modified termination. The two lines are the same outside the terminal zone, and they maintain the same ratio of scalar potential difference to current across the load. The equations for the *fictitious* line are the conventional ones, *viz.*,

$$[\partial^2 V(w)/\partial w^2] - \gamma^2 V(w) = 0 \qquad (3.6)$$

$$I_z(w) = (1/z)[\partial V(w)/\partial w]. \qquad (3.7)$$

It may be concluded that for determining the scalar potential difference and current for a line *outside* the terminal zone, or for determining the theoretical load admittance Y_s, it is possible to treat the terminal zone as though conventional line theory with constant parameters applied, provided Y_s is treated as though connected in parallel with a lumped capacitance C_T and in series with a lumped inductant L_T as shown in Fig. 4a or 4b. For use in conjunction with an "image line" the circuit of Fig. 5 is convenient. It is equivalent to Fig. 4b but with elements so arranged that they are symmetrical with respect to a plane midway between the wires of the line.

The lumped series inductance L_T has been shown to be negative. It compensates for the use of a constant inductance per unit length l_0^e in the terminal zone in place of the variable $l_0^e(w)$. The lumped parallel capacitance C_T may be positive or negative, depending upon the structure of the termination. For an antenna it is negative. It corrects for the use of a constant capacitance per unit length c_0 in the terminal zone instead of the variable $c_T(w)$. The function of $c_T(w)$ includes the variation in capacitance per unit length near the end of the line as contained in $c_0(w)$ and, in addition, the effect of coupling between the line and the termination. (Note that there is no contribution to $l_0^e(w)$ due to coupling only because it has been assumed that the termination is so designed that currents in it are either perpendicular to the line or include equal and opposite elements with canceling effects.)

4. ANTENNA TERMINATING TWO-WIRE LINE

The rigorous one-dimensional analysis of the circuit consisting of a completely balanced two-wire line terminated in a symmetrical center-driven antenna (Fig. 6) requires the solution of simultaneous integro-differential equations for the distributions of current both in the antenna and in the two-wire line. Since the antenna and the line are coupled over distances along the atenna and along the line comparable with small multiples of the finite separation b of the conductors of the line, the definition of an input impedance Z_{BA} (Fig. 6), that is characteristic of the *antenna alone* and independent of the feeding line, is not possible. An impedance in the sense of conventional transmission-line theory can be defined only for a sufficiently long section of line terminated in the antenna. Thus, $Z_{B'A'}$ can be defined if the distance $A'A$ in Fig. 6 is large com-

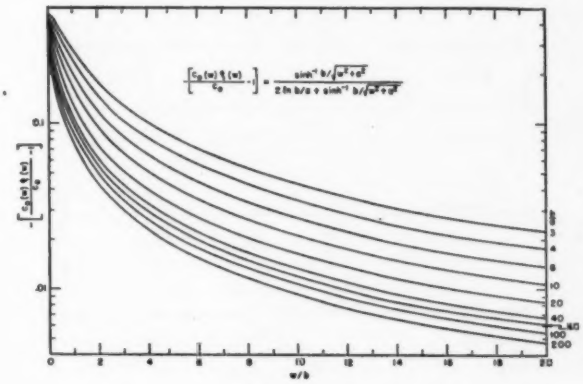

FIG. 12. Like Fig. 8 but for center-loaded line.

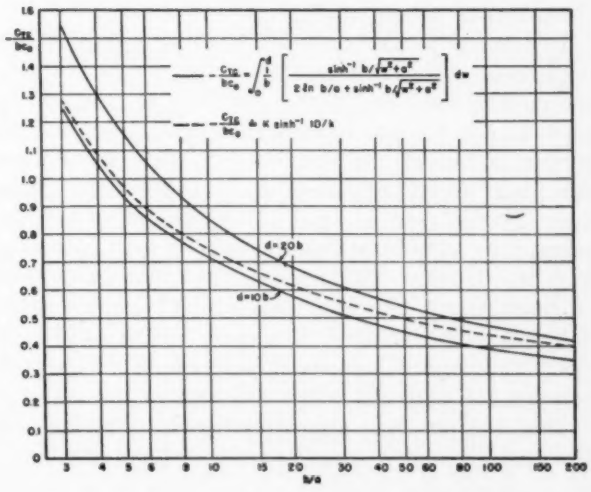

FIG. 13. Like Fig. 9 but for center-loaded line.

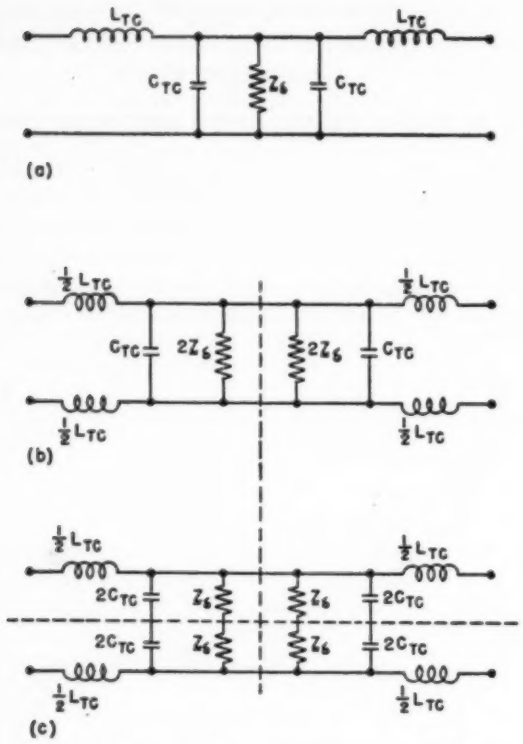

FIG. 14. Equivalent terminal-zone networks for center-loaded line.

pared with the spacing b. Note, however, that the impedance $Z_{B'A'}$ of the section of line to the right of $B'A'$ is not independent of the presence of the line to the left of $B'A'$. The assumption is implicit in the definition of every impedance on a transmission line that the uniform line continues in *both directions* from the points of definition $B'A'$.

In order to obtain an *approximate* expression for the impedance of an antenna terminating a two-wire line, the method described in the preceding section may be used. In effect, this considers the characteristics of the section of line to the right of $B'A'$ (Fig. 6) in three parts that depend primarily upon (1) the transmission line, (2) the antenna, and (3) the coupling between them. Since significant coupling is confined to distances from the junction of antenna and line that are of order of magnitude b, the condition $\beta_0^2 b^2 \ll 1$ assures essentially near-zone coupling. However, conditions of symmetry and perpendicularity eliminate *inductive* coupling between the currents in the line and in the antenna, so that the principal approximation is to replace the *distributed* capacitive coupling between line and antenna by a *concentrated* coupling in the form of a lumped capacitance in parallel with the antenna at its junction with the line. This is included in C_T. In this way, the transmission-line problem (1) and the antenna problem (2) are made effectively independent of each other except for the common potential difference across the terminals at the junction points and the requirement of continuity for the current at these terminals.

The determination of the lumped capacitance C_T defined by (3.3) involves the prior evaluation of the function

$$[c_0(w)\phi(w)-c_0]\equiv[q_L(w)/V(w)]-c_0 \qquad (4.1)$$

$$V(w)=V_L(w)+V_T(w), \qquad (4.2)$$

where $V_L(w)$ is the contribution to the scalar potential difference $V(w)$ across the line due to the distribution of charge $q_L(w)$ on the line alone, and where $V_T(w)$ is the contribution due to the distribution of charges on the termination—in this case the antenna. The function $V_L(w)$ is defined by (2.13) with w substituted for x; (Fig. 7). The function $V_T(w)$ is defined, in general, as follows:

$$V_T(w)=\frac{1}{2\pi\epsilon_0}\int_{b/2}^{h} q(z')\left[\frac{e^{-j\beta_0 R_{1\delta}}}{R_{1\delta}}-\frac{e^{-j\beta_0 R_{2\delta}}}{R_{2\delta}}\right]dz', \qquad (4.3)$$

where

$$R_{1\delta}\doteq\left[\left(z'-\frac{b}{2}\right)^2+w^2+a^2\right]^{\frac{1}{2}};$$

$$R_{2\delta}\doteq\left[\left(z'+\frac{b}{2}\right)^2+w^2+a^2\right]^{\frac{1}{2}}, \qquad (4.4)$$

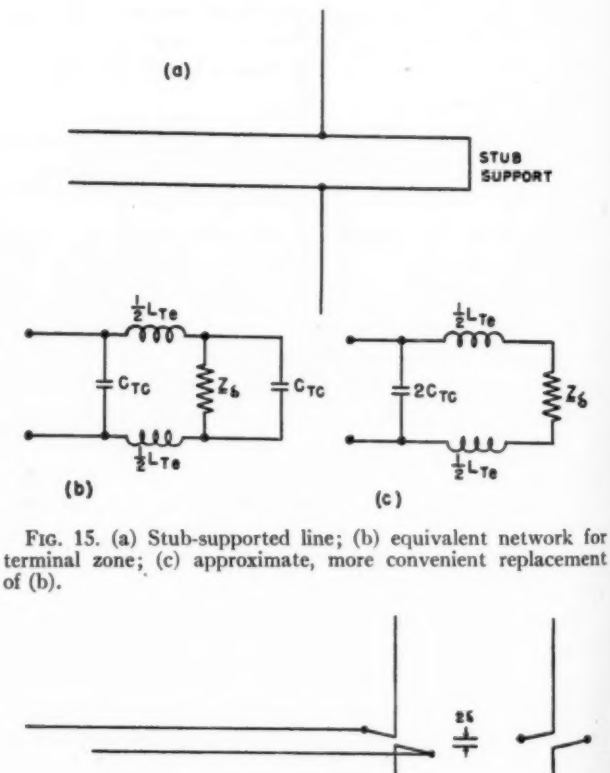

FIG. 15. (a) Stub-supported line; (b) equivalent network for terminal zone; (c) approximate, more convenient replacement of (b).

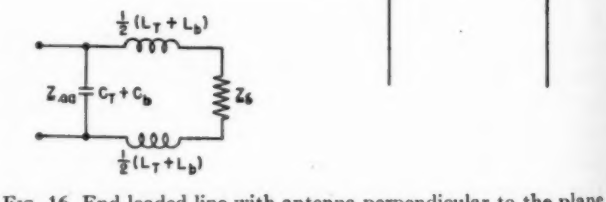

FIG. 16. End-loaded line with antenna perpendicular to the plane of the line; equivalent terminal-zone network.

and where $q(z')$ is the charge per unit length on the upper half of the antenna; $q(z')$ is an odd function of z'.

The exact evaluation of $V_L(w)$ and $V_T(w)$ is intricate. Fortunately, subject to the condition $\beta_0^2 b^2 \ll 1$, significant contributions to the integrals in (4.3) and (4.5) come only from the integrands when evaluated at distances from the junction that are not large compared with b. Accordingly, the exponentials may be replaced by their leading terms of unity, and the upper limit of integration may be made infinite.

$$V_L(w) \doteq \frac{\bar{q}_L}{2\pi\epsilon_0}\int_0^\infty \left[\frac{1}{R_a}-\frac{1}{R_b}\right]dw', \qquad (4.5)$$

$$V_T(w) \doteq \frac{\bar{q}_T}{2\pi\epsilon_0}\int_{b/2}^\infty \left[\frac{1}{R_{1b}}-\frac{1}{R_{2b}}\right]dw'. \qquad (4.6)$$

The quantity $\bar{q}_L$ is the average charge per unit length on the upper conductor of the line in the terminal zone. Similarly, $\bar{q}_T$ is the average charge per unit length on the upper half of the antenna in a short region near the junction point. The approximations made in obtaining (4.5) and (4.6) are essentially the same as those implied in the derivation of the conventional line equations, but since $V_T(w)$ and $V_L(w)$ are involved here only in correction terms, these approximations are equivalent to higher order errors. The integrals may be evaluated directly.

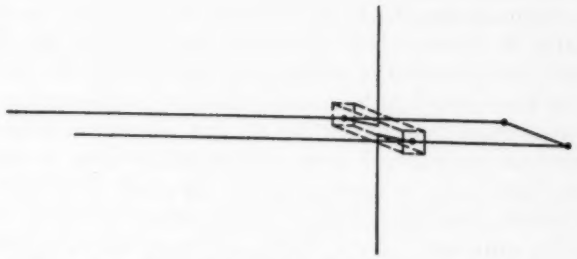

FIG. 17. Like Fig. 16 but with dielectric and stub supports adjusted to give maximum voltage across antenna terminals when the antenna is removed.

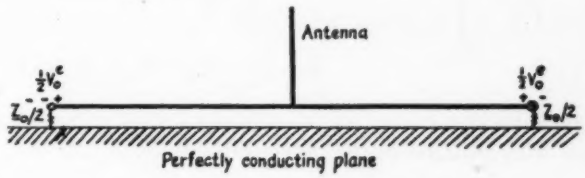

FIG. 18. Image-plane equivalent of Fig. 10.

$$V_L(w) \doteq \frac{\bar{q}_L}{c_0(w)}; \quad V_T(w) = \frac{\bar{q}_T}{2\pi\epsilon_0}\sinh^{-1}\frac{b}{(w^2+a^2)^{\frac{1}{2}}}. \qquad (4.7)$$

In order to evaluate $[c_0(w)\phi_1(w)-c_0]$ it is necessary to substitute (4.7) in (4.1). For convenience, let the charge-ratio factor k_q be defined by $k_q \equiv \bar{q}_T/\bar{q}_L$. Then,

$$[c_0(w)\phi_1(w)-c_0]/c_0 = -\left\{\frac{\sinh^{-1}(w/a)-\sinh^{-1}(w/b)+k_q\sinh^{-1}[b/(w^2+a^2)^{\frac{1}{2}}]+\ln(b/a)}{\sinh^{-1}(w/a)-\sinh^{-1}(w/b)+k_q\sinh^{-1}[b/(w^2+a^2)^{\frac{1}{2}}]-\ln(b/a)}\right\}. \qquad (4.8)$$

It is readily argued that $k_q \doteq 1$ is a satisfactory approximation.

The function $[c_0(w)\phi_1(w)-c_0]/c_0$, as defined in (4.8), is shown plotted in Fig. 8 with b/a as parameter and w/b as independent variable in the range from $w/b=0$ to $w/b=20$ with $k_q=1$. The area under each of these curves from $w=0$ to $w=d$ multiplied by $-c_0 b = -b\pi\epsilon_0/\ln b/a$ is the desired lumped capacitance C_{Te} (subscript e for end-loaded line) for each value of b/a and an appropriate choice of d. These areas, obtained by numerical methods, are shown in Fig. 9 as a function of b/a and for $d=10b$ and $d=20b$. Since the values of $-C_{Te}/bc_0$ for these two choices of the length d of the terminal zone differ appreciably, it is clear that significant capacitive coupling between the antenna and the line exists for distances from the antenna exceeding 10 times the line spacing b. This means that the representation of this distributed effect by an equivalent lumped capacitance at $w=0$ is necessarily only a fair approximation unless d can be taken quite large compared with b and yet be a small fraction of a wave-length. In order to make it possible to treat end-effects on lines at frequencies for which $b/\lambda_0 \leqq 0.02$, it is necessary to restrict d to at most $10b$ or $0.2\lambda_0$. Even for this length the assumption of equal average charge concentrations per unit length on antenna and line ($k_q=1$) is justified only near antiresonance.

For the rapid evaluation of C_{Te}, a closed formula is desirable. The shapes of the curves obtained in Fig. 8 suggest

$$C_{Te} = -c_0\int_0^d \frac{Kb}{(w^2+k^2b^2)^{\frac{1}{2}}}dw = -c_0 bK\sinh^{-1}\frac{d}{kb}. \qquad (4.9)$$

K and k are determined by fitting $-Kb/(w^2+k^2b^2)^{\frac{1}{2}}$ to $[c_0(w)\phi_1(w)-c_0]/c_0$ in the range of w from zero to $d=10b$. This is done by requiring (4.9) to be satisfied exactly at $w=a$ and $w=3b$.

Curves showing the approximate function $-C_{Te}/bc_0$ as evaluated from (4.8) are shown in Fig. 9 together with the same function determined from (4.9) by numerical integration. The agreement is seen to be fair, with the approximate curve falling between the curves for terminal zones of length $d=10b$ and $d=20b$. Since the proposed representation of a distributed effect by a lumped capacitance is in any case far from exact, the values of C_{Te} taken from the simple integrated formula (4.9) are quite satisfactory. Note that the order of magnitude of C_{Te} is that of a section of uniform line of length equal to the line spacing b.

Summarizing the analysis of the two-wire line terminated in a center-driven antenna, the following may be said: the apparent impedance Z_{sa} terminating the two-wire line—which is the actual impedance looking toward the antenna from a point on the line (assumed lossless) one-half wave-length from the antenna—may be determined using the circuit of Fig. 4a or 4b if the ratio of scalar potential difference to current at the terminals of the antenna, *viz.*, $Z_\delta = V_\delta/I_\delta$, is known. In the figures

$$L_T = L_{Te} = -(b-a)/2\pi v_0 \tag{4.12}$$

$$C_T = C_{Te} = \int_0^d [c_0(w)\phi_1(w) - c_0]dw \doteq -Kc_0 b \sinh^{-1}(d/kb). \tag{4.13}$$

The subscript e identifies the values for an end-loaded line with antenna in the plane of the line.

5. ANTENNA AS MIDPOINT LOAD FOR SYMMETRICALLY DRIVEN LINE

The circuit of Fig. 6, in which a center-driven antenna terminates a balanced two-wire line, has several practical shortcomings if interest lies in the accurate measurement of the impedance of the antenna. One of the problems is to support the antenna and line at or near their junction. A common method uses a piece of dielectric material. However, even the theoretical or experimental determination of the *actual* added capacitance due to a very thin dielectric support and not merely the *apparent* added capacitance is complicated. In usual practice only the *apparent combined* impedance terminating the line is of interest, and this is readily measured directly in each case. On the other hand, a complete, even though perhaps quantitatively only approximate understanding of the factors that contribute to the apparent impedance of a termination requires a separation of the effect of a dielectric support from those effects characteristic of the configuration of conductors.

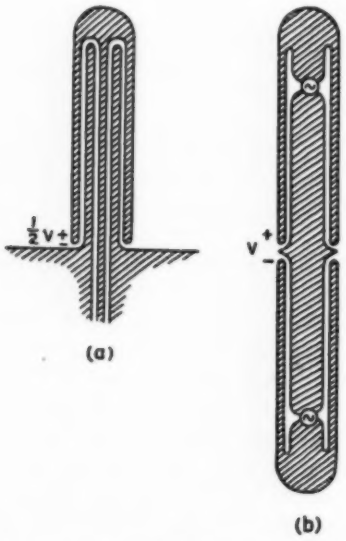

FIG. 19. Possible method of driving antenna to approximate slice generator with coaxial line in (a) and image equivalent in (b).

A very flexible structure which provides both a means of support for the line at its junction with the antenna and complete symmetry is the circuit shown in Fig. 10. The antenna is attached to the center of a symmetrical line that is driven from *each end by identical generators*. The currents in the two driving lines are equal in magnitude and opposite in direction at corresponding points measured from the antenna. The charge per unit length at these points are the same in magnitude and sign. The currents $I_z(w=0)$ at the junction point $w=0$ combine into the antenna current $I_z(\delta)$; the charge per unit length on the antenna near the junction point is equal to the charges per unit length on *each* of the two line conductors very near the junction.

If the impedance Z_δ of the antenna is defined formally as the ratio of the scalar potential difference V_δ at the junction point to the current $I_z(\delta)$,

$$Z_\delta \equiv \frac{V_\delta}{I_z(\delta)} = \frac{\phi(\delta)-\phi(-\delta)}{I_z(\delta)}, \tag{5.1}$$

it follows that,

$$Z_\delta = \frac{V_\delta}{2I_z^{(1)}(w=0)}, \tag{5.2}$$

where $I_z^{(1)}$ is the current in conductor 1 of the line.

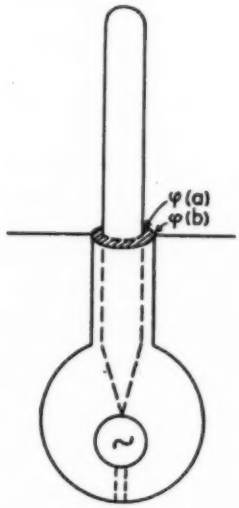

FIG. 20. Conventional method of driving antenna above image plane from coaxial line.

Hence, if complete symmetry is maintained, each line may be treated as though terminated in an impedance

$$2Z_\delta = \frac{V_\delta}{I_z^{(1)}(w=0)} = \frac{V_\delta}{-I_z^{(2)}(w=0)}. \tag{5.3}$$

Therefore, the entire analysis of Sections 2–4 applies, except that the lumped elements L_T and C_T must be re-evaluated since the two parts of the line are coupled not only to the antenna but also to each other.

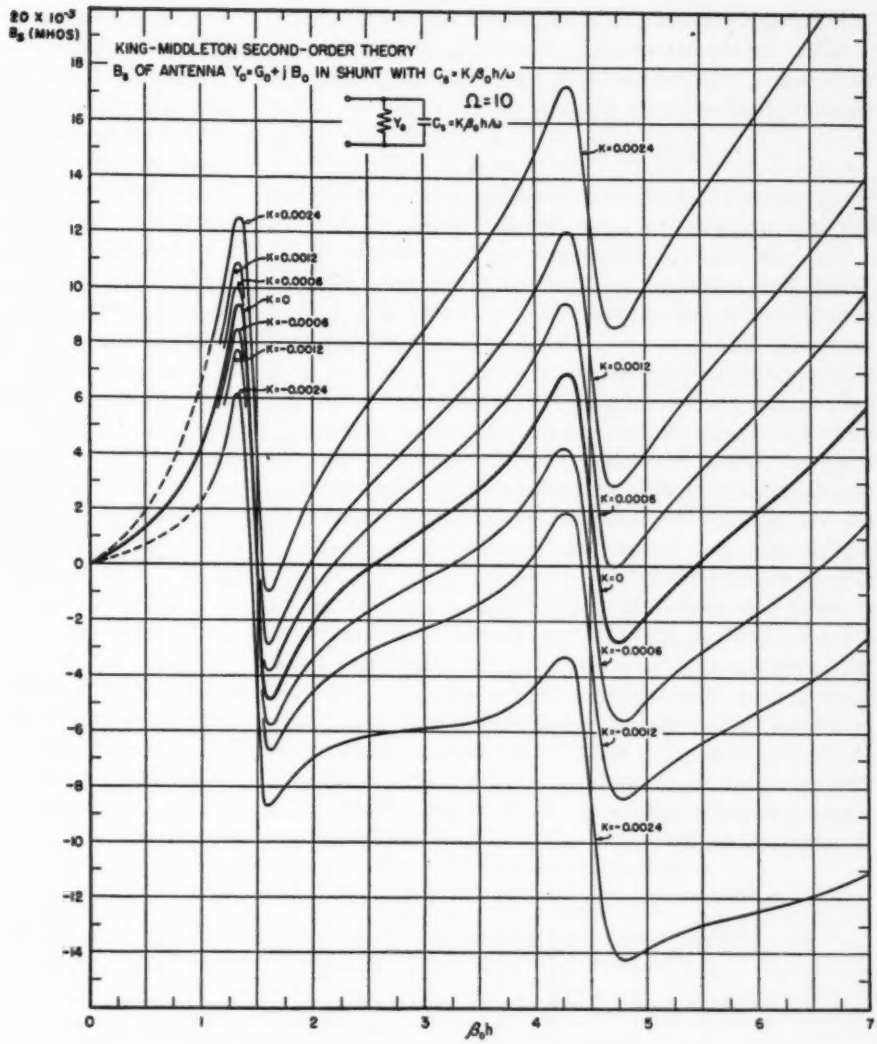

FIG. 21. Theoretical admittance of antenna in parallel with lumped positive and negative capacitances; for antenna $\Omega=2\ln(2h/a)=10$.

It is readily verified that

$$L_{TC}=-(b-a)/\pi v_0. \tag{5.4}$$

Note that L_{TC} in (5.4) is the lumped inductance to be connected in series with *each* half of the symmetrical line with uniform constants. The subscript C identifies the center-loaded line.

It remains to evaluate C_{TC}. This is carried out as for the end-loaded line but with the following modified expressions for $V_L(w)$ and $V_T(w)$ which must now include the effect of the additional feeding line (Fig. 11).

$$V_L(w)\doteq\frac{\bar{q}_L}{2\pi\epsilon_0}\int_{-\infty}^{\infty}\left[\frac{1}{R_a}-\frac{1}{R_b}\right]dw'=\frac{\bar{q}_L}{\pi\epsilon_0}\ln\frac{b}{a} \tag{5.7}$$

$$V_T(w)\doteq\frac{\bar{q}_T}{2\pi\epsilon_0}\int_{b/2}^{\infty}\left[\frac{1}{R_{1b}}-\frac{1}{R_{2b}}\right]dz'$$

$$=\frac{\bar{q}_T}{2\pi\epsilon_0}\sinh^{-1}\frac{b}{(w^2+a^2)^{\frac{1}{2}}}. \tag{5.8}$$

As before, $k_q=\bar{q}_T/\bar{q}_L$, where $\bar{q}_T$ is the average charge per unit length on the antenna near the junction with the line, and $\bar{q}_L$ is the average charge per unit length on one conductor on each of the two lines.

Substitution of (5.7) and (5.8) in (4.1) gives

$$[c_0(w)\phi_1(w)-c_0]/c_0$$

$$=-\left\{\frac{k_q\sinh^{-1}[b/(w^2+a^2)^{\frac{1}{2}}]}{2\ln(b/a)+k_q\sinh^{-1}[1/(w^2+a^2)^{\frac{1}{2}}]}\right\}. \tag{5.9}$$

Curves of $[c_0(w)\phi(w)-c_0]/c_0$ for $k_q=1$ are in Fig. 12.

Comparison with Fig. 8 shows that for the center-loaded line, $[c_0(w)\phi(w)-c_0]/c_0$ is approximately equal to its value for the end-loaded line except at very small values of w/b. The lumped capacitance C_{TC} is given by (3.3).

Curves showing C_{TC} as a function of b/a are in Fig. 13 as evaluated by numerical methods with $d=10b$ and $d=20b$. Comparison with Fig. 13 for C_{Te} shows that they are roughly equal.

Since the general shapes of the curves of $[c_0(w)\phi(w) - c_0]/c_0$ for the center-loaded line is the same as for the end-loaded line except near $w/b=0$, they may be evaluated as before by setting

$$[c_0(w)\phi_1(w)-c_0]/c_0=-K/[(w/b)^2+k^2]^{\frac{1}{2}}. \quad (5.10)$$

K and k are obtained by evaluating (5.10) at $w=0$ and $w=3b$. Curves of $-C_{TC}/bc_0$ are in Fig. 13.

To conclude the discussion of the symmetrically driven line, attention is called to the circuit of Fig. 14a which must replace the antenna as center-load if conventional transmission-line theory is to be a satisfactory approximation. In actual use the circuit of Fig. 14b, which is equivalent to Fig. 14a, is convenient. Since no current crosses the central axis of symmetry, the two connections between the two loads $2Z_\delta$ may be removed and each side treated separately. Alternatively, the circuit may be arranged as in Fig. 14c which is useful when an "image line" is used, as discussed in Section 6 and Part III.

Since L_{TC} is exactly twice L_{Te} but is connected in series with $2Z_\delta$ in Fig. 14b, the inductive corrections are the same for the center-loaded and end-loaded lines. Since C_{TC} is approximately the same as C_{Te}, C_{TC} in parallel with $2Z_\delta$ for the center-loaded line is *effectively double* C_{Te} in parallel with Z_δ for the end-loaded line. The apparent terminal impedance Z_{sa} of a *particular* antenna must, therefore, be different when determined for the antenna as end-load from its value for the *same* antenna as center-load unless C_T is negligible.

Instead of a dielectric support, a so-called "stub" support consisting of a high impedance, antiresonant section of transmission line may be used (Fig. 15). In order to achieve a sufficiently high impedance, losses in the stub must be very small and, hence, the adjustment to antiresonance very critical. A practical procedure is to determine accurately with a sensitive probe the location of the voltage maximum with the antenna absent, and then to attach the antenna exactly at this point. If the stub is so constructed that the impedance of the stub is very great compared with that of the antenna, the current in the stub near the junction with antenna and line is very small, so that the inductance per unit length of the transmission line differs only negligibly from that for the unsupported line and antenna. Hence, $L_T=L_{Te}$. However, the concentrations of charge on the sections of the stub near the junction point are by no means negligible compared with those on adjacent sections of the antenna and the line proper. When there is a maximum voltage at the terminals of the antenna, the distribution of voltage and charge along the transmission line including the stub is essentially the same as the distribution for the symmetrical, center-loaded line. Accordingly, $C_T \doteq C_{TC}$. However, in this instance the impedance terminating the line is not $2Z_\delta$ but simply Z_δ so that the equivalent terminal-

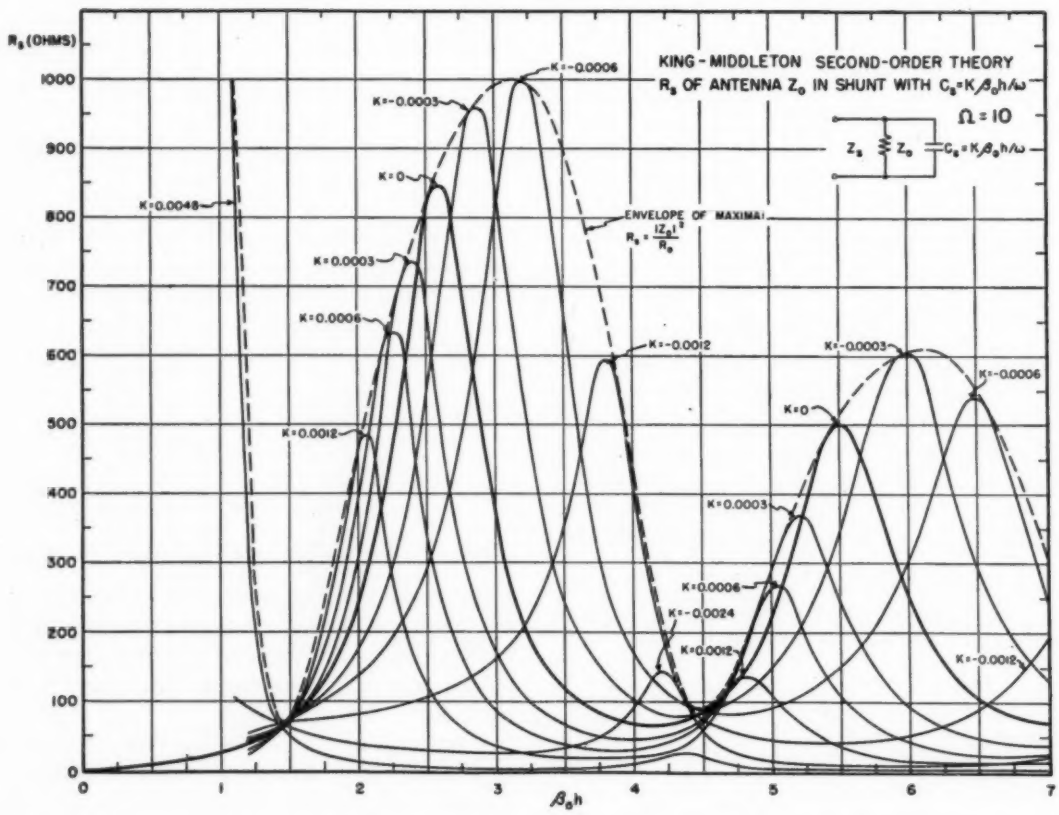

FIG. 22. Theoretical resistance of antenna in parallel with lumped positive and negative capacitances; $\Omega=10$.

zone network is in Fig. 15b rather than in Fig. 14b. Note also that L_{Te} replaces L_{TC}. No inductances are required on the right, since the current into the high impedance stub is always small. Since L_{Te} is small, the two capacitances may be combined as in Fig. 15c without significant error. The resulting circuit is the same as for the center-loaded antenna in Fig. 14b. Note that the capacitance C_{TC} on the right in Fig. 15b is due entirely to coupling between the antenna and the stub, so that it can *not* be compensated by adjusting the stub with the antenna removed. For this reason it must be included in the circuit even if the stub is adjusted experimentally to put a voltage maximum at the load terminals before the antenna is connected.

6. ANTENNA CENTER-DRIVEN FROM A TWO-WIRE LINE WITH MINIMUM COUPLING; IMAGE METHOD OF DRIVING AN ANTENNA USING OPEN-WIRE LINE; ANTENNA PERPENDICULAR TO IMAGE PLANE

In order to eliminate *all* coupling between antenna and transmission line it is necessary to orient the antenna so that the vector and scalar potentials *due to currents and charges on the transmission line* vanish at *all* points along the antenna. In the end-loaded and center-loaded lines the tangential vector potential due to currents in the line is zero on the surface of the antenna since antenna and line are mutually perpendicular; however, the scalar potential on the surface of the antenna due to charges on the line does not vanish. In order to make this zero on the antenna, opposite points on the two conductors of the line must be made equidistant from each point on the axis of the antenna. If this is done, the contribution to the scalar potential at any cross section of the antenna by the charges in one conductor of the line is canceled by the scalar potential due to an identical distribution of charge of *opposite sign* on the second conductor of the line. One method of accomplishing this cancelation is shown in Fig. 16a for an antenna driven as an end load. (In this circuit there is *no inductive coupling* between the antenna and the line or the antenna and the short bridges connecting the antenna to the line so that the inductive end-effect is due exclusively to the absence of an infinite line just as in the more conventional circuit in Fig. 1. Therefore, the same value of L_T may be used.)

In the conventional end-loaded line the correcting capacitance C_T combines the effect of non-uniformity in the capacitance per unit length of line with coupling between line and load. In the arrangement of Fig. 16 this latter effect vanishes so that C_T is simplified to the extent that direct coupling between the two parallel conductors of the line and the antenna is eliminated. If the two short conductors connecting the ends of the line to the terminals of the antenna were exactly perpendicular to the antenna, the scalar potentials on the antenna due to the equal charges of opposite sign on

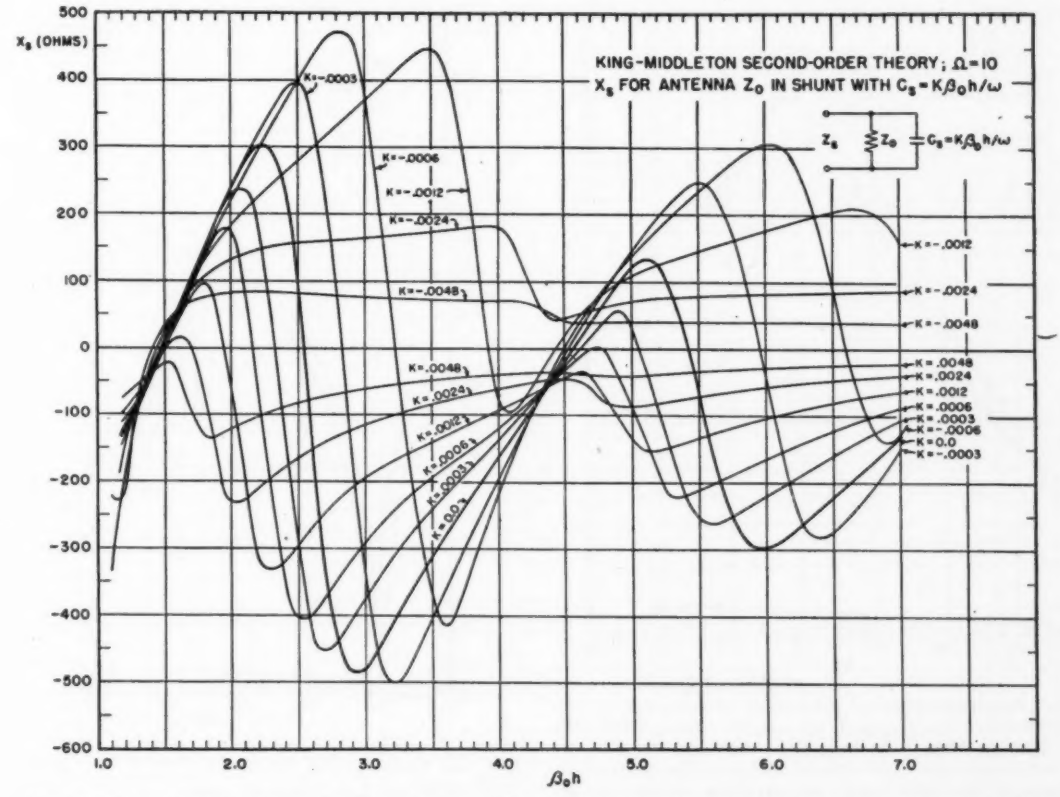

FIG. 23. Theoretical reactance of antenna in parallel with lumped positive and negative capacitances; $\Omega=10$.

them would cancel exactly. Evidently this is possible only in the idealized case of zero gap. For a finite gap the potentials due to the charges on the short connecting sections do not quite cancel, so that a small capacitive coupling between antenna and the connecting conductors exists. Since each of the conductors is essentially of length $b/2$ the magnitude of the coupling is very small and approximately equivalent to a small lumped capacitance connected across the terminals of the antenna.

In practice the arrangement of Fig. 16 is not convenient without a dielectric or stub support, of which account must be taken. Fortunately, and unlike the corresponding situation in Fig. 15, the presence of a stub in the form of a continuation of the line as shown in Fig. 17 involves *no coupling* to the antenna, although L_T and C_T are affected due to modification of end-effect on the line. However, since the antenna is not directly involved, it is possible to use a dielectric support in conjunction with a stub so adjusted that in the absence of the antenna the impedance of the dielectric in parallel with the stub is very great compared with the maximum impedance of the antenna. Experimentally, this is readily accomplished by adjusting the length of the stub in the absence of the antenna until a voltage maximum occurs exactly at the dielectric support as determined from the main line. In this way end-effect and the presence of the dielectric and the stub are all combined in a manner that virtually eliminates them. If the antenna is attached after this adjustment has been made, the impedance measured for the termination is essentially the impedance Z_δ of the antenna. That is, $Z_{sc} \doteq Z_\delta$, if the series inductance of the half-bridges is negligible, as is true when these are of sufficiently large cross section.

The experimental study of antennas center-driven from a balanced two-wire line may be facilitated in some instances if use is made of the theorem of images[8] to provide equivalent structures which provide a shield for the observer. For the conventional end-load line (Fig. 6) or the center-loaded line (Fig. 10) (but not for the circuits of Figs. 16 and 17), the plane $z=0$, perpendicular to and bisecting the rectangle formed by the line, is a plane of symmetry for the entire circuit. On this plane the tangential component of the electric field is zero everywhere, so that nothing is changed electromagnetically if a perfectly conducting sheet is placed to coincide with the plane $z=0$. Such a sheet completely isolates the halves of the circuit and the fields associated with their charges and currents, so that one-half may be removed without disturbing the other. Each then consists of one conductor of the original two-wire line parallel to a perfectly conducting sheet at a distance $b/2$ and one-half of the original

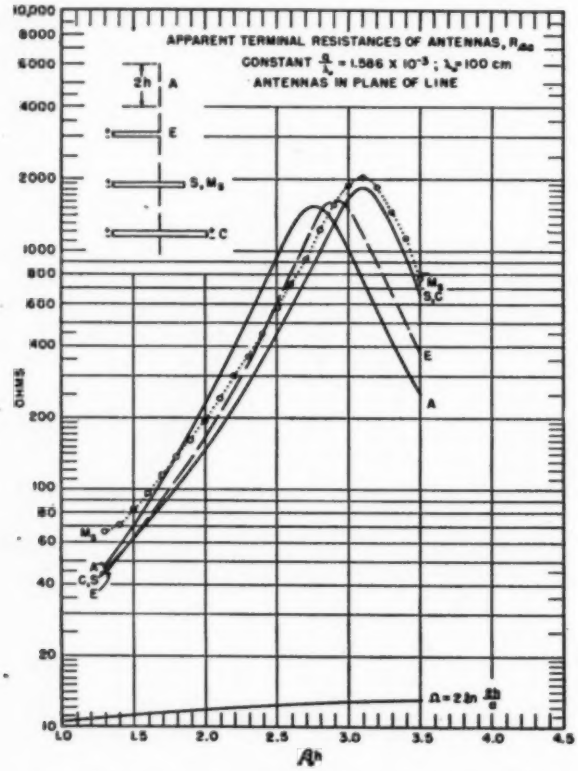
APPARENT TERMINAL RESISTANCES OF ANTENNAS, R_{sc}
CONSTANT $\frac{a}{\lambda}$ = 1.586 X 10⁻³ ; λ_p = 100 cm
ANTENNAS IN PLANE OF LINE
OHMS
$\Omega = 2\ln\frac{2b}{a}$
$\frac{2h}{\lambda}$

FIG. 24(a). Apparent terminal resistances of antennas in the plane of the two-wire line. Curve A, second-order King-Middleton theory for antenna with slice generator; curve E, theory corrected for end-load; curve S, C theory corrected for center-load or stub-supported end-load; curve M_s, experimental data of K. Tomiyasu for stub-supported end-load.

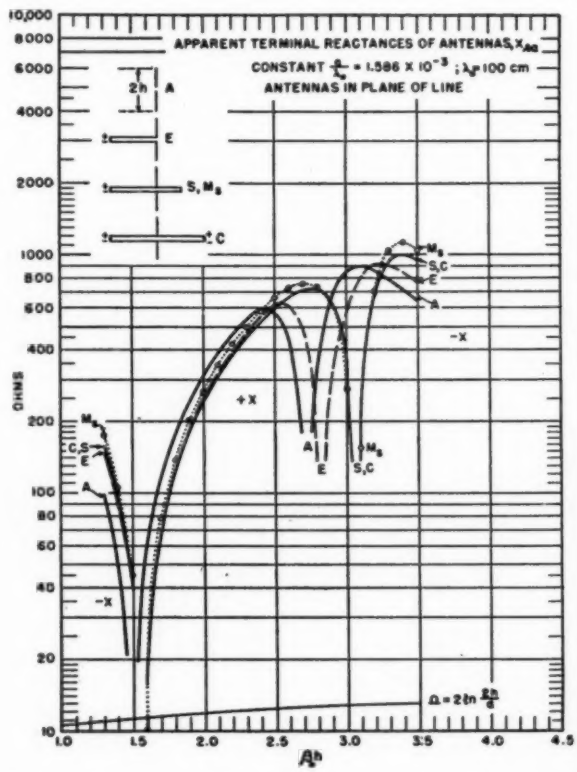
APPARENT TERMINAL REACTANCES OF ANTENNAS, X_{sc}
CONSTANT $\frac{a}{\lambda}$ = 1.586 X 10⁻³ ; λ_p = 100 cm
ANTENNAS IN PLANE OF LINE
OHMS
$\Omega = 2\ln\frac{2b}{a}$
$\frac{2h}{\lambda}$

FIG. 24b. Like Fig. 24a but for reactances instead of resistances.

[8] See reference 6, Section IV, p. 20.

antenna perpendicular to the sheet as shown in Fig. 18 for the center-loaded line.

Instead of using half of a two-wire line over a conducting plane, it is often convenient to use a coaxial line in the arrangement shown in Fig. 19. In so far as the electromagnetic field and distributions of current and charge in the half-space $z \geqq 0$ are concerned, the theorem of images states that the circuit of Fig. 19a is equivalent to the physically awkward, symmetrical, center-driven circuit of Fig. 19b. In order that the scalar potential difference across the double gap in the

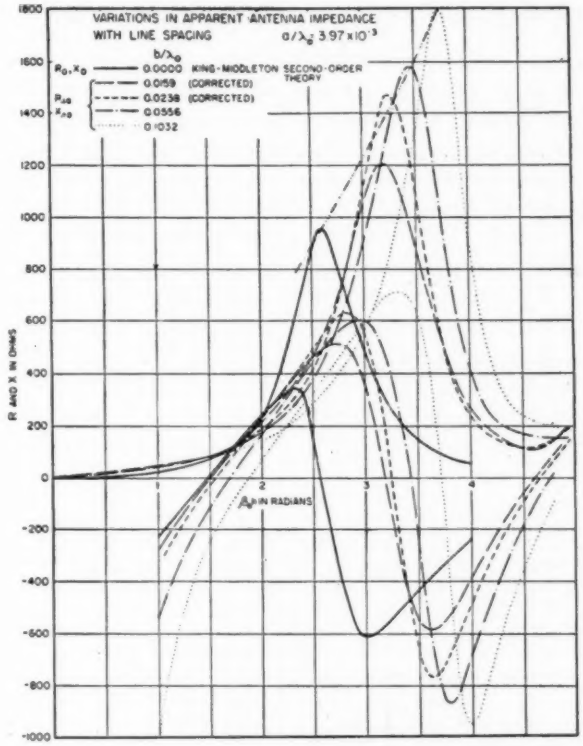

FIG. 25a. Apparent terminal impedances of antennas as center load obtained experimentally by P. Conley on image-plane line together with theoretical curves for antenna driven by slice generator.

symmetrical circuit of Fig. 19b be twice the scalar potential difference across the gap in the circuit of Fig. 19a, the gap must be sufficiently short to make the following condition a good approximation:

$$V_\delta/2 = \phi(\delta) - \phi(0) \doteq \int_0^\delta E_z dz \gg j\omega \int_0^\delta A_z dz. \quad (6.1)$$

For a sufficiently small gap it is reasonable to assume that little error is introduced if the gap is in the conventional form of a hole in the conducting plane as shown in Fig. 20 instead of a slit around the surface of the antenna. The requirement now is

$$V_\delta/2 = \phi(b) - \phi(a) = \int_a^b E_r dr \gg j\omega \int_a^b A_r dr. \quad (6.2)$$

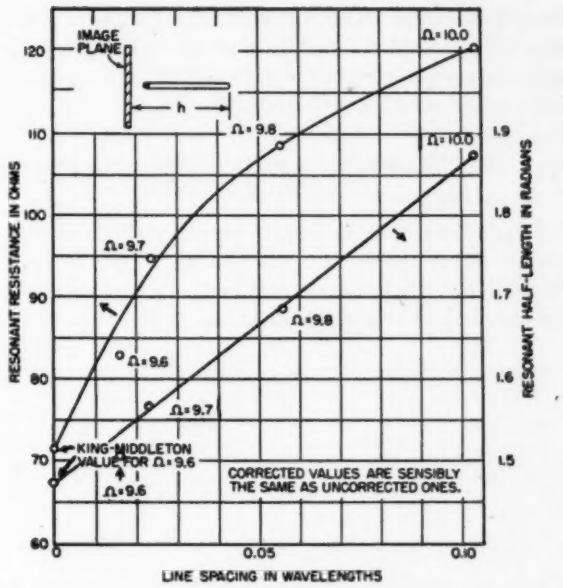

FIG. 25b. Resonant resistances and lengths as determined experimentally by P. Conley with curves extrapolated to theoretical values for slice generator.

A more detailed investigation of the antenna driven from a coaxial line as shown in Fig. 20 is not con-

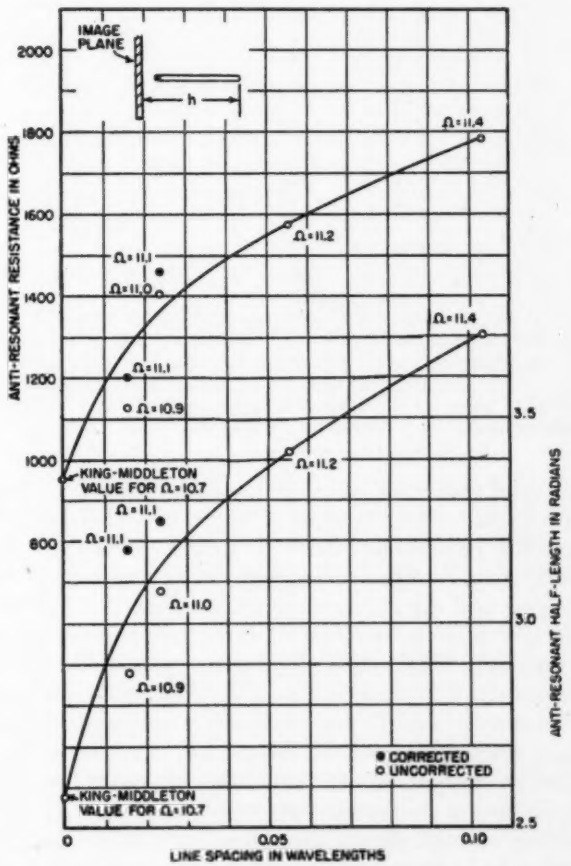

FIG. 25c. Antiresonant resistances and lengths as determined experimentally by P. Conley with curves extrapolated to theoretical values for slice generator.

templated here. The present discussion is intended merely to permit comparison of this arrangement as a more usual alternative to the open-wire line in measuring impedances for cylindrical antennas.

7. THEORETICAL AND EXPERIMENTAL IMPEDANCE CURVES

It has been demonstrated theoretically that the apparent impedance of an antenna as a load on a transmission line may be determined approximately from the theoretical impedance (defined as the ratio of scalar potential difference to current) of an isolated antenna with gap if account is taken of coupling- and end-effects near the junction points. This may be done with appropriately determined inductances in series with the antenna and capacitances in parallel with it. Inductive effects usually are quite small, capacitive effects may be surprisingly large. Accordingly, the *general nature* of the possible differences between the apparent impedance of antennas driven from various transmission lines using several methods of connection may be investigated by determining the effect on the admittance and impedance of the isolated antenna of a lumped capacitance in parallel. By allowing the capacitance to assume a range of positive and negative values, a true picture is given of the measurable admittance and impedance under conditions ranging from large positive capacitances due to dielectric supports or binding posts, to correspondingly large negative capacitances encountered in the terminal zone networks of antennas as end-loads, both with and without stub supports, and antennas as center-loads. Since the difference between the impedance Z_δ of the isolated antenna with gap $2\delta=b$ and the impedance Z_0 of the same antenna with $\delta=0$ is small, present purposes are adequately served if the capacitance C is connected in parallel with Z_0 as obtained from the second-order King-Middleton expansion.[3]

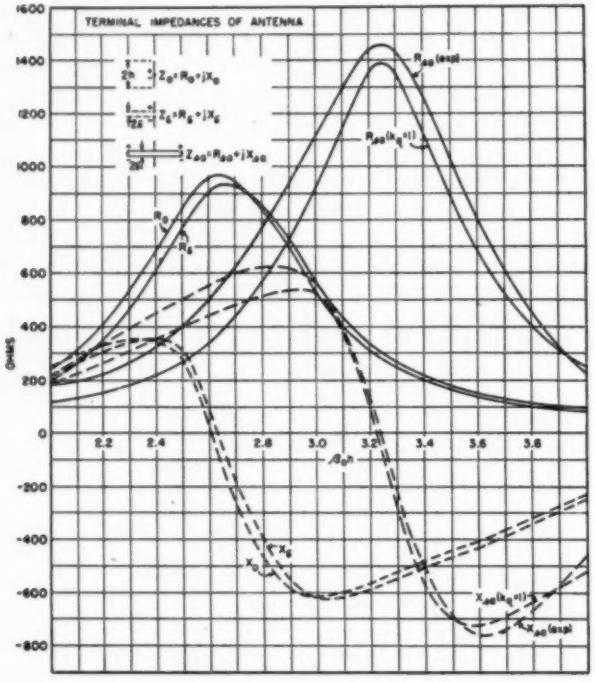

FIG. 26. Theoretical and experimental impedance curves. Z_0 is the King-Middleton second-order impedance for antenna with slice generator; Z_δ is the theoretical impedance for antenna with gap; Z_{ae} is the apparent terminal impedance determined theoretically using Z_δ with terminal-zone network and measured experimentally by P. Conley on image-plane line.

In Figs. 21–23 are shown curves of B_0, R_0, and X_0 in parallel with a lumped capacitance,

$$C_S=K\beta_0 h/\omega=Kh/v_0, \tag{7.1}$$

where K is a constant parameter to which a range of positive and negative values is assigned. G_0 is unaffected by a capacitance in parallel. The independent variable is $\beta_0 h$, the radian half-length of the center-driven antenna. If C is assumed to be a fixed constant,

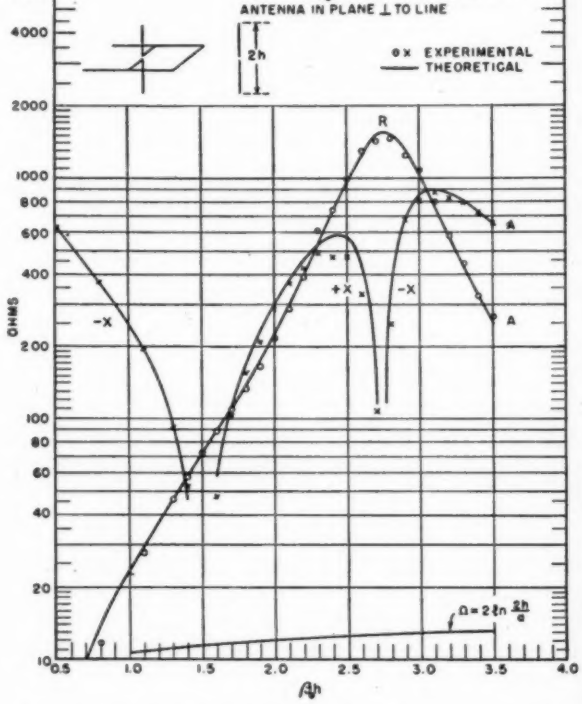

FIG. 27. Apparent terminal impedance of antenna in plane perpendicular to two-wire line. Theoretical curves are King-Middleton second-order impedance, experimental points determined by K. Tomiyasu using dielectric and stub supports adjusted to give maximum voltage at terminals of antenna when this was removed.

$\beta_0 h=\omega h/v_0$ is varied by changing the frequency in $\omega=2\pi f$. The curves marked $K=0$ are for the antenna alone. Note that a *positive* capacitance in parallel, as with a dielectric support, leads to reduced magnitudes of resistance and reactance with shifts of antiresonance

to smaller values of $\beta_0 h$. Conversely, a *negative* capacitance in parallel increases the magnitudes of resistance and reactance very appreciably if K is not too great, and produces a shift of antiresonance to much greater values of $\beta_0 h$. It is clear that the nature of the admittance or impedance of an antenna is greatly modified by a capacitance in parallel. For example, the curves for $K=0$ would be quite inadequate to describe the apparent impedance of antennas and terminal zones for which $K=-0.0003$ or $K=+0.0003$.

In Figs. 24a and 24b are shown the calculated resistance and reactance curves and one experimental pair[9] for a particular antenna and line. Curves A give the real and imaginary parts, R_s and X_s, of the ratio of scalar potential difference to current for an isolated antenna driven by a fictitious generator. Curves E give the apparent terminal impedance $Z_{sa}=R_{sa}+jX_{sa}$ of the *same* antenna used as end-load in the plane of the two-wire line (Fig. 6). Curves S are for the *same antenna and transmission line* as E but with an added high impedance-stub support (Fig. 15). Similarly, curves C (which are the same as curves S) are for the same antenna when connected as center-load on a line symmetrically driven at both ends, as in Fig. 10. Note that the curves are shifted to longer electrical lengths for antiresonance and greater magnitudes of impedances in proportion to the negative shunt capacitances of the appropriate terminal-zone networks.

The dotted curves M_s were obtained experimentally with the particular antenna for which the theoretical curves were evaluated;[9] a high impedance-stub support was used as in Fig. 15. Note that agreement between the experimental curves M_s and the curves A for the isolated antenna with fictitious generator is very poor. On the other hand, the agreement with curves S, obtained using the values of curves A in conjunction with the appropriate terminal zone network, is quite good. As predicted, the attempt to correct for a distributed coupling- and end-effect by lumped elements evaluated for antiresonant conditions ($k_q=1$) is not quantitatively exact. But whereas curves A are almost useless in attempting to predict the experimental curves M_s, curves S are adequate for many practical purposes.

In Fig. 25a are shown curves of R_{sa} and X_{sa} determined experimentally [10] for an antenna connected as center-load in the plane of a transmission line symmetrically driven at both ends (Fig. 10) for four values of the ratio of line spacing to wave-length.[10] Theoretical curves of R_0 and X_0 (King-Middleton second-order) for the same antenna driven by a "slice" generator are also shown. Owing to a slight bow in the image plane the two sets of experimental curves for the smaller values of b/λ_0 involve considerable error for which an approximate correction was introduced.[10] In Fig. 25b are resonant and antiresonant lengths and resistances. The effect of the line spacing on the apparent impedance

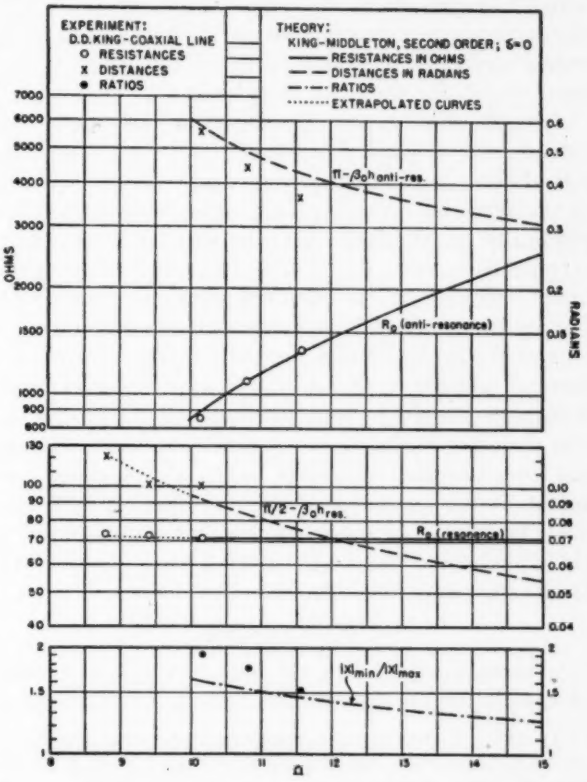

FIG. 28. Theoretical antenna impedances for slice generator with coaxial-line measurements by D. D. King.

is great. In Fig. 26 one of the pairs of curves for R_{sa} and X_{sa} in Fig. 25a is reproduced together with the corresponding theoretical values of R_0 and X_0, R_s and X_s for the antenna with gap 2δ, and of R_{sa} and X_{sa} using the appropriate terminal zone network with elements computed from the constants of the particular line. The experimental curves are seen to be in very much better agreement with the theoretical curves of R_{sa} and X_{sa} than with R_0 and X_0 or R_s and X_s. Note that the maxima of the experimental curves of R and X are relatively too high as seen from Fig. 25a. Actually, experimental and theoretical maxima are almost coincident if interpolated experimental values are used. Unfortunately, the theoretical values of R_{sa} and X_{sa} for the two larger values of b/λ_0 cannot be determined due to the limitation of the theory to small values of b/λ_0.

As a final test of the new theory, Fig. 27 shows theoretical curves of R_s and X_s for an isolated antenna with gap 2δ and fictitious generator together with experimental points[9] for an antenna connected as end-load pependicular to and in the neutral plane of the transmission line, as in Fig. 17. The stub and dielectric supports were adjusted to give maximum voltage at the

[9] K. Tomiyasu, "Problems of measurement on two-wire lines with application to antenna impedances," Cruft Lab. Tech. Rep. No. 48 (June 15, 1948). K. Tomiyasu, "Antennas and open-wire lines, part II, measurements on two-wire lines," J. App. Phys. (to be published).

[10] P. Conley, "Impedance measurements on open-wire lines," Cruft Lab. Tech. Rep. No. 35 (March 18, 1948). P. Conley, "Antennas and open-wire lines, part III, image-line measurements," J. App. Phys. (to be published).

load terminals before the antenna was attached. The connecting half-bridges were of large cross section so that their series inductance was negligible.

As predicted for this special case in which there is virtually no coupling between antenna and line, and in which line end-effects are compensated experimentally, the apparent terminal impedance Z_{aa} is the *same* as the theoretical ratio of scalar potential difference to current, *viz.*, Z_δ for the isolated antenna.

For all other types of connection previously discussed such an equivalence can exist only in the theoretical limit as the line spacing, and with it the length of the terminal zone, approach zero. This limit, while physically unattainable, may be defined by graphical extrapolation as in Fig. 25b and so serve as an operational definition of the idealized slice generator. It has already been shown[11] that for an antenna driven from a coaxial line in the arrangement of Fig. 20, the apparent terminal impedance Z_{aa} is closely approximated by Z_0 in parallel with the lumped positive capacitance due to a thin dielectric wafer at the junction between antenna and line, provided the inner radius of the outer conductor of the coaxial line at this junction is a very small fraction of a wave-length. This is illustrated in Fig. 28 where compensated critical data obtained by King[11] are compared with theoretical values.

8. CONCLUSION

An approximate theory has been derived and verified for calculating the measurable, apparent impedance of an antenna loading an open-wire line in several arrangements. Use is made of conventional transmission-line theory and antenna theory together with a properly designed terminal-zone network that takes account of transmission-line end-effects and coupling between antenna and line. In this way the King-Middleton second-order impedances as generalized to a finite gap by King and Winternitz are shown to lead to good agreement with impedances measured on open-wire and coaxial lines using widely different connections. These measured impedances differ greatly.

Significantly, the new theory is not limited to antennas, but applies equally to *all types of load*. It constitutes an essential supplement to conventional transmission-line theory whenever an increase in the length of the line by an amount equal to its spacing produces *more* than a *negligible* change in impedance. For example, the new theory has been applied to open-end and bridged-end transmission lines to determine end-corrections. It may also be applied to discontinuities.

[11] D. D. King, "Measured impedance of cylindrical dipoles," Cruft Lab. Tech. Rep. No. 2 (July 19, 1946); J. App. Phys. **16**, (October, 1946).

ACKNOWLEDGMENTS

The writer is grateful to Dr. K. Tomiyasu and Dr. P. Conley for permission to include their major experimental results in this part of the paper (instead of retaining them in their respective parts) to facilitate comparison with theory. Dr. C. T. Tai kindly read the manuscript. Most of the computations and the drafting were supported by the Navy Department (ONR) and the Signal Corps.

Potential Functions for a Thermionic Vacuum Tube

E. C. Okress

Westinghouse Electric Corporation, Lamp Division, Bloomfield, New Jersey

(Received February 21, 1949)

Space charge free potential functions for a particular type of thermionic vacuum tube are derived and represented graphically for four sets of boundary conditions. The geometry under consideration comprises two spaced parallel equipotential metallic planes between which are three symmetrically interposed planes of spaced metallic strands. The strands are mutually parallel in their respective planes, though the strands in planes adjacent to the equipotential surfaces are both orthogonal to those in the central plane. This structure is divided principally into two planes, due to the orthogonal relationship between the strands in the central and adjacent planes. These two planes are each conformally transformed such that the analysis thereof yields the desired potential functions for the original structure, neglecting edge effects. Finally, the theoretical results are applied to a typical commercial thermionic vacuum tube.

I. INTRODUCTION

THE object of this exposition is primarily the derivation of potential distribution functions by the application of conformal transformations for a type of geometry illustrated essentially by Fig. 1.

Although, either (a) the experimental method, involving electrolytic tank field plotting,[1] or the (b) relaxation method,[2] involving the solution of Laplace's equation by first reducing it to a system of difference or algebraic equations which are solved by an arithmetical technique due to R. V. Southwell,[2] or the (c) conformal transformation method[3–5] may be used

[1] L. M. Myers, *Electron Optics* (D. Van Nostrand and Company, Inc., New York, 1939), pp. 129–142.

[2] R. V. Southwell, *Relaxation Methods in Theoretical Physics* (Oxford University Press, London, 1946).

[3] G. Julia, *Representation Conforme* (Gauthier-Villars, Paris, 1931).

to derive the potential functions desired. Often, as in the present case, the last method is the most appropriate.

The general expression for the potential function involving the particular geometry under consideration is derived and represented by expression (8). This expression is then evaluated for each of four boundary conditions,

(a) between the grid and filament strands,
(b) between the grid and through the filament strands,
(c) between the filament and through the grid strands,
(d) through the grid and filament strands,

encountered with a typical thermionic vacuum tube. The resulting potential functions are illustrated in graphical form by Figs. 6 through 9.

As illustrated by Fig. 1 the geometry under consideration comprises two spaced parallel equipotential planes 1,1 between which are symmetrically interposed planes 2,2 and 3 of isolated metallic strands. The strands in planes 2,2 are mutually parallel to those in plane 3 also, but strands in planes 2,2 are orthogonal to those in plane 3 as shown. Planes 1,1 are at a prescribed unipotential value, E_p. These planes are referred to as the anode or plate. Strands in planes 2,2 are also at a prescribed potential E_G with respect to potential E_C of the strands in assemblage 3. Planes 2,2 are referred to as the grids and plane 3 as the cathode or filaments.

This structure is next represented on a composite plane commonly referred to as the W plane. This plane is comprised of two corresponding parts of the structure illustrated by Fig. 1 and will be referred to as the W_1 and W_2 planes. The former of these two planes pertains to the filament as center, as illustrated by Fig. 2a, whereas the other pertains to the grid as center, as illustrated by Fig. 2b. Finally, in order to derive the potential functions in the original structure, Fig. 1, it is expedient to transform conformally the composite W plane into a composite Z plane. The Z plane is necessarily composite and constitutes transformations of the two corresponding parts of Fig. 2. As illustrated by Fig. 3a and Fig. 3b these are referred to as ZX and YX transformations. The type of conformal transformation resorted to may be represented by the complex function $W=\ln Z$. From the theory of functions of a complex

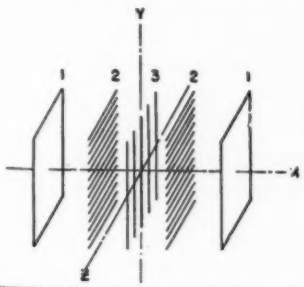

FIG. 1. Structure under consideration, comprising metallic planes 1,1 with metallic strands in planes 2,2 orthogonal to those in plane 3.

[4] C. Caratheodory, "Conformal Representation," Cambridge Tract 28 (Cambridge University Press, London, 1932).
[5] W. G. Dow, *Fundamentals of Engineering Electronics* (John Wiley and Sons, Inc., New York, 1937), Chapter 2.

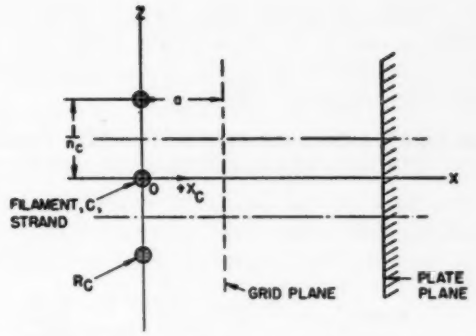

FIG. 2a. The W_1 plane with a strand in plane 3 of Fig. 1, e.g. the filament as center of coordinates.

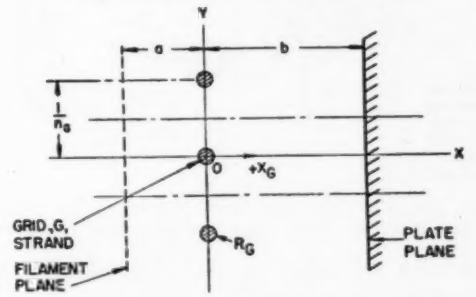

FIG. 2b. The W_2 plane with a strand in plane 2 of Fig. 1, e.g. the grid as center of coordinates.

variable it is shown that equipotential surfaces and field lines retain their original relationship by such transformation. Hence, the self and mutual capacitances and potentials between elements remain invariant as a result of such conformal transformations. With the aid of these transformations the potential function is derived and evaluated for each of the four important boundary conditions previously outlined.

The physics of thermionic vacuum tubes involves an important well-known constant referred to as the amplification factor, μ. It represents a measure of the relative effectiveness of the control grid and plate potentials in the determination of the electric field strength at an infinitesimal distance from the filament or cathode surface. This constant is derivable with the aid of the potential function (8). Explicitly, the amplification factor is expressed as a ratio of potential coefficients, (9) and (10), from relation (15). It is also expressible in terms of geometric factors, by expressions (13) or (14). Incidentally, the application of conformal transformation for the evaluation of the amplification factor was made early by King,[6] Vogdes and Elder,[7] and others.

The derived potential functions are applicable with a fair degree of approximation to structures of the type illustrated by Fig. 1 and under restrictions set forth in the analysis. Aside from the neglect of space charge and edge effects, the treatment is approximate to the extent that the derivation of *exact* electron trajectories

[6] R. W. King, Phys. Rev. **15**, 256 (1920).
[7] F. B. Vogdes and F. R. Elder, Phys. Rev. **24**, 683 (1924).

is not strictly derivable with the aid of the present potential functions. An appropriate application of the theoretical results to a typical commercial thermionic vacuum tube terminates the work.

II. THE DERIVATION OF THE POTENTIAL FUNCTION BY CONFORMAL TRANSFORMATION, METHOD C

In the light of the geometry revealed by Fig. 1, W_1 and W_2 half planes are constructed as shown in Figs. 2a and 2b. This follows as a consequence of the

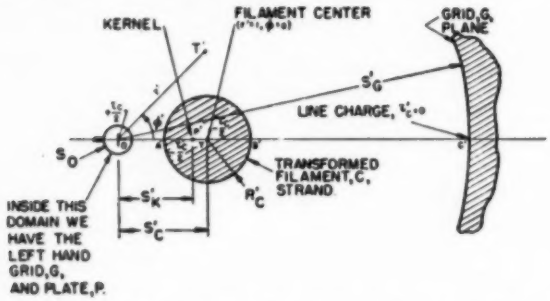

FIG. 3a. The XZ conformal transformation with a strand in plane 3 of Figs. 1 and 2a, e.g. the filament as center.

relation that the structure on either side of the YZ plane in Fig. 1 is identical.

First, the W_1 plane is transformed into a ZX plane as shown in Fig. 3a. In the W_1 plane, the origin, i.e. the position of the filament center, Y, is represented by the coordinates

$$\phi' = 2\pi n_C Z = 0,$$

and

$$r' = e^{2\pi n_C X_C},$$

in the ZX transformation. The size of the filament strand is represented by the coordinates

$$\phi' = 0,$$
$$r'_{A'} = e^{2\pi n_C(-R_C)},$$

and

$$r'_{B'} = e^{2\pi n_C R_C}.$$

The position of the grid plane is represented by the coordinates

$$\phi' = 0,$$

and

$$r'_{C'} = e^{2\pi n_C a}.$$

Note that, in the ZX transformation, all elements to the left of the filament C in the W_1 plane makes $r' \to 0$ rapidly, but not negative. Hence, in the minute domain about the polar origin exists the left-hand grid and plate. Furthermore, no passage is permitted through the grid plane as this is assumed to be the immediate boundary by virtue of the fact that the grid strands are orthogonal to the filament strands.

Next, the W_2 plane is transformed into a YX transformation, Fig. 3b. In the W_2 plane the origin, i.e. the position of the grid center, is represented by the coordinates

$$\phi'' = 2\pi n_G Y = 0,$$

and

$$r'' = e^{2\pi n_G X_G} = 1,$$

in the YX transformation. The size of the grid strand is represented by the coordinates

$$\phi'' = 0,$$
$$r''_{A''} = e^{2\pi n_G(-R_G)},$$

and

$$r''_{B''} = e^{2\pi n_G R_G}.$$

The position of the plate is given by the coordinates

$$\phi'' = 0$$

and

$$r''_{C''} = e^{2\pi n_G b}.$$

Now, note that in the YX transformation, all elements to the left of the grid strand, G, in the W_2 plane makes $r'' \to 0$ rapidly. Hence, in the minute domain about the polar origin exists the filament, the left hand grid and plate. In other words, the complete W_1 plane or ZX transformation exists in the minute domain about the polar origin.

Consider the ZX transformation again and select any point on the filament surface, such as A' for which $\phi' = 0$, and any other point in space, such as T'. These are to be kept invariant in position during the formulation of the subsequent potential expressions. In this ZX transformation, the potential difference between T' and A' with $\phi' = 0$, due to a positive whole charge,[8] $+\tau_{C'}$ at the grid center is represented by

$$E_{T'} - E_{A'} = -2(+\tau_{C'}) \ln \frac{r'}{(S_{C'} - R_{C'})}. \quad (1)$$

Next, due to a negative whole charge, $-\tau_{C'}$, at the filament kernel the potential difference is

$$E_{T'} - E_{A'} = -2(-\tau_{C'}) \times \ln \frac{[(r')^2 + (S_{K'})^2 - 2r'S_{K'}\cos\phi']^{\frac{1}{2}}}{R_{C'} - (S_{C'} - S_{K'})}, \quad (2)$$

where the numerator of the logarithm corresponds to $T'P'$ in Fig. 3a and the denominator thereof corresponds to $A'P'$. Finally, due to a negative whole charge, $-\tau_{C'}$, at the filament center the potential difference is

$$E_{T'} - E_{A'} = -2(-\tau_{C'}) \times \ln \frac{[(r')^2 + (S_{C'})^2 - 2r'S_{C'}\cos\phi']^{\frac{1}{2}}}{R_{C'}}, \quad (3)$$

where the numerator of the logarithm corresponds to $T'Y$ in Fig. 3a and the denominator thereof corresponds to $A'Y$. As a consequence of the three whole charges the total potential difference is (observing that $E_{A'} = E_{C'}$)

$$E_{T'} - E_C = -2(+\tau_{C'}) \ln \frac{r'}{(S_{C'} - R_{C'})} - 2(-\tau_{C'}) \ln \frac{1}{R_{C'}\{R_{C'} - (S_{C'} - S_{K'})\}} \times \{[(r')^2 + (S_{K'})^2 - 2r'S_{K'}\cos\phi'] \times [(r')^2 + (S_{C'})^2 - 2r'S_{C'}\cos\phi']\}^{\frac{1}{2}}.$$

[8] Line charges are referred to unless otherwise stated.

Since, the path between the filament and plate planes is characterized by the value of ϕ' in Fig. 3a, it is appropriate, for illustrative purposes at least, to consider only two paths, i.e. centrally through and halfway between strands which correspond to $\phi'=0$ and π, respectively. Furthermore, recalling that the characteristics of the composite Z plane entails only magnitudes of distances, it follows that

$$E_{T'}-E_C=2(-\tau_C')\ln\frac{r'}{(S_C'-R_C')}+2(-\tau_C')\ln\frac{R_C'\{R_C'-(S_C'-S_K')\}}{|r'\pm S_K'||r'\pm S_C'|}.$$

Now, from potential theory $(S_C')^2-1=(R_C')^2$ and $S_K'=1/S_C'$ so that, using half of the previous whole charges, the above expression assumes the form

$$E_{T'}-E_C=(-\tau_C')\ln\frac{(R_C')^2}{|S_C'\pm 1/r'||r'\pm S_C'|}. \quad (4)$$

Next, the YX transformation, Fig. 3b will be analyzed. The potential difference between T'' and S_C with $\phi''=0$, due to a positive whole charge, $+\tau_C''$, at the grid kernel is represented by

$$E_{T''}-E_C=-2(+\tau_C'')\times\ln\frac{[(r'')^2+(S_K'')^2-2r''S_K''\cos\phi'']^{\frac{1}{2}}}{(S_K''-S_C)}. \quad (5)$$

The potential difference between T'' and S_C, $\phi''=0$, due to a negative whole charge, $-\tau_P''$, at the grid center is represented by

$$E_{T''}-E_C=-2(-\tau_P'')\times\ln\frac{[(r'')^2+(S_G'')^2-2r''S_G''\cos\phi'']^{\frac{1}{2}}}{(S_G''-S_C)}. \quad (6)$$

The potential difference between T'' and S_C with $\phi''=0$, due to half of the two whole aforementioned charges, is expressed as

$$E_{T''}-E_C=-(-\tau_P'')\ln\frac{[(r'')^2+(S_G'')^2-2r''S_G''\cos\phi'']^{\frac{1}{2}}}{S_G''}-(+\tau_C'')\ln\frac{[(r'')^2+(S_K'')^2-2r''S_K''\cos\phi'']^{\frac{1}{2}}}{S_K''}.$$

for case I, i.e., when $S_C\ll S_K$, S_G.

As previously discussed, paths for which $\phi'=0$ and π will only be considered. Hence, the above expression reduces to

$$E_{T''}-E_C=-(-\tau_P'')\ln|r''/S_G''\pm 1|-(+\tau_C'')\ln|S_G''r''\pm 1|, \quad (7)$$

since $S_K''=1/S_G''$ as a consequence of potential theory.

From the foregoing it should be noted that although ϕ' and r' are derived from transformation ZX, whereas ϕ'' and r'' are derived from transformation YX, the former variables are independent of the latter. Incidentally, when the chosen angles ϕ' and ϕ'' each exceed the secant angles of the transformed filament and grid circles, respectively, the coordinates are off the respective strands.

Now, expressions (4) and (7) are next combined to obtain the over-all potential at any point, $T'=T''=T$, i.e.

$$E_T=-\tau_C'\ln\frac{(R_C')^2}{|S_C'\pm 1/r'||r'\pm S_C'|}+\tau_P''\ln|r''/S_G''\pm 1|-\tau_C''\ln|S_G''r''\pm 1|,$$

for $2E_C=0$. Since

$$\sigma_C''\{=n_G(-\tau_C'')\}=\sigma_C'\{=n_C(-\tau_C')\}$$

or

$$(-\tau_C'')=(n_C/n_G)(-\tau_C'),$$

the above expression for potential becomes

$$E_T=(-\tau_C')\left\{\ln\frac{(R_C')^2}{|S_C'\pm 1/r'||r'\pm S_C'|}+(n_C/n_G)\times\ln|S_G''r''\pm 1|\right\}+(+\tau_P'')\ln|r''/S_G''\pm 1|, \quad (8)$$

which represents the general potential function for the system of Fig. 1. It should be recalled that this expression is valid only for case I, i.e. when $S_C\ll S_G$. It is necessary to return to the basic expressions (5) and (6)

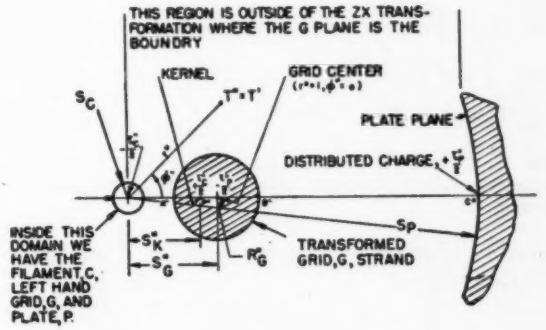
THIS REGION IS OUTSIDE OF THE ZX TRANSFORMATION WHERE THE G PLANE IS THE BOUNDRY
KERNEL
GRID CENTER
PLATE PLANE
DISTRIBUTED CHARGE
INSIDE THIS DOMAIN WE HAVE THE FILAMENT,C, LEFT HAND GRID,G, AND PLATE,P.
TRANSFORMED GRID,G, STRAND

FIG. 3b. The YX conformal transformation with a strand in plane 2 of Figs. 1 and 2b, e.g. the grid as center.

in order to derive the general potential function for case II, i.e. when the aforementioned condition is not valid.

Continuing the consideration of case I, particular solutions of (8) are required for the plate to cathode and grid to cathode potentials in terms of potential coefficients and charges in the expression (8). These are obtained by first putting T *on* the plate, such that when

$$\phi'=0,\quad r'=e^{2\pi nC(a+b)},$$

and when $\phi''=0$, $r''=e^{2\pi nGb}$ are substituted in ex-

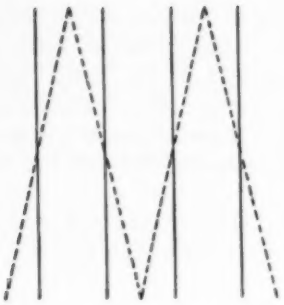

FIG. 4. The actual W filament approximated by a parallel strand type, for case I of the analysis.

pression (8), the plate to filament potential,

$$E_P-E_C=(-\tau_C')\left\{\ln\frac{(R_C')^2}{\left|S_C'-\frac{1}{e^{2\pi nC(a+b)}}\right|\left|e^{2\pi nC(a+b)}-S_C'\right|}+\frac{n_C}{n_G}\ln\left|S_G''e^{2\pi nGb}-1\right|\right\}+(+\tau_P'')\ln\left|\frac{e^{2\pi nGb}}{S_G''}-1\right|, \quad (9)$$

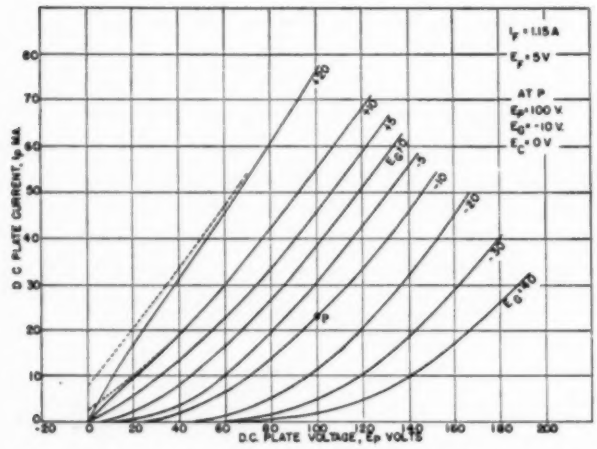

FIG. 5. Conventional static plate characteristic curves for a typical thermionic vacuum tube structure considered in the example.

is readily obtained. Then, by putting T *on* the grid, such that when

$$\phi'=0, \quad r'=e^{2\pi nCa},$$

and when $\phi''=0$, $r''=S_G''\pm R_G''$ are substituted in expression (8), the grid to filament potential,

$$E_G-E_C=(-\tau_C')\left\{\ln\frac{(R_C')^2}{\left|S_C'-\frac{1}{e^{2\pi nCa}}\right|\left|e^{2\pi nCa}-S_C'\right|}+\frac{n_C}{n_G}\ln\left|S_G''(S_G''\pm R_G'')-1\right|\right\}+(+\tau_P'')\ln\left|\pm R_G''/S_G''\right|, \quad (10)$$

results.

Relations (9) and (10) may be written in terms of the potential coefficients, A_1, A_2, B_1, B_2, and the charges, τ_C' and τ_P'', as

$$\left.\begin{aligned}E_P&=A_1(-\tau_C')+A_2(+\tau_P'')\\ \text{and}\quad E_G&=B_1(-\tau_C')+B_2(+\tau_P'')\end{aligned}\right\}, \quad (11)$$

where the potential coefficients are

$$A_1=\ln\frac{(R_C')^2}{\left|S_C'-\frac{1}{e^{2\pi nC(a+b)}}\right|\left|e^{2\pi nC(a+b)}-S_C'\right|}+\frac{n_C}{n_G}\ln\left|S_G''e^{2\pi nGb}-1\right|. \quad (12a)$$

$$A_2=\ln\left|\frac{e^{2\pi nGb}}{S_G''}-1\right|\simeq\ln\frac{e^{2\pi nGb}}{S_G''}, \quad (12b)$$

$$B_1=\ln\frac{(R_C')^2}{\left|S_C'-\frac{1}{e^{2\pi nCa}}\right|\left|e^{2\pi nCa}-S_C'\right|}+(n_C/n_G)\ln\left|S_G''(S_G''\pm R_G'')-1\right|, \quad (12c)$$

and

$$B_2=\ln\left|\pm R_G''/S_G''\right|. \quad (12d)$$

Expression (8) can be solved with the aid of (11), from which the charges, τ_C' and τ_P'', are derived in terms of specified values of E_P and E_G.

III. THE AMPLIFICATION CONSTANT, μ

With an aspect to completeness it is now appropriate to formulate the relations for the amplification constant, μ, for the geometric structure under consideration, Fig. 1. This constant is a measure of the grid and plate potentials in the determination of the electric field strength that exists just off the filament (or cathode) surface, in the absence of space charge. Hence, the amplification constant, μ, can be expressed in terms of the potential coefficients, (12b) and (12d), that is

$$\mu=-\frac{A_2}{B_2}\simeq-\frac{\ln(e^{2\pi nGb}/S_G'')}{\ln S_G''/R_G''}. \quad (13)$$

Since $S_G''=\cosh 2\pi n_G R_G$ and $R_G''=\sinh 2\pi n_G R_G$,

$$\mu=\frac{(2\pi n_G b-\ln\cosh 2\pi n_G R_G)}{\ln\coth 2\pi n_G R_G}, \quad (14)$$

as usual.

This expression is also valid so long as the distance between the filament and grid is such as to justify that $S_C\ll S_G$ in the Z plane. When this condition is not fulfilled the coefficients in (13) must be derived directly from expressions (5) and (6) as they stand.

The amplification constant can also be represented in terms of the previously derived potential distribution function, that is

$$\mu=-(E_P-E_C)/(E_G-E_C),$$

at cut off.

IV. A PRACTICAL EXAMPLE

To illustrate the foregoing theory and particularly to apply it, a thermionic vacuum tube is selected which approximately fulfills the essentials of the geometry portrayed by Fig. 1. The Western Electric type 104D

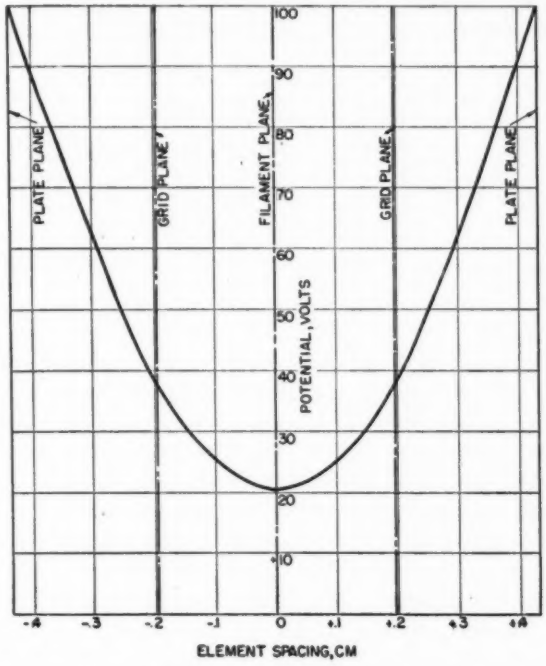

FIG. 6. Theoretically derived potential distribution between plates, along a path halfway between grid and filament strands of Fig. 1.

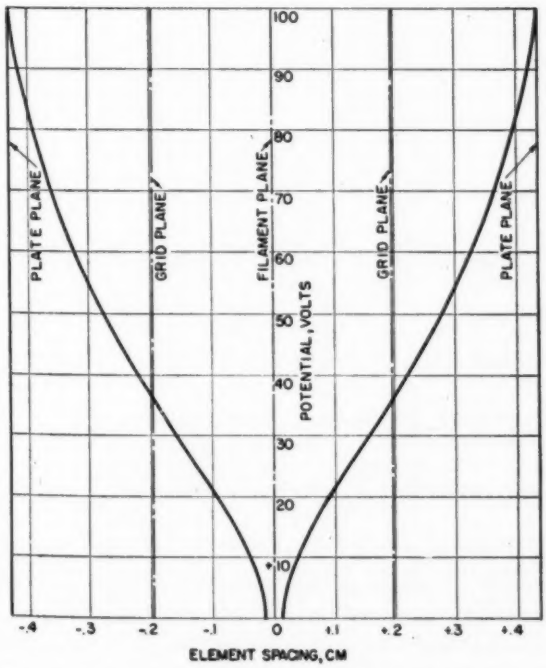

FIG. 7. Theoretically derived potential distribution between plates, along a path halfway between grid strands and centrally through filament strands of Fig. 1.

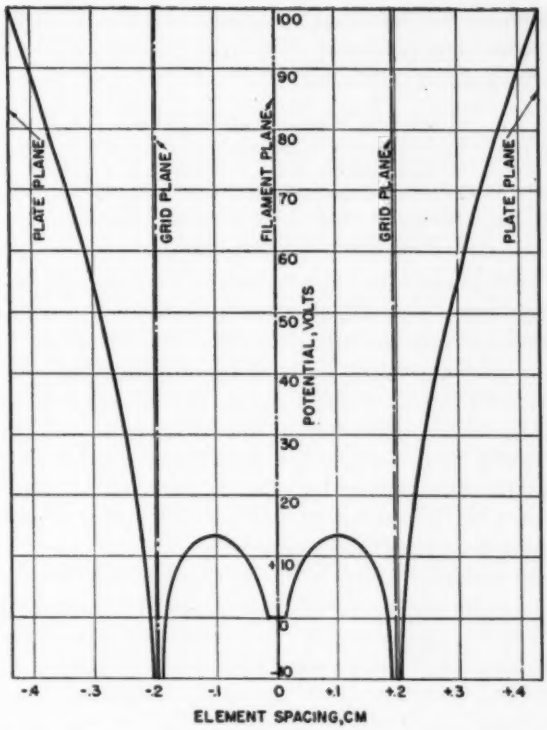

FIG. 8. Theoretically derived potential distribution between plates, along a path centrally through grid and filament strands of Fig. 1.

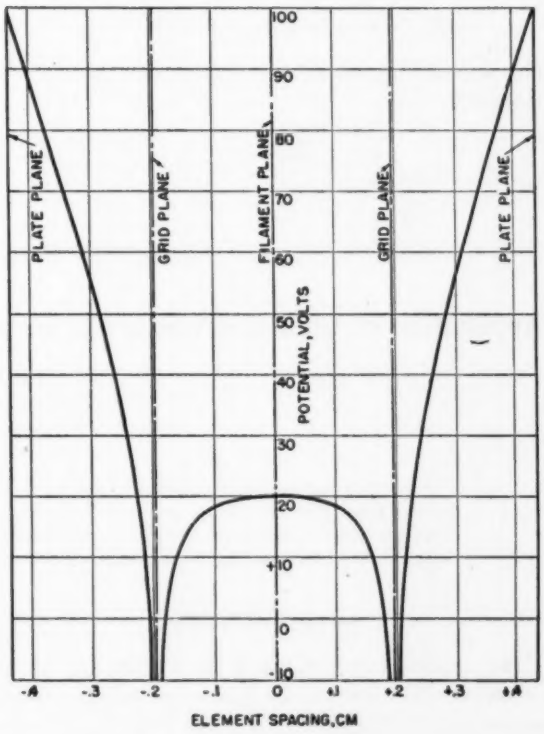

FIG. 9. Theoretically derived potential distribution between plates, along a path halfway between filament strands and centrally through the grid strands of Fig. 1.

thermionic vacuum tube is suitable for the immediate purposes. The pertinent geometric data obtained from the dismantled tube are:

Grid strand radius, $R_G=0.00825$ cm,
Grid strand pitch, $n_G=2.53$ strands/cm,
Grid to plate distance, $b=0.239$ cm,
Filament to grid distance, $a=0.195$ cm,
Filament strand radius, $R_C=0.0128$ cm,
Filament strand pitch, $n_C=2$/cm.

The filament wire pitch is derived from an equivalent model. The actual filament configuration in the chosen thermionic vacuum tube is an inverted W shape filament, 13.0 cm long. To simplify the analysis it was considered valid, in the light of the assumption that $S_C \ll S_G$, to treat the actual filament geometry as symmetrically disposed parallel strands orthogonal to the grid wires as shown in Fig. 4.

The plate characteristics of the chosen thermionic vacuum tube are illustrated by Fig. 5.

The potential function (8) is evaluated for this tube in the following manner: The values of the potential coefficients (12a) through (12d) in expressions (11) are computed by merely substituting the corresponding geometric constants and potential differences. Then, the charges τ_C' and τ_P'' in expressions (11) are solved for and substituted in the potential function, (8). From the foregoing geometric data it is evident that

$$S_C'=\cosh 2\pi n_C R_C=1.013,$$
$$S_G''=\cosh 2\pi n_G R_G=1.008,$$
$$R_C'=\sinh 2\pi n_C R_C=0.1607, \text{ and}$$
$$R_G''=\sinh 2\pi n_G R_G=0.1304.$$

The selected operating point with reference to Fig. 5 is defined by

$$E_P=100 \text{ volts},$$
$$E_G=-10 \text{ volts, and}$$
$$E_C=0.$$

These are substituted in expressions (11) to yield the charges,

$$(-\tau_C')=-.0138 \text{ statcoulomb}$$

and

$$(+\tau_P'')=+.0678 \text{ statcoulomb}.$$

Upon substitution of these charges in expression (8) with pertinent other factors the potential function,

$$E=-0.0138\left\{\ln\frac{0.0258}{\left|1.013\pm\frac{1}{r'}\right|\,|r'\pm 1.013|}+0.790\ln|1.008r''\pm 1|\right\}+0.0678\ln\left|\frac{r''}{1.006}\pm 1\right|,$$

is obtained.

This particular potential function is next evaluated, with the previously fixed values of E_P, E_G and E_C, for the following four important cases, between plates along a path (a) halfway between grid and filament strands, i.e. for $\phi'=\phi''=\pi$, (b) halfway between grid strands though centrally through the filament strands, i.e. for $\phi'=0$, $\phi''=\pi$, (c) halfway between the filament strands though centrally through the grid strands, i.e. for $\phi'=\pi$, $\phi''=0$, and (d) centrally through the grid and filament strands, i.e. for $\phi'=\phi''=0$.

It should be recalled that the choice of sign in the absolute terms are dependent upon the chosen values of ϕ' and ϕ''. As previously mentioned, only the two extreme values of these angles were selected. So that whenever these angles are equal to π, in the Z plane, the signs in the absolute terms are simply positive, whereas when zero the sign chosen is negative.

The final results are illustrated by Fig. 6 through 9 and are self-explanatory.

Application of Thermodynamics to Chemical Problems Involving the Oxide Cathode

ADDISON H. WHITE
Bell Telephone Laboratories, Murray Hill, New Jersey
Received February 23, 1949

Computations of the free energy of some chemical reactions involving dissociation or reduction of alkaline earth oxides have been made on the basis of rough estimates of the thermochemical quantities which have not been measured. The resulting values of free energy, equilibrium constant and equilibrium pressure of barium vapor derived for specified ideal conditions are tabulated. Several applications of these results are discussed.

I. INTRODUCTION

THE oxide-coated cathode is a complex system whose chemistry and physics are still the subject of extensive investigation.[1] Over the long history of research in this field there has been very little application of the powerful methods of thermodynamics to the chemistry of reactions involving these alkaline earth oxides.[2] The primary reason for this is the lack of thermochemical data, particularly the high-temperature heat capacities of BaO and SrO. Nevertheless, it is

[1] J. P. Blewett, J. App. Phys. **17**, 643 (1946).

[2] For a review of such applications, see J. P. Blewett, J. App. Phys. **10**, 831 (1939); see also reference (12).

possible to base illuminating calculations on reasonable estimates of such quantities. This paper is designed to provide a tabulation of the results of such calculations made several years ago which, it has since developed, are of interest to a number of workers in the field. It must be emphasized that the free energies of reaction thus derived are only approximations, but at a rough guess are correct to within five kilocalories per mole of BaO or SrO involved.

II. METHOD OF COMPUTATION

The change of the Gibbs free energy accompanying a chemical reaction is

$$\Delta F^\circ(T)=\Delta H(T)-T\Delta S(T), \quad (1)$$

where H and S are respectively the heat content and the entropy.[3] The superscript o indicates as usual that each substance involved in the reaction is conceived to be in its standard state. It is thus sufficient for the calculations below to know ΔH and ΔS for the reactions and temperatures in question. One convenient way to obtain these quantities is to start with the known values of $\Delta H(T_0)$ and $\Delta S(T_0)$ ($T_0=298.1°\text{K}$) in calculating the desired quantities at the higher temperatures of interest, according to

$$\Delta H(T)=\Delta H(T_0)+\int_{T_0}^{T}\Delta C_p dT; \quad (2)$$

$$\Delta S(T)=\Delta S(T_0)+\int_{T_0}^{T}\Delta C_p d\ln T. \quad (3)$$

ΔC_p is the total molar heat capacity at constant pressure of the substances "produced" less that of those "consumed" in the reaction. The molar heat capacities C_p of the substances involved below can all be expressed in the approximate analytical form*

$$C_p=A+BT-CT^{-2}+DT^{-\frac{1}{2}}$$

so that, for any of the reactions involved,

$$\Delta C_p=\Delta A+\Delta BT-\Delta CT^{-2}+\Delta DT^{-\frac{1}{2}}. \quad (4)$$

Equations 1 to 4 yield, after the indicated integrations

$$\Delta F^\circ(T)=\Delta H(T_0)-T\Delta S(T_0)+f_A\Delta A+f_B\Delta B+f_C\Delta C+f_D\Delta D \quad (5)$$

where

$$f_A=T-T_0-T\ln(T/T_0),$$
$$f_B=TT_0-\tfrac{1}{2}(T^2+T_0^2),$$
$$f_C=1/2T-(1/T_0)(1-T/2T_0),$$
$$f_D=4T^{\frac{1}{2}}-2TT_0^{-\frac{1}{2}}-2T_0^{\frac{1}{2}}.$$

These functions of temperature are presented in Fig. 1 with sufficient accuracy for calculations of this type.

The thermochemical data used here are recorded in Table I, together with the sources from which they were obtained. It will be noted below that some of the heat capacity data are employed beyond the temperature range of their validity as specified by the last column of the table. Where data are lacking, the basis of an estimate is briefly indicated in the footnotes appended to the table. In particular the high-temperature molar heat capacities of BaO and SrO are taken to be equal to that of CaO, which has been measured. This is empirically justified by the fact that at 298.1°K the three heat capacities fall within the range from 10.23 to 11.34 calories per degree-mole, and that below room temperature this range decreases with increasing temperature.[4]

The values of free energy obtained as above for twelve chemical reactions at four elevated temperatures are recorded in Table II. The free energy of formation of water in Row 1 is useful for obtaining the free energy for reactions not included here by addition or subtraction according to the standard procedure.[3] Reaction 2 does not occur but is similarly useful in combination with other reactions. Reactions 3 to 12 are relevant to various aspects of the oxide cathode problem.

III. THERMAL DISSOCIATION OF ALKALINE EARTH OXIDES

In order to illustrate the application of the data to problems of interest the equilibrium constants of these reactions have been calculated according to

$$\Delta F^\circ=-RT\ln K,$$

and are recorded in Table III. One problem is to esti-

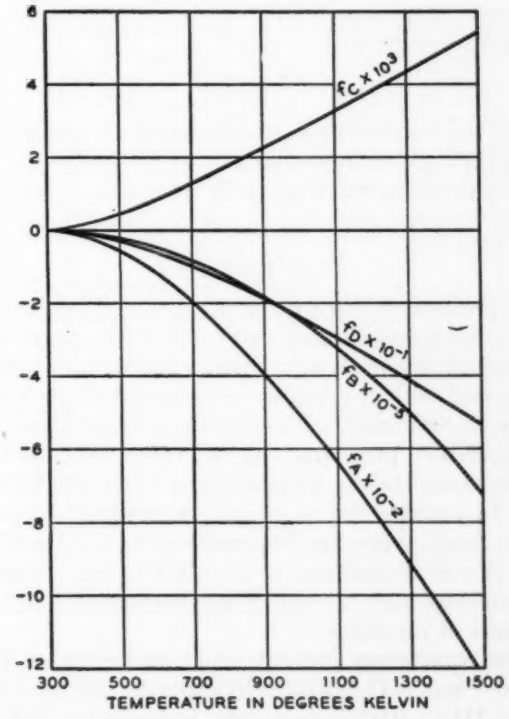

FIG. 1.

[3] See e.g., G. N. Lewis and M. Randall, *Thermodynamics* (McGraw-Hill Book Company, Inc., New York, 1923).

* See Table I, reference (d).

[4] Table I, reference (c).

TABLE I. Thermochemical data employed in free energy calculations.

	$H(T_0)$[a] (Kilocalories/Mole)	$S(T_0)$[a] (E.U./Mole)	$C_p = A + BT - CT^{-2} + DT^{-\frac{1}{2}}$ (calories deg.$^{-1}$ mole^{-1}). A[d]	$B\times10^{3}$[d]	$C\times10^{-5}$[d]	D[a]	Valid range
H_2	0	31.23	5.797[a]	1.003[a]	0	+14.63	273°–2500°K
O_2	0	49.03	9.629[a]	0.369[a]	0	−42.83	300°–2500°
$H_2O(g)$	−57.798[f]	45.17	8.828[a]	1.917[a]	0	−29.58	300°–2500°
$CH_4(g)$	−19.100	44.46	5.34	11.5	0	0	273°–1200°
$CO(g)$	−26.428	47.32	7.74[a]	0.74[a]	0	−20	273°–2500°
$Ba(g)$	(+44.500)[g]	40.67	4.97	0	0	0	All
$BaO(s)$	−133.100	16.8	10.0[h]	4.84[h]	1.080[h]	0	
$Ni(s)$	0	7.1	6.99	0.905	0	0	626°–1725°
$NiO(s)$	−57.830	9.25[i]	13.69[j]	0.83[j]	2.915[j]	0	273°–1373°
$C(gr)$	0	1.36	2.673	2.617	1.169	0	273°–1373°
$Si(s)$	0	4.50	5.74	0.617	1.01	0	273°–1174°
$SiO_2(l)$	−198.300	11.2	12.80	4.47	3.02	0	273°–1973°
$BaSiO_3(s)$	−356.040	28[k]	27.95[l]	2.056[l]	7.456[l]	0	
$Mg(g)$	+35.907[b]	35.51	4.97	0	0	0	All
$MgO(s)$	−145.760	6.4	10.86	1.197	2.087	0	273°–2073°
$Sr(g)$	(+39.2)[m]	39.33	4.97	0	0	0	All
$SrO(s)$	−140.700	13.0	10.0[h]	4.84[h]	1.080[h]	0	
$Ca(g)$	+42.485[b]	37.00	4.97	0	0	0	All
$CaO(s)$	−151.710	9.5	10.00	4.84	1.080	0	273°–1173°

[a] International Critical Tables, Vol. V, p. 169 (1929), unless otherwise specified.
[b] K. K. Kelley, U. S. Bureau of Mines Bulletin 383 (1935).
[c] K. K. Kelley, U. S. Bureau of Mines Bulletin 394 (1936), unless otherwise specified.
[d] K. K. Kelley, U. S. Bureau of Mines Bulletin 371 (1934), unless otherwise specified.
[e] M. deK. Thompson, *Total and Free Energies of Formation of the Oxides of Thirty-two Metals* (Electrochemical Society, New York, 1942).
[f] F. D. Rossini, J. Research, Nat. Bur. Stand. **22**, 407 (1939).
[g] Heat of sublimation assumed independent of temperature and equal to Van Liempt's value, 800°–1050°K (J. A. M. Van Liempt, Rec. Trav. Chim. de Pay-Bas, **55**, 468 (1936).
[h] Assumed equal to values for CaO, $300° < T < 1500°$.
[i] Seltz, DeWitt, and MacDonald, J. Am. Chem. Soc. **62**, 3527 (1940).
[j] A. F. Kapustinski and K. A. Novosel'tsev, J. Phys. Chem. USSR **11**, 61 (1938).
[k] Assumed equal to the sum of $S(T_0)$ for BaO and SiO_2, by analogy with the result observed in $CaSiO_3$.
[l] Assumed equal to values for Wollastonite, $CaSiO_3$, $273° < T < 1573°$.
[m] Taking heat of vaporization of liquid strontium from (*b*) to be 37.046 kilocalories at 298°K, and adding the observed heat of fusion of strontium at 1030°K of 2.190 kilocalories, assuming it to be equal to heat of fusion at 298°K.

mate the pressure of gaseous Ba and O_2 in equilibrium with solid BaO at 1273°K, as compared with its molecular vapor pressure of 4×10^{-7} mm.[5] For this we have to a good approximation[3]

$$K = p_{Ba}{}^2 p_{O_2} \tag{6}$$

where the equilibrium partial pressures identified by the subscripts are expressed in atmospheres. For the ideal case with no source of Ba or O_2 except the dissociating BaO

$$p_{Ba} = 2p_{O_2} = (2K)^{\frac{1}{3}}.$$

This pressure as listed under p_m in the table is 2×10^{-11} mm of mercury, showing that at 1273°K the rate of loss of BaO by dissociation to gaseous products is negligible compared with the loss by evaporation of BaO molecules. In SrO and CaO however similar estimates yield "dissociation pressures" p_m in Table III which are smaller than the vapor pressures by a factor of less than ten. In practice this is of little significance when the pressure of oxygen due to contamination is higher than that due to dissociation of the alkaline earth oxide, in experiments such as the determination of the vapor pressure of this oxide.

The equilibrium pressure of 8×10^{-17} mm of Ba or 4×10^{-17} mm of O_2 obtained by extrapolating the data of Table III to 1000°K may seem in conflict with Dushman's[6] estimate of $<10^{-40}$ atmosphere for the dissociation pressure of BaO at this temperature. However Dushman's result presumably refers to the conventional meaning of the term "dissociation pressure;" i.e., the equilibrium pressure of oxygen above the oxide in the presence of the *solid* metal. This may be obtained from Eq. (6) by setting p_{Ba} equal to the vapor pressure of solid Ba, 1.2×10^{-2} mm at 1000°K.[7] The equilibrium pressure of oxygen thus derived is 2×10^{-45} mm or 3×10^{-48} atmosphere, in agreement with Dushman. Since no such pressures are attainable it is of course concluded that no solid barium nor for that matter any significant concentration of excess barium dissolved in BaO can be obtained by thermal dissociation of BaO at or near 1000°K.

IV. PRODUCTION OF FREE BARIUM

A widely accepted theory of the oxide cathode starts with the assumption that BaO is an excess electronic semiconductor by virtue of a slight stoichiometric excess of barium atoms dissolved in it.[8] The possibility of supplying such excess barium by the reaction of various reducing agents with BaO has been considered from this thermodynamic point of view. The results are shown, in

[5] A. Claassen and C. F. Veenemans, Zeits. f. Physik **80**, 343 (1933).

[6] S. Dushman, Rev. Mod. Phys. **2**, 433 (1930); vd. also J. A. Becker, Trans. Am. Electrochem. Soc. **59**, 209 (1931) and Wagner, Electronics **1**, 178 (1930).

[7] Table I, reference g.

[8] See e.g., J. P. Blewett, J. App. Phys. **10**, 668 (1939) for a review; see also reference (10).

terms of the equilibrium pressure of barium vapor, by the data for Reactions 4 to 10 in Table III. The concentration of excess barium in the solid in equilibrium with this vapor can be estimated as to order of magnitude by assuming that Raoult's law holds over the entire range of solid solubility. Then, since the saturated solution would be in equilibrium with solid or liquid barium,

$$f_{Ba}/f_{Ba}^{\circ}=p_{Ba}/p_{Ba}^{\circ} \qquad (7)$$

where f_{Ba} and f_{Ba}° are, respectively, the equilibrium and the saturated mole fractions of dissolved barium, while p_{Ba}° is the vapor pressure of solid or liquid barium. The value of f_{Ba}° may be taken from Schriel to be of the order of 0.01 at 1400°K.[9] No estimates of f_{Ba} are included in Table III, since p_{Ba} is equally useful for comparing the effectiveness of the various reducing agents. By way of example however, the p_{Ba} of 1 mm at 1473°K obtained from Reaction 5, together with $p_{Ba}^{\circ}=17$ mm and $f_{Ba}^{\circ}=0.01$, yields 6×10^{-4} for the concentration of dissolved barium in equilibrium with 10^{-5} atmospheres of methane.

Reactions 4 and 5 represent procedures that might be employed in a laboratory experiment designed to increase the excess barium content of BaO. The equilibrium pressures of barium vapor tabulated in the last column show that methane at a pressure of 10^{-5} atmosphere is at least 100-fold more effective than hydrogen at one atmosphere in reducing BaO. The low pressure chosen for the methane calculation was that employed in an experiment which is described elsewhere.[10]

Reactions 6 to 10 are related to mechanisms by which BaO might be reduced in a commercial oxide cathode, where the (BaSr)O is in contact with a nickel core containing small concentrations of such impurities or additives as carbon, silicon, and magnesium. Reaction 6 shows that nickel itself can have no effect, since the equilibrium pressure of barium vapor above BaO alone is higher than that above BaO in the presence of both nickel and NiO. In Reaction 7 carbon is shown to have a considerable effect, although it should be emphasized that Reactions 7 to 10 are written for saturated solid solutions of the reducing agent in nickel, whereas the commercial concentrations are probably much lower. Reactions 8 and 9 show that silicon would be much less effective than carbon if it were not for the side reaction between BaO and SiO_2 to form a silicate, here assumed for convenience in calculation to be $BaSiO_3$ rather than the experimentally observed Ba_2SiO_4.[11] It will be noted that the equilibrium constants for Reaction 10 have been calculated for gaseous rather than liquid magnesium. However the barium pressures listed under p_m are derived by taking the pressure of magnesium to be that in equilibrium with its liquid at each temperature.

TABLE II. Free energy changes accompanying certain reactions.

Reaction	ΔF° (Kilocalories) T=873°	1073°	1273°	1473°
1. $2H_2+O_2=2H_2O(g)$	−95	−90	−84	−79
2. $2CH_4+O_2=2CO+4H_2$	−91	−110	−128	−147
3. $2BaO(s)=2Ba(g)+O_2$	273	255	238	221
4. $2SrO(s)=2Sr(g)+O_2$	273	254	236	218
5. $2CaO(s)=2Ca(g)+O_2$	300	280	262	243
6. $BaO(s)+H_2=Ba(g)+H_2O$	89	82	77	71
7. $BaO(s)+CH_4=Ba(g)+CO+2H_2$	91	73	55	37
8. $BaO+Ni(s)=Ba(g)+NiO(s)$	98	93	88	84
9. $BaO(s)+C(gr)=Ba(g)+CO$	91	78	65	53
10. $2BaO(s)+Si(s)=2Ba(g)+SiO_2(l)$	111	102	93	84
11. $3BaO(s)+Si(s)=2Ba(g)+BaSiO_3(s)$	87	77	69	60
12. $BaO+Mg(g)=Ba(g)+MgO(s)$	1	2	4	6

The results are thus to be compared with those of Reactions 6 to 9 and show magnesium to be thermodynamically the most effective of the reducing agents considered here.

Tungsten is also of considerable interest as a reducing agent for alkaline earth oxides, but is not treated here in view of the careful work of Moore, Allison, and Morrison.[12]

V. CONCLUSION

This is not intended to be an inclusive discussion of the application of thermodynamics to the chemistry of

TABLE III. Equilibrium constants of various chemical reactions.

1 Reaction	2 T	3 K	4 p_m(mm)
1. $2BaO(s)=2Ba(g)+O_2$	1073	1×10^{-33}	6×10^{-11}
	1273	2×10^{-41}	2×10^{-11}
	1473	2×10^{-32}	1×10^{-9}
2. $2SrO(s)=2Sr(g)+O_2$	1073	2×10^{-33}	5×10^{-11}
	1273	3×10^{-41}	3×10^{-11}
	1473	4×10^{-32}	2×10^{-9}
3. $2CaO(s)=2Ca(g)+O_2$	1073	8×10^{-35}	9×10^{-17}
	1273	1×10^{-46}	1×10^{-12}
	1473	8×10^{-37}	9×10^{-10}
4. $BaO(s)+H_2(g)=Ba(g)+H_2O(g)$	1073	2×10^{-17}	3×10^{-6}
	1273	7×10^{-14}	2×10^{-4}
	1473	3×10^{-11}	4×10^{-3}
5. $BaO(s)+CH_4(g)=Ba(g)+CO(g)+2H_2(g)$	1073	2×10^{-15}	6×10^{-3}[a]
	1273	4×10^{-10}	1×10^{-1}[a]
	1473	4×10^{-6}	1[a]
6. $BaO(s)+Ni(s)=Ba(g)+NiO(s)$	1073	1×10^{-19}	9×10^{-17}
	1273	7×10^{-16}	5×10^{-13}
	1473	4×10^{-13}	3×10^{-10}
7. $BaO(s)+C(\text{graph})=Ba(g)+CO(g)$	1073	1×10^{-16}	8×10^{-4}
	1273	6×10^{-13}	2×10^{-3}
	1473	1×10^{-9}	9×10^{-3}
8. $2BaO(s)+Si(s)=2Ba(g)+SiO_2(l)$	1073	2×10^{-31}	3×10^{-9}
	1273	1×10^{-26}	8×10^{-6}
	1473	3×10^{-23}	4×10^{-4}
9. $3BaO(s)+Si(s)=2Ba(g)+BaSiO_3(s)$	1073	2×10^{-28}	1×10^{-3}
	1273	2×10^{-23}	1×10^{-2}
	1473	1×10^{-9}	3×10^{-2}
10. $BaO(s)+Mg(g)=Ba(g)+MgO$	1073	3×10^{-1}	7[b]
	1273	2×10^{-1}	4×10^{0}[b]
	1473	1×10^{-1}	2×10^{0}[b]

[a] In equilibrium with CH_4 at 10^{-5} atmosphere.
[b] In equilibrium with magnesium gas at the vapor pressure of liquid magnesium.

[9] M. Schriel, Zeits. f. Anorg. allgem. Chemie **231**, 313 (1937).
[10] Hannay, MacNair, and White, J. App. Phys. **20**, 669 (1949); see also C. H. Prescott and J. Morrison, J. Am. Chem. Soc. **60**, 3047 (1938).
[11] A. Fineman and A. Eisenstein, J. App. Phys. **17**, 663 (1946); H. P. Rooksby, Nature **159**, 609 (1947).
[12] Moore, Allison, and Morrison, Phys. Rev. **75**, abstract in print; paper to be published; *cf.* also G. E. Moore, J. Chem. Phys. **9**, 427 (1941).

the oxide cathode, but rather to illustrate the type of problems that can be attacked profitably even without complete thermochemical data. However the data of Table II may be combined to obtain the free energies of a number of reactions not explicitly considered above. For example, Reaction 1 or Reaction 2 may be added to Reaction 4 to obtain the free energy for reduction of SrO by hydrogen or methane respectively; or Reactions 3, 5, and 9 may be combined to yield the free energy of reduction of CaO by graphitic carbon.

Finally, it is to be emphasized that equilibrium conditions are seldom attained; hence the barium pressures listed represent upper limits not likely to be experimentally realized.

The author is indebted to L. A. Wooten, C. Herring, and G. E. Moore for illuminating discussions of this subject.

Time Constants for Vacuum Gage Systems

S. A. Schaaf and R. R. Cyr
University of California, Berkeley, California
(Received January 20, 1949)

A typical system for measuring pressures in a rarefied gas consists of a vacuum gage connected to the gas by a length of tubing, usually with an orifice of diameter smaller than that of the tubing at the end. The interior surface of this system will outgas at a fairly constant rate for a long period of time so that an equilibrium state will be reached with a definite non-constant pressure distribution along the tubing. The response time constant for the system to come to equilibrium and the difference in pressure between gas and gage are functions of the outgassing rate and the geometry of the system. An analysis is made assuming molecular flow, and formulas are obtained for the response time and the pressure difference. It is shown that there is an optimum value of the tubing diameter for a given orifice diameter, gage volume, and length of tubing. This optimum is rather critical; if the diameter is too small, response time constants of the order of hours may result. Experimental work has been done and the results compared with theory. This work was done under ONR contract.

NOMENCLATURE

A = inside surface area of gage.
C = constant, $\frac{1}{4}[1/(2\pi RT)^{\frac{1}{2}}] \approx 10^{-5}$ sec./cm at 20°C.
L = length of tube.
p = pressure.
p_0 = pressure in system (applied at time $t=0$).
p_1 = initial pressure in gage.
p_2 = equilibrium pressure in gage.
Q = mass rate of flow.
q = surface outgassing rate.
$q' = RTq$.
R = gas constant.
r_0 = orifice radius.
r_t = tube radius.
r_{opt} = optimum tube radius.
t = time.
t_L = time constant (lag coefficient).
V = gage volume.
x = distance along tube from gage.
ρ = density.
$\varphi = r_t^3/r_0^3 L$.
$\theta = r_0^{4/3} L^{2/3}/V$.

INTRODUCTION

THE reading given by a vacuum gage connected to a vacuum system by a length of tubing (see Fig. 1) does not respond immediately to a change in the pressure level in the system. There is a certain time lag during which gas molecules flow in or out of the volume of the gage and tubing until an equilibrium condition is reached (see Fig. 2). The length of this time lag depends on the geometry of the gage and tubing system, and may be of the order of hours or more unless care is taken in choosing dimensions properly. There is, in fact, an optimum size of tubing diameter for any given installation; too large a diameter increases the time lag because a larger volume must be brought into equilibrium, too small a diameter increases the time lag by increasing the resistance to flow through the tubing. In the present paper it is shown that the gage pressure varies exponentially with time, and a formula is obtained for the time constant or lag coefficient of the gage—i.e., the time within which the gage will have registered $1/e$ of its complete change following an instantaneous pressure change in the vacuum system. This formula is derived under the assumption of "free molecular flow," i.e., that the pressure level is so low that all collisions between gas molecules may be neglected. The formula has been verified experimentally and shown to be adequate for design purposes.

The equilibrium state in general results in a pressure in the gage which is different from that in the system. This is apparently due to surface outgassing or ingassing, i.e., the emission or adsorption of gas molecules at the inside surface of gage and tubing. The rate of the outgassing or ingassing also changes with time, resulting in a gage pressure change, but does so very slowly, being almost constant for hours or more. It is desirable to have an estimate of the initial equilibrium pressure difference between gage and system. Such an estimate is obtained.

RESULTS

The time constant is found to be

$$t_L = C[VL/r_t^3 + 8V/3r_0^2 + 8\pi r_t^2 L/3r_0^2 + 4L^2/\pi r_t]. \quad (1)$$

In dimensionless form this reduces to

$$\frac{t_L r_0^2}{CV}=8/3+1/\varphi+\theta\left[\frac{8\pi}{3}\varphi^{2/3}+\frac{4}{\pi\varphi^{1/3}}\right], \qquad (2)$$

where $\theta=r_0^{4/3}L^{5/3}/V$ and $\varphi=r_t^3/r_0^2L$. Graphs of Eq. (2), which illustrate the rather critical optimum, are presented in Fig. 3. The four terms appearing on the right side of Eq. (1) may be interpreted as the time constants associated with, respectively: (i) the flow of gas in the gage volume V through the resistance L/r_t^3 of the tube, (ii) the flow of the same gas through the resistance $8/3r_0^2$ of the orifice, (iii) the flow of gas in the tube volume $\pi r_t^2 L$ through the resistance of the orifice, and (iv) the flow of gas in the tube through the distributed resistance $4L/\pi^2 r_t^3$ of the tube itself.

It is clear from (1) that t_L may be decreased by decreasing V and L and by increasing r_0. In general, however, there are physical limitations on how small V and L may be made, and on how large r_0 may be consistent with the purpose of the instrument. For any given r_0, L, and V there is an optimum r_t. In most actual applications the volume of the tube is small in comparison with that of the gage. The term $4L^2/\pi r_t$ in (1) may then be neglected and the optimum value of r_t is determined by

$$r_{opt}=[9r_0^2V/16\pi]^{1/5}=[0.18r_0^2V]^{1/5}. \qquad (3)$$

Experimental time constants have been obtained for three gage systems having the same values for r_0 and V, but with different values for r_t, respectively smaller than, equal to, and larger than the optimum indicated in Eq. (3). The results are given under I, II, and III in Table I.

The time constant for a gage system with no orifice other than the tube itself is found to be given by

$$t_L=C[VL/r_t^3+4L^2/\pi r_t]. \qquad (4)$$

Experimental values have been obtained for three such gage systems and are presented in Table I under IV, V, and VI. The theoretical and experimental pressure response as a function of time for the six gage systems is presented in Fig. 4 in dimensionless form, using the theoretical time constant appropriate to each gage system.

The pressure difference at the initial equilibrium between gage and system, due to outgassing flow, is found to be

$$p_{gage}-p_{system}=q'C\left\{\frac{8A}{3r_0^2}+\frac{AL}{r_t^3}+\frac{16r_t\pi L}{3r_0^2}+\frac{\pi L^2}{r_t^2}\right\}. \qquad (5)$$

The outgassing rate q' apparently depends upon the pressure and temperature history of the surface for several hours preceding a measurement, as well as upon the surface material. It may be positive (outgassing) or negative (ingassing), and approaches zero with time if the surface is exposed to a constant pressure gas for several hours (see Fig. 2). From the measured pressure differences and Eq. (5), we estimate that the maximum value of q' is of the order of 10^{-2} μcm/sec. for a Pyrex glass surface which has been exposed to pressures of the order of one micron for several hours. Further work on this phase of the problem is planned.

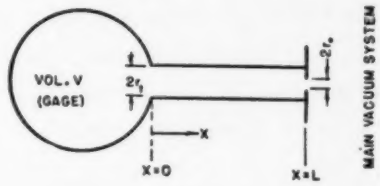

FIG. 1. Vacuum gage system schematic.

THEORETICAL DEVELOPMENT

Under free molecular flow conditions, the flow rate at any point in a tube depends on the pressure and temperature distribution along the entire tube. For steady isothermal flow in a long tube with a constant pressure gradient, the flow rate is proportional to the over-all pressure gradient.[1] The basic simplifying assumption of this paper is to set the instantaneous flow rate proportional to the instantaneous local pressure gradient only; the justification for this assumption is probably best found in the generally good agreement between theory and experiment indicated in Section 2.

Under the above assumption, we have the axial mass rate of flow given by[1]

$$Q=(-r_t^3/CRT)(\partial p/\partial x). \qquad (6)$$

The radial mass rate of flow in from the sides due to surface outgassing is, for a ring of width "dx,"

$$dQ=2\pi r_t q dx. \qquad (7)$$

Using the gas law $p=R\rho T$, and assuming T and q are constant, a mass balance on the element of length dx

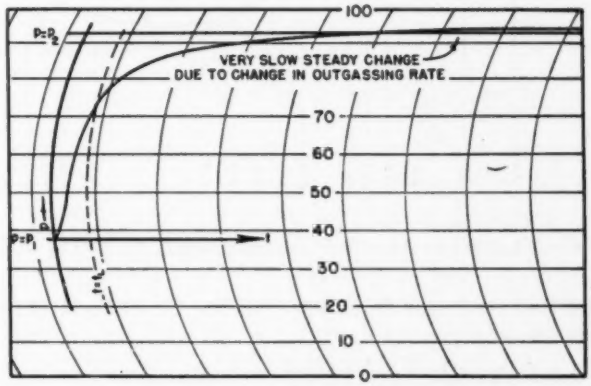

FIG. 2. Response of pressure gage.

gives the partial differential equation

$$\partial p/\partial t=(r_t/\pi C)(\partial^2 p/\partial x^2)+2q'/r_t. \qquad (8)$$

The boundary condition at $x=0$, is obtained by writing

[1] Leonard Benedict Loeb, *The Kinetic Theory of Gases* (McGraw-Hill Book Company, Inc., New York, 1934), p. 293.

a mass balance for the gage volume. It is

$$\partial p/\partial t=(r_t^3/VC)(\partial p/\partial x)+Aq'/V \text{ at } x=0. \quad (9)$$

For an infinitely thin orifice, the mass rate of flow is given by[2]

$$Q=(4\pi Cr_0^2/3)(p-p_0). \quad (10)$$

The boundary condition at $x=L$ is, hence,

$$\partial p/\partial t=(3r_0^2/8r_t^3)(p_0-p) \text{ at } x=L. \quad (11)$$

If the aperture consists in a short tube of length L' and radius r_0', an effective orifice r_0, given by

$$r_0=r_0'\Big/\left(1+\frac{3}{8}\frac{L'}{r_0'}\right)^{\frac{1}{2}}, \quad (12)$$

should be used in Eq. (11). The case of no orifice other than the tube itself, i.e., $p=p_0$ at $x=L$, may be obtained formally by letting $r_0\to\infty$ in Eq. (11).

The differential Eq. (8) is equivalent to a heat conduction equation with a distributed heat source,[3] and

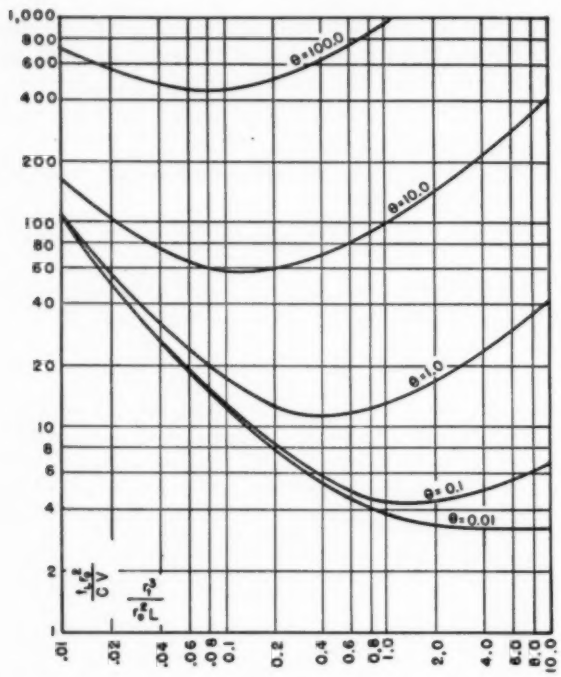

FIG. 3. Variation of time constants with geometry of gage system. $C=3/4(2\pi RT)^{\frac{1}{2}}=2.61\times10^{-8}$ sec./in. at 530°R. $\theta=r_0^{4/3}L^{5/3}/V$.

together with the boundary conditions (9) and (11), has the solution

$$p=p_0+q'C[8A/3r_0^2+AL/r_t^3 +16r_t\pi L/3r_0^2+\pi L^2/r_t^2] -ACq'x/r_t^3-\pi Cq'x^2/r_t^2 +\sum_1^\infty (A_n\cos\lambda_n x+B_n\sin\lambda_n x)\exp\left(-\frac{\lambda_n^2 r_t}{\pi C}t\right), \quad (13)$$

where the eigenvalues λ_n are determined from the equation,

$$\tan\lambda_n L=\frac{3\pi r_t^2 r_0^2-8r_t^3V\lambda_n^2}{(3Vr_0^2+8\pi r_t^5)\lambda_n}. \quad (14)$$

From Eq. (13), we have at $x=0$,

$$\frac{p-p_1}{p_2-p_1}\approx\exp\left(-\frac{\lambda_1^2 r_t}{\pi C}t\right), \quad (15)$$

where λ_1 is the smallest eigenvalue. By definition, the time constant t_L is given by

$$t_L=\pi C/\lambda_1^2 r_t. \quad (16)$$

Solving Eq. (14) approximately for λ_1, we obtain finally, Eq. (1):

$$t_L\approx C[VL/r_t^3+8V/3r_0^3+8\pi r_t^2L/3r_0^2+4L^2/\pi r_t].$$

Eq. (4) is obtained by letting $r_0\to\infty$ in Eq. (1). Eq. (5) is obtained directly from Eq. (13) by setting $x=0$ and letting $t\to\infty$.

EXPERIMENTAL SET-UP

The equipment used for making the experimental tests of time constants consisted of the small vacuum system in Fig. 5 which is ordinarily used for gage calibration. This system has a volume of approximately 10 liters and a pumping speed of 25 liters per sec., yielding a time constant of 0.4 sec.—considerably faster than any of the gage systems tested.

The gage systems (dimensions listed in Table I) were

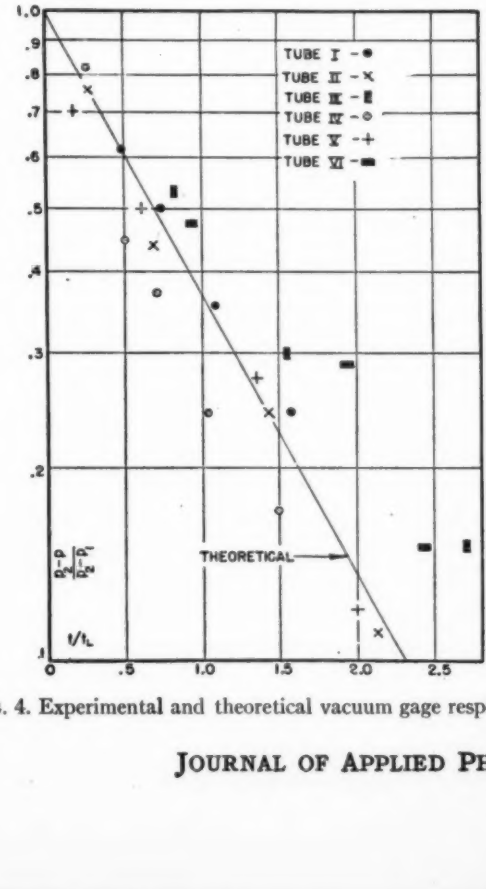

FIG. 4. Experimental and theoretical vacuum gage responses.

[2] See reference 1, p. 302.
[3] See, for example, H. S. Carslaw and J. C. Jaeger, *Conduction of Heat in Solids* (Oxford University Press, London, 1947).

TABLE I. Theoretical and experimental time constants for six gage systems.

	Tube I	Tube II	Tube III	Tube IV	Tube V	Tube VI
V (cm³)	164	164	164	52.5	52.5	52.5
L (cm)	25.4	25.4	25.4	25.4	25.4	153
r_1 (cm)	0.11	0.41	1.6	0.13	0.05	0.41
r_0 (cm)	0.02	0.02	0.02	—	—	—
Time constant theory (sec.)	41	14	24	6.7	91	2.1
Time constant exp. (sec.)	51	13	32	5.0	100	2.6

constructed of Pyrex glass using standard commercially available ionization gages. Ionization gages were selected, since their pressure response is instantaneous in comparison with the Pirani and thermocouple gages which have a slow response due to the necessity of obtaining thermal equilibrium in the gage. The two ionization gages were driven by circuits which regulated the voltage on the grids and the emission current.[4] The ion currents were measured by a balanced vacuum tube voltmeter bridge circuit in which an Esterline Angus recording meter was used to measure the output.

The measurements were made by pumping on the gage system until equilibrium had been reached, then a needle valve connected to the main vacuum system was opened, causing a sharp rise in the pressure. The variation of pressure in the glass gage system was measured on the recorder as indicated in Fig. 2, and the data used in Figs. 3 and 4 were reduced from the recorder tape.

FIG. 5. Experimental equipment.

This work was done under a contract between the University of California and the ONR.

[4] L. N. Ridenour and C. W. Lampson, Rev. Sci. Inst. 8, 162 (1937).

A Generalization of Nyquist's Stability Criteria

A. VAZSONYI
Underwater Ordnance Department, Naval Ordnance Test Station, Pasadena, California
(Received January 24, 1949)

A generalization of Nyquist diagrams is developed. These new diagrams yield a lower limit to the values of "damping ratios" and so permit the evaluation of the stability and the "degree" of stability of systems characterized by ordinary linear differential equations.

I. INTRODUCTION

THE classical method to investigate ordinary linear differential equations consists of determining the roots of the characteristic equation and computing the response to some special input functions, such as a step or a pulse. Often one is interested only in the nature of the possible oscillations of the system. In this latter case from the roots of characteristic equation, the so-called "damping ratios" are computed. These dimensionless quantities can be considered as a measure of the oscillatory nature of the system.

The classical procedure is very laborious for complicated systems. The frequency method developed by Nyquist* permits the stability investigation of very complicated linear systems without an excessive amount of labor. From the Nyquist diagram of the system, it can be readily determined whether the system is stable or not. Furthermore, by special experience a certain insight about the "degree" of stability of the system can also be obtained. However, the classical "degree" of stability is not immediately correlated with the "degree" of stability of the system obtained from a Nyquist diagram.

The purpose of this paper is to present a generalization of Nyquist's theorem. It will be seen that the theorem in this more general form permits a quantitative correlation between the classical and the frequency (steady-state) method. More specifically, the generalized Nyquist diagram yields a lower limit to the damping ratios of the linear system.

* H. Nyquist, Bell Sys. Tech. J. 11, 126 (1932).

II. NYQUIST'S CRITERIA AS A MAPPING THEOREM

Consider the general form of a homogeneous n'th-order linear differential equation with constant coefficients

$$A_n\frac{d^n\theta}{dt^n}+A_{n-1}\frac{d^{n-1}\theta}{dt^{n-1}}+\cdots+A_2\frac{d^2\theta}{dt^2}+A_1\frac{d\theta}{dt}+A_0\theta=0. \quad (1)$$

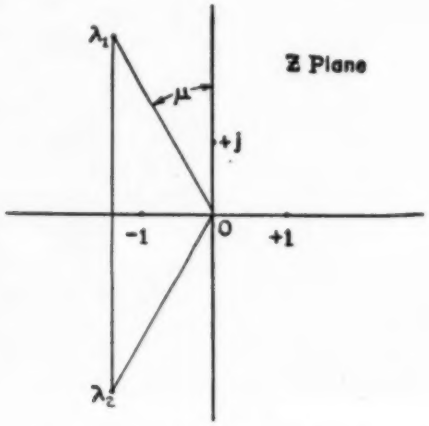

FIG. 1. λ_1 and λ_2 in complex plane.

The auxiliary algebraic equation associated with this equation is

$$A_n\lambda^n+A_{n-1}\lambda^{n-1}+\cdots+A_2\lambda^2+A_1\lambda+A_0=0. \quad (2)$$

Let the roots of Eq. (2) be $\lambda_1, \lambda_2, \cdots, \lambda_n$. The general solution of the differential equation is

$$\theta=c_1e^{\lambda_1 t}+c_2e^{\lambda_2 t}+\cdots+c_ne^{\lambda_n t}. \quad (3)$$

The differential equation is stable when each term of the general solution goes to zero with increasing time. Thus we have

Lemma 1. The differential Eq. (1) is stable when all the roots of Eq. (2) have negative real parts.

Let us consider now the complex function

$$w=f(z)=A_nz^n+A_{n-1}z^{n-1}+\cdots+A_1z+A_0. \quad (4)$$

This function maps the z plane into the w plane. In particular, assume that the positive half of the z plane (where the real part of z is non-negative) is mapped into the "interior" of the domain D of the w plane. According to our Lemma, Eq. (1) is stable when the domain D does not contain the origin of the w plane. The contour of the domain D is given by the mapping of the imaginary axis of the z plane and so is given by

$$f(j\omega)=A_n(j\omega)^n+A_{n-1}(j\omega)^{n-1}+\cdots+A_1(j\omega)+A_0, \quad (5)$$

where ω is a real number varying from $-\infty$ to $+\infty$. Thus the stability of Eq. (1) can be determined in three steps:

1. Plot the $f(j\omega)$ function in the w plane.
2. Determine the "inside" of the domain limited by $f(j\omega)$ (that is, determine on which side the positive half of the z plane is mapped).
3. If the domain contains the origin, the differential equation is unstable. If it does not contain the origin, the equation is stable.

III. MEASURE OF STABILITY

Consider the second-order differential equation

$$A_2\frac{d^2\theta}{dt^2}+A_1\frac{d\theta}{dt}+A_0\theta=0. \quad (6)$$

This equation can be written in the form

$$(d^2\theta/dt)+2\zeta\omega(d\theta/dt)+\omega^2=0, \quad (7)$$

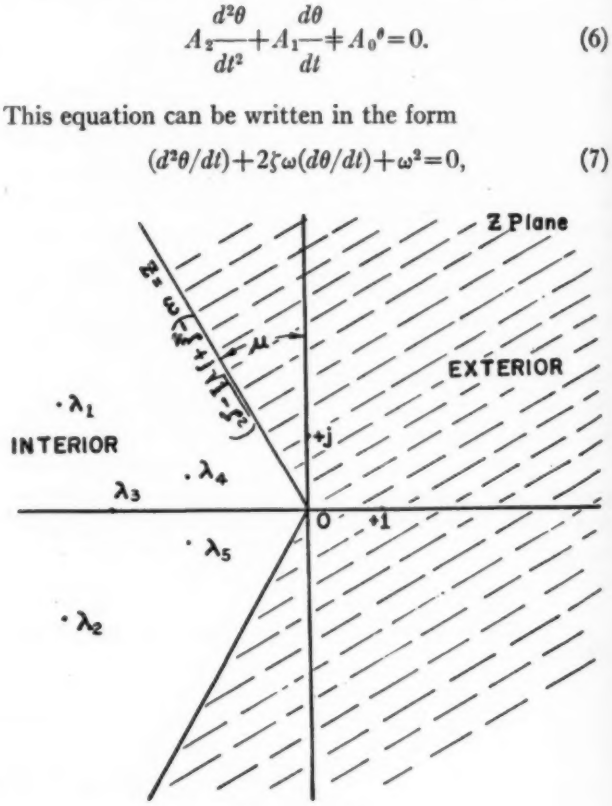

FIG. 2. z plane.

where

$$\omega=(A_0/A_2)^{\frac{1}{2}} \quad (8)$$

and

$$\zeta=A_1/2(A_0A_2)^{\frac{1}{2}}. \quad (9)$$

ω is the undamped natural frequency and ζ is the dimensionless damping ratio. The quantity ζ is a measure of the stability of the system. When $\zeta<0$ the system is unstable, when $\zeta=0$ the system is neutrally stable, when $0<\zeta<1$ the system oscillates with decreasing amplitude, when $\zeta\geqslant 1$ the system is not capable of oscillations. Suppose now, that the system is oscillatory and let λ_1 and λ_2 be the conjugate complex roots of the auxiliary equation of Eq. (6). By solving Eq. (7)

$$\lambda_1=[-\zeta+j(1-\zeta^2)^{\frac{1}{2}}]\omega \quad (10a)$$

$$\lambda_2=[-\zeta-j(1-\zeta^2)^{\frac{1}{2}}]\omega. \quad (10b)$$

Figure 1 shows a diagram of λ_1 and λ_2 in the complex plane. Let us call the angle between the vector λ_1 and the imaginary axis the "excess" angle μ. Thus,

$$\mu=\text{Arg}\lambda-\pi/2. \quad (11)$$

From Eqs. (10a) and (10b) follows, that

$$\sin\mu=\zeta. \tag{12}$$

Thus, the excess angle is a measure of the stability of the system. When $\mu=0$ the system is neutrally stable, when $\mu=\pi/2$ the system is critically damped.[1]

Consider now the n'th-order equation (1). The roots of the auxiliary equation are real or conjugate complex. Each pair of conjugate complex roots corresponds to a second-order equation of the type of Eq. (6). Each pair of roots defines a damping ratio and an excess angle. Lemma 1 can now be generalized.

Lemma 2. Assume that the roots of Eq. (2) in the upper half plane lie in the sector to the left of the excess angle μ (Fig. 2). The damping ratios associated with Eq. (1) are larger than $\zeta=\sin\mu$.

IV. GENERALIZATION OF NYQUIST'S CRITERIA

Equation (4) maps the z plane into the w plane. Assume that the exterior of the sector of Lemma 2 in the z plane (see Fig. 2) is mapped into the domain D of the w plane. According to Lemma 2, if D does not contain the origin, the damping ratios of Eq. (1) are larger than $\sin\mu$. Now, the upper half of the sector in the z plane can be defined by

$$z=\omega(-\sin\mu+j\cos\mu)=\omega[-\zeta+j(1-\zeta^2)^{\frac{1}{2}}], \tag{13}$$

where ω is a real number varying from 0 to $+\infty$. The half of the contour of domain D in the w plane is given by

$$f\{\omega[-\zeta+j(1-\zeta^2)^{\frac{1}{2}}]\}=A_n\{\omega[-\zeta+j(1-\zeta^2)^{\frac{1}{2}}]^n\} +A_{n-1}\{\omega[-\zeta+j(1-\zeta^2)^{\frac{1}{2}}]\}^{n-1}+\cdots+A_0. \tag{14}$$

Thus the following criteria can be set up:

1. Plot the $f\{\omega[-\zeta+j(1-\zeta^2)^{\frac{1}{2}}]\}$ function for a given ζ in the w plane.
2. Determine the "inside" of the domain limited by $\omega[-\zeta+j(1-\zeta^2)^{\frac{1}{2}}]$.
3. If this domain does not contain the origin, the damping ratios of the system are all larger than the given ζ.

V. NUMERICAL EXAMPLE

Consider the torque amplifier

$$I(d^2\theta_0/dt^2)+\beta(d\theta_0/dt)=M, \tag{15}$$

where I is the moment of inertia, β is the viscous damping, θ_0 is the output, and M is the torque of the motor.

Assume that the torque M is related to the error through the differential equation

$$T(dM/dt)+M=K\epsilon=K(\theta_i-\theta_0), \tag{16}$$

where θ_i is the input angle. Equation (16) expresses the fact that for a given error, ϵ, the torque is developed through the time lag T. Write Eqs. (15) and (16) in operational notation

$$p(Ip+\beta)\theta_0=M \tag{17}$$

$$(Tp+1)M=K(\theta_i-\theta_0). \tag{18}$$

By eliminating M,

$$\left(Ip^2+\beta p+\frac{K}{Tp+1}\right)\theta_0=\frac{K\theta_i}{Tp+1}. \tag{19}$$

We are interested in the homogenous equation only. This can be written as

$$\left[1+\frac{K/\beta}{p(I/\beta p+1)(Tp+1)}\right]\theta_0=0. \tag{20}$$

The performance of the system can be studied with the

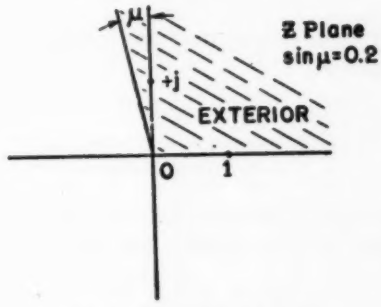

FIG. 3a. Mapping of z plane.

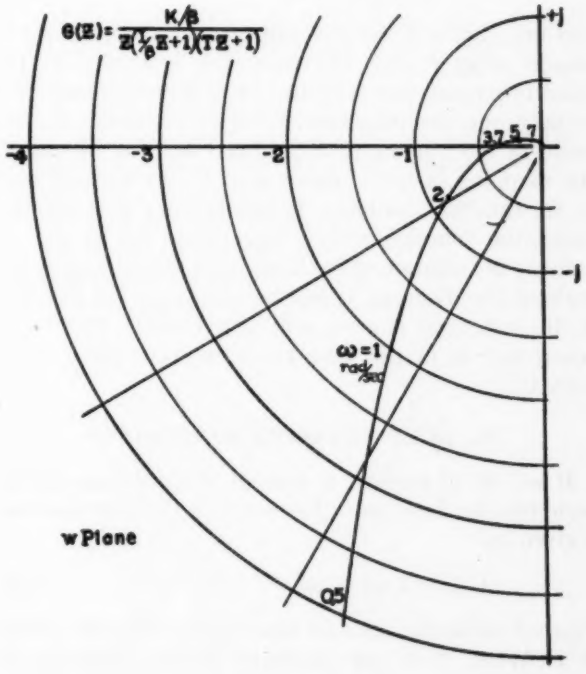

FIG. 3b. w plane.

[1] Equation (12) was communicated to the author by Frank J. Bednarz.

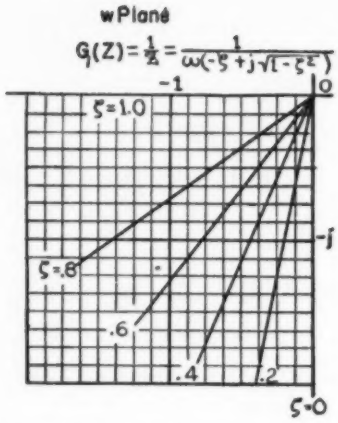

FIG. 4. The transfer function $G_1(z)=1/z$.

aid of the function

$$f(z)=1+\frac{K/\beta}{z(I/\beta z+1)(Tz+1)}. \tag{21}$$

Actually, it is more practical and useful to study the transfer function

$$G(z)=\frac{K/\beta}{z(I/\beta z+1)(Tz+1)}. \tag{22}$$

In this case the "−1" point of $G(z)$ takes the place of the zero point of $f(z)$. Assume the following numerical values:

$I=2.00$ slug-ft.^{2}
$\beta=5.50$ ft. lb./rad./sec.
$T=0.08$ sec.,

and investigate K for the value giving damping ratios smaller than $\zeta=0.2$. (Actually the system is of the third order and has only one second-order factor and so only one damping ratio.) Figure 3a shows the exterior of the z plane to be mapped and Fig. 3b shows the mapping in the w plane. For K, the value $K=10$ ft. lb./rad. was assumed. It can be seen that for this value, the damping ratio is larger than 0.2 as the -1 point is not contained in the domain. By changing the scale of the diagram, it can be shown that if $K=30.2$ ft. lb./rad., the domain will just contain the "−1" point, and so in this case the damping ratio ζ is exactly 0.2.

VI. BASIC TRANSFER FUNCTIONS

It will be of interest to present plots of some of the basic transfer functions. The simplest transfer function is given by

$$G_1(z)=1/z=1/\omega[-\zeta+j(1-\zeta^2)^{\frac{1}{2}}]. \tag{23}$$

Figure 4 shows the transfer function for different values of ζ. When $\zeta=0$ the standard transfer function is obtained.

Another important transfer function is given by

$$G_2(z)=1+Tz=1+T\omega[-\zeta+j(1-\zeta^2)^{\frac{1}{2}}]. \tag{24}$$

This is a "phase lead" transfer function. Figure 5 shows the plots for this function.

A third important transfer function is given by

$$G_3(z)=1/1+Tz=1/1+T\omega[-\zeta+j(1-\zeta^2)^{\frac{1}{2}}]. \tag{25}$$

This "phase lag" or "time lag" function is shown on Fig. 6. The transfer function loci are circular arcs through the "0" and "1" points.

These three transfer functions provide the building blocks for transfer functions of more complicated systems. It can be seen that the usual theory of transfer functions can be easily generalized from the transfer functions introduced in this paper.

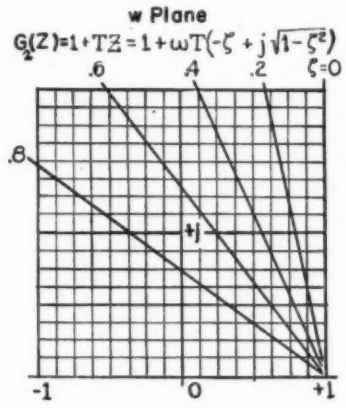

FIG. 5. The transfer function $G_2(z)=1+Tz$.

VII. GENERALIZED ATTENUATION PHASE ANALYSIS

More recent methods[2] of servo-analysis plot the logarithm of the transfer function

$$\ln G=\ln|G|+j\,\mathrm{Arg}G=A+j\varphi. \tag{26}$$

Separate diagrams for the attenuation and for the

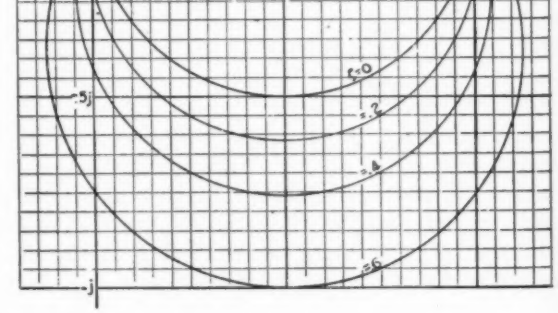

FIG. 6. The transfer function

$$G_3(z)=\frac{1}{(1+Tz)}=\frac{1}{1+T\omega[-\zeta+j(1-\zeta^2)^{\frac{1}{2}}]}$$

[2] See: James, Nichols, and Phillips, *Theory of Servomechanism* (McGraw-Hill Book Company, Inc., New York, 1947), p. 163.

argument are prepared, both plotted on semilog paper. The basic plot in this method is given by

$$A=\ln|1+T\omega[-\zeta+j(1-\zeta^2)^{\frac{1}{2}}]|. \tag{27}$$

Figure 7 shows the attenuation curve of Eq. (27) for different values of ζ. It is important to note that the asymptotic characteristic of the attenuation diagram is independent of ζ. Figure 8 shows the corresponding phase diagram. Obviously,

$$\tan\varphi=\frac{T\omega(1-\zeta^2)^{\frac{1}{2}}}{1-\zeta T\omega}. \tag{28}$$

The asymptotic characteristics of the phase diagram are of great importance. Obviously when $T\omega=0$, $\varphi=0$; when $T\omega=\infty$, $\cos\varphi=-\zeta$. Thus the value of φ for large $T\omega$ is affected by ζ while the asymptotic character of the attenuation is independent of ζ.

A Comment on Dr. Vazsonyi's Paper, "A Generalization of Nyquist's Stability Criteria"

S. J. Mason
Research Laboratory of Electronics, Massachusetts Institute of Technology, Cambridge, Massachusetts
(May 20, 1949)

THE Nyquist diagram of a function $F(S)$, where $S=r\exp j\theta$, may be defined as the F plane map of the S plane curve $|\theta|=\pi/2$. Dr. Vazsonyi presents and discusses a generalization in which some fixed value of $|\theta|$ between $\pi/2$ and π is mapped. Such maps represent loci of constant Q.[1] If the appropriate critical point is not encircled by the F-plane locus, then the system not only is stable but the associated transient oscillation must exhibit a Q less than $\cot(2\theta-\pi)$. Gain-phase-log frequency techniques, generalized to constant-Q loci by Dr. Vazsonyi, provide an approach to system design for a specified maximum allowable Q.

In working with Nyquist Diagrams and gain-phase diagrams the writer has used a method of Q determination which may be of supplementary interest to readers of Dr. Vazsonyi's paper. The method requires only the standard Nyquist plot of $F(j\omega)$ and makes use of a graphical process of analytic continuation to locate the critical frequency in the left half of the S plane. The steps are as follows. The Nyquist diagram, $F(j\omega)$ or $\log F(j\omega)$, is plotted. A uniform frequency scale is marked upon the curve in the region of closest approach to the critical point. A grid-work of curvilinear squares is then sketched in the neighborhood of the critical point, using the frequency marks on the Nyquist plot as starting points for the construction. The grid-work represents the F plane map of rectangular coordinates in the S plane.

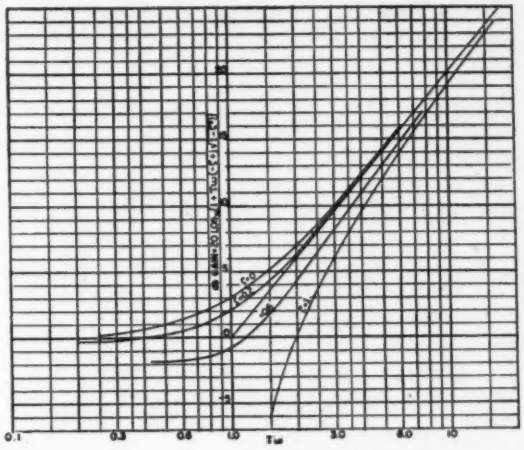

FIG. 7. Attenuation diagram for $\ln|1+Tz|$.

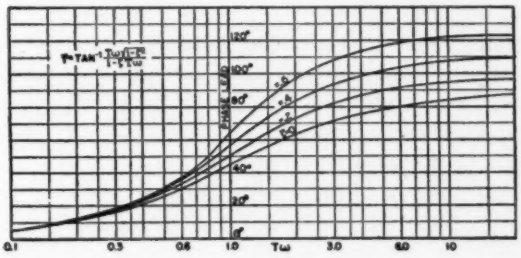

FIG. 8. Phase diagram for $\ln|1+Tz|$.

The critical frequency $S_1=\sigma_1+j\omega_1$, corresponding to the critical point, may then be read from the curvilinear coordinates of the sketch and Q_1 may be computed.

If a logarithmic (rather than an arithmetic) frequency scale is marked upon the Nyquist plot, then the associated curvilinear squares represent the F plane map of the coordinates $\log|S|$ and θ. A critical point which lies at θ_1 in this grid-work indicates the value of $Q_1=\cot(2\theta_1-\pi)$.

The graphical method described here is particularly simple in problems where the Q of the critical frequency is high, since the required curvilinear squares will then exhibit little distortion. Conversely, if the critical frequency lies far from the $j\omega$ axis in the S plane and close to singularities of the function $F(S)$, then elaborate sketching will be necessary in order to continue the function from the $F(j\omega)$ plot to the critical point.

[1] The Q of a complex-frequency $S_1=\sigma_1+j\omega_1$ is defined here as

$$Q_1=\frac{-|\omega_1|}{2\sigma_1}$$

and the associated transient is of the form

$$f(t)=\exp\left(\frac{-|\omega_1|t}{2Q_1}\right)\cos\omega_1 t.$$

The Propagation of Electromagnetic Waves in a Tube Containing a Coaxial D.C. Discharge*, **

PHILIP ROSEN***
Sloane Physics Laboratory, Yale University, New Haven, Connecticut
(Received January 25, 1949)

The boundary value problem involved in finding the propagation characteristics of electromagnetic waves in a cylindrical tube containing a coaxial d.c. discharge is solved. Ohm's law is assumed to hold for the alternating current. This assumption has been verified theoretically for the case where the alternating electric field is small compared with the d.c. field. Curves which give the relationship between the complex propagation constant, γ, and the complex dielectric coefficient, K_c', have been computed for the solution in which the TEM mode of the coaxial line is approached as K_c' becomes infinite.

INTRODUCTION

RECENTLY microwave techniques have been applied to the study of d.c. gaseous discharges by D. E. Kerr[1,2,3] of the M.I.T. Research Laboratory of Electronics. He used a cylindrical conducting tube which contained a d.c. coaxial mercury vapor discharge. He measured the propagation characteristics of microwaves as a function of d.c. discharge current by standing wave measurements. The details of this experiment will be given in C.

The purpose of the present work is to solve the boundary value problem involved in this experiment, to find a relation between the dielectric properties of the discharge and the propagation of electromagnetic waves through the coaxial line.

In the past, the propagation of the electromagnetic waves in a cylindrical tube containing two non-lossy coaxial dielectric materials has been investigated by Buchholz,[4] Pincherle,[5] Frankel,[6] and by Bruck and Wicker.[7] These investigators only considered dielectric coefficients equal to or greater than unity. In the present work we deal with a lossy dielectric and furthermore the dielectric coefficient is permitted to be less than unity and even negative. A dielectric coefficient less than one is characteristic of media which contain a large density of electrons (see Appendix).

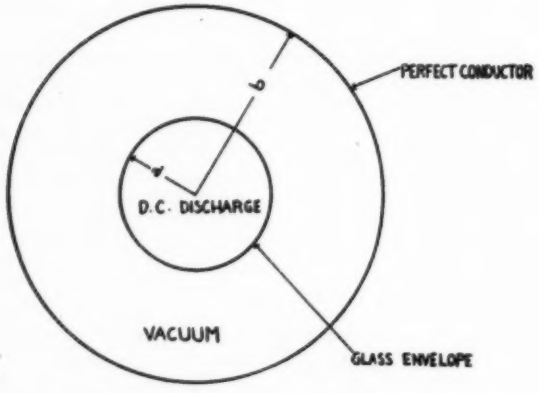

FIG. 1. Wave guide with lossy center conductor.

A. BOUNDARY PROBLEM

Our basic task is to solve the boundary problem of the wave guide shown in Fig. 1. For simplicity we have taken the outer conductor to be perfect. We also assume that the glass container for the ionized gas has a negligible effect. But before we can proceed we must consider a general set of Maxwell's equations applicable to a medium containing charges and currents. Also, for simplicity we will assume our center conductor to be homogeneous and isotropic. If we assume Ohm's law to hold, i.e.,

$$\mathbf{J}=\sigma_c\mathbf{E}, \tag{1}$$

where σ_c may be complex, $\sigma_c=\sigma_R+i\sigma_I$, and also assume a time variation of the form $e^{i\omega t}$, we can then use a set of Maxwell's equations which contain no charges or currents but which is equivalent to that for a medium having a complex dielectric constant, K_c.[8] It can be shown that: $K_c=K-i(\sigma_R/\omega)$, where K the effective dielectric constant, $=\epsilon+(\sigma_I/\omega)$, where ϵ is the ordinary dielectric constant.

Thus our problem reduces to that of a cylindrical wave guide with two dielectrics, which has been solved by Pincherle[5] for real positive dielectric constants. For a circularly symmetric transverse magnetic wave we obtain:

$$\frac{K_c'}{\zeta_i}\frac{J_1(\zeta_i)}{J_0(\zeta_i)}=\frac{1}{\zeta_0}\frac{\{J_1(\zeta_0)/J_0[(b/a)\zeta_0]\}-\{N_1(\zeta_0)/N_0[(b/a)\zeta_0]\}}{\{J_0(\zeta_0)/J_0[(b/a)\zeta_0]\}-\{N_0(\zeta_0)/N_0[(b/a)\zeta_0]\}}, \tag{2}$$

* This paper is part of a dissertation presented for the degree of Doctor of Philosophy in Yale University.

** This research has been assisted by the ONR under contract N7onr-288, Task Order II.

*** Now at Rensselaer Polytechnic Institute, Troy, New York.

[1] Kerr, Brown, and Kern, Phys. Rev. **71**, 480 (1947).

[2] D. E. Kerr, Gas Discharge Seminar, M.I.T., Cambridge, Massachusetts, October 7, 1946.

[3] D. E. Kerr and W. P. Allis, M.I.T., Cambridge, Massachusetts. Private communication.

[4] H. Buchholz, Ann. d. Physik **43**, 5, 313–368 (1943).

[5] L. Pincherle, Phys. Rev. **66**, 118–130 (1944).

[6] S. Frankel, J. App. Phys. **18**, 650–655 (1947).

[7] G. G. Bruck and E. R. Wicker, J. App. Phys. **18**, 766–769 (1947).

[8] Leigh Page, *Electrodynamics* (D. Van Nostrand Company, Inc., New York, 1940), Chapter 6.

where:

$$\zeta_i^2-\zeta_0^2=(K_c'-1)\left(\frac{2\pi}{\lambda_0/a}\right)^2 \tag{3}$$

and

$$\zeta_0=a[\gamma^2+(2\pi/\lambda_0)^2]^{\frac{1}{2}}, \quad \zeta_i=a[\gamma^2+K_c'(2\pi/\lambda_0)^2]^{\frac{1}{2}}.$$

Here $\gamma=\alpha+i\beta$, is the complex propagation constant with α, the attenuation, and β, the phase constant; $K_c'=K_i/K_0-i(\sigma/\omega K_0)=K_i'-i(\sigma/\omega K_0)$ (K_0 is the dielectric constant of vacuum); λ_0 is the free space wavelength; b, and a, are the outside and inside radii respectively; i refers to the inside or central region and 0 refers to the outside region or vacuum.

In our work we will only consider a circularly symmetric TM wave. This is necessary for simplicity since for the non-symmetric case a linear combination of TM and TE waves must be used. From Eqs. (2) and (3), it can be seen that our problem is determined by a choice of the ratios λ_0/a, and b/a.

B. APPROXIMATIONS AND NUMERICAL SOLUTION

Our problem is to solve Eq. (2) subject to Eq. (3)—an attempt to do this analytically is unsuccessful. Therefore, we are left with the methods of approximation and of numerical solution. Both methods will be used so that one can be employed to check the other.

Approximations

If the complex dielectric coefficient, K_c', becomes very large, one would expect to obtain the solutions for a coaxial line. It can be shown[9] that for a coaxial line:

$$\gamma=[n\pi/(b-a)-\omega^2/c^2]^{\frac{1}{2}}, \quad n=0, 1, 2\cdots,$$

or in terms of ζ_0:

$$\zeta_0=n\pi/(b/a-1). \tag{4}$$

The TEM mode ($n=0$) therefore means that $\zeta_0=0$. Because of this result, it seems wise to try the approximations to the Bessel functions for large ζ_i and for large ζ_0 first, leaving the approximations for large ζ_i and small ζ_0 for later.

Large ζ_i, Large ζ_0.—Using the asymptotic expressions for the Bessel functions of the first and second kind[10] in Eq. (2), and assuming that the imaginary part of ζ_i is large we obtain:

$$\frac{-(K_c')^2}{\zeta_i^2}=\frac{1}{\zeta_0^2}\left[\frac{1}{\sin^2\{[(b/a)-1]\zeta_0\}}-1\right]. \tag{5}$$

The imaginary part of ζ_i would certainly be large for high σ and high negative K_i' since:

$$\zeta_i=a\{\gamma^2+[K_i'-(i\sigma/\omega K_0)](2\pi/\lambda_0)^2\}^{\frac{1}{2}}.$$

Thus a high negative effective dielectric constant has the same effect as a high conductivity. Now as $|K_i'|\to\infty$, $[(b/a)-1]\zeta_0=n\pi$, $n=0, 1, 2\cdots$. However, $\zeta_0=0$ does not satisfy our initial requirement for ζ_0 to be large. To make ζ_0 as large as possible for the other solutions, b/a should be close to unity.

Large ζ_i, Small ζ_0.—For small values of the arguments of the Bessel functions we have:[10]

$$\begin{aligned} &\text{(a)}\ J_0(z)\approx 1 && \text{(b)}\ J_1(z)\approx\frac{z}{2} \\ &\text{(c)}\ N_0(z)\approx\frac{-2}{\pi}\ln\left(\frac{2}{1.78z}\right) && \text{(d)}\ N_1(z)\approx\frac{-2}{\pi z}. \end{aligned} \tag{6}$$

Using these for ζ_0, and the asymptotic expressions for ζ_i, in Eq. (2) we obtain:

$$\zeta_0=i^{\frac{1}{2}}(2\pi a/\lambda_0)^{\frac{1}{2}}[\ln b/a]^{-\frac{1}{2}}(K_c')^{-\frac{1}{2}}, \tag{7}$$

provided that $\zeta_0^2\ll 1$ and $|K_c'|\gg 1$. We see from Eq. (7) that $\zeta_0\to 0$ (TEM mode) as $|K_c'|\to\infty$. The usefulness of Eq. (7) lies in guiding our numerical work. It is not accurate enough in itself to be used for calculation except if one is satisfied with error of 5 percent or more.

The following important conclusions can be drawn from Eq. (7). First if K_c' is real and highly negative, ζ_0 lies along the positive imaginary axis near the origin and moves downward as K_i' decreases. Secondly if K_c' is a highly negative imaginary, ($|\sigma/\omega K_0 K_i'|\gg 1$), the argument of ζ_0 is 67.5°.

Dielectric Rod Type of Propagation

From Eq. (7) it follows that for real and highly negative K_c', ζ_0 lies along the positive imaginary axis near the origin and approaches the origin as K_i' decreases further. This suggests that for low negative and real K_c', ζ_0 may be a positive imaginary but large in absolute value. To verify this guess, we will take ζ_0 to be a large positive imaginary. Then from (3) ζ_i is also a large positive imaginary.

Now, the Bessel functions, J_n and N_n, can be expressed in terms of the Hankel functions.[11] If we make use of this on the right of Eq. (2) we obtain:

$$\frac{K_c'}{\zeta_i}\frac{J_1(\zeta_i)}{J_0(\zeta_i)}=\frac{1}{\zeta_0}\frac{\{H_1^{(1)}(\zeta_0)/H_0^{(1)}[(b/a)\zeta_0]\}-\{H_1^{(2)}(\zeta_0)/H_0^{(2)}[(b/a)\zeta_0]\}}{\{H_0^{(1)}(\zeta_0)/H_0^{(1)}[(b/a)\zeta_0]\}-\{H_0^{(2)}(\zeta_0)/H_0^{(2)}[(b/a)\zeta_0]\}}. \tag{8}$$

From the asymptotic expressions for the Hankel functions, it can be seen that the ratios involving the $H_n^{(2)}$ functions become much smaller than the ratios involv-

[9] Sarbacher and Edson, *Hyper and Ultra High Frequency Eng.* (John Wiley & Sons, Inc., New York, 1943), Chapter 7.

[10] Stratton, *Electromagnetic Theory* (McGraw-Hill Book Company, Inc., New York, 1941), p. 357ff.

[11] Jahnke and Emde, *Tables of Functions* (Dover Publications, New York, 1943), p. 134.

ing the $H_n^{(1)}$ function as ζ_0 becomes a large imaginary. We therefore have:

$$\frac{K_c'}{\zeta_i}\frac{J_1(\zeta_i)}{J_0(\zeta_i)}=\frac{1}{\zeta_0}\frac{H_1^{(1)}(\zeta_0)}{H_0^{(1)}(\zeta_0)}. \tag{9}$$

Equation (9) is identical with the equation obtained by Hondros and Debye[12] for dielectric guides. This means that for large positive imaginary ζ_0, the fields attenuate rapidly as one goes radially outward from the center into the vacuum, i.e., most of the energy is confined in the central dielectric rod. This is just the reverse of the case where $\zeta_0=0$ (TEM mode) where the energy is confined to the annular space. For large ζ_0 and large ζ_i Eq. (9) can be put into the form:

$$\zeta_0^2=\frac{(2\pi a/\lambda_0)^2}{K_c'+1}. \tag{10}$$

This relation could have been obtained from Eq. (5), since:

$$\sin\left\{\left[\left(\frac{b}{a}\right)-1\right]\zeta_0\right\}\to\infty, \quad \text{as} \quad \zeta_0\to i\infty.$$

From Eq. (10) we conclude that $\zeta_0=i\infty$ for $K_c'=-1$ and as K_i' becomes more negative, ζ_0 travels down the positive imaginary axis toward the origin. For a small enough imaginary part of K_c' (ζ_0 nearly a positive imaginary), ζ_0 does not become infinite at $K_c'=-1$, and we have a resonance effect with the function rising steeper the smaller the loss.

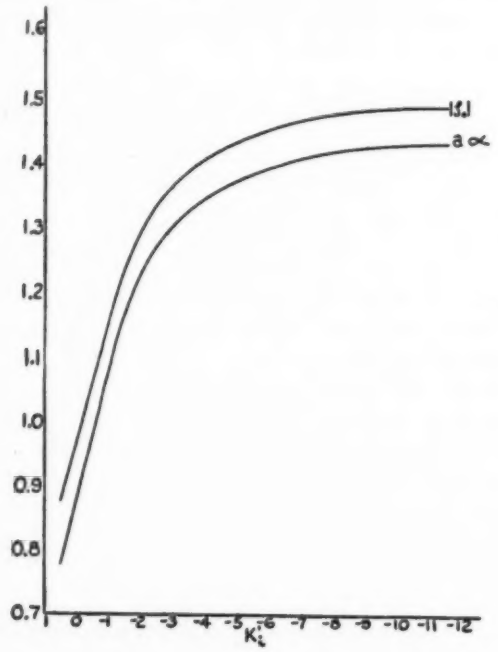

FIG. 2. ζ_0 and $a\alpha$ plotted as functions of K_i' for the lossless case when ζ_0 is real.

[12] Hondros and Debye, Ann. d. Physik **32**, 465 (1910).

We have not examined what occurs for $K_i'>-1$. But we will discuss this below.

Numerical Solution

We now put Eq. (2) into the form:

$$K_c'J_1(\zeta_i)\zeta_0\chi(b/a,\zeta_0)=\zeta_iJ_0(\zeta_i)\psi(b/a,\zeta_0), \tag{11}$$

where

$$\chi(b/a,\zeta_0)\equiv J_0(\zeta_0)N_0[(b/a)\zeta_0]-J_0[(b/a)\zeta_0]N_0(\zeta_0), \tag{12a}$$

and

$$\psi(b/a,\zeta_0)\equiv J_1(\zeta_0)N_0[(b/a)\zeta_0]-J_0[(b/a)\zeta_0]N_1(\zeta_0). \tag{12b}$$

The auxiliary Eq. (3) remains the same.

The values of the ratios b/a, and λ_0/a were taken to be 3, and 5π, respectively. These are the values used by Kerr,[3] in his experiment. Thus Eq. (3) becomes:

$$0.16(K_c'-1)=\zeta_i^2-\zeta_0^2; \tag{13}$$

also

$$\zeta_0=(a^2\gamma^2+0.16)^{\frac{1}{2}}, \quad \zeta_i=(a^2\gamma^2+0.16K_c')^{\frac{1}{2}}. \tag{14}$$

Because χ and ψ are functions of ζ_0 only for constant b/a, it seems wise to use a trial and error method with ζ_0 as our independent variable. Also, since ζ_0 is limited to the first quadrant as is easily seen, our task is thereby lessened. Therefore χ and ψ were computed as functions[13,14] of $|\zeta_0|$ for constant arguments of ζ_0. The

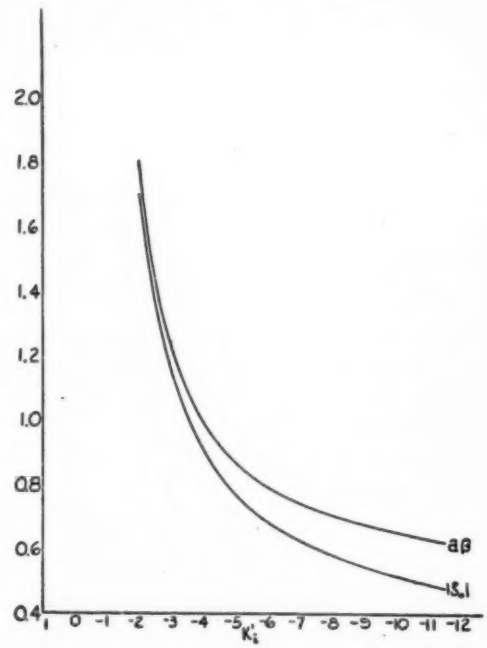

FIG. 3. ζ_0 and $a\beta$ plotted as functions of K_i' for the lossless case when ζ_0 is imaginary.

[13] *Table of the Bessel Functions $J_0(z)$ and $J_1(z)$ for Complex Arguments*, Math. Tables Proj. (Columbia University Press, New York, 1943).

[14] *Table of Bessel Functions of the Second Kind $Y_0(z)$ and $Y_1(z)$ for Complex Arguments*, Math. Tables Proj. (microfilm copy).

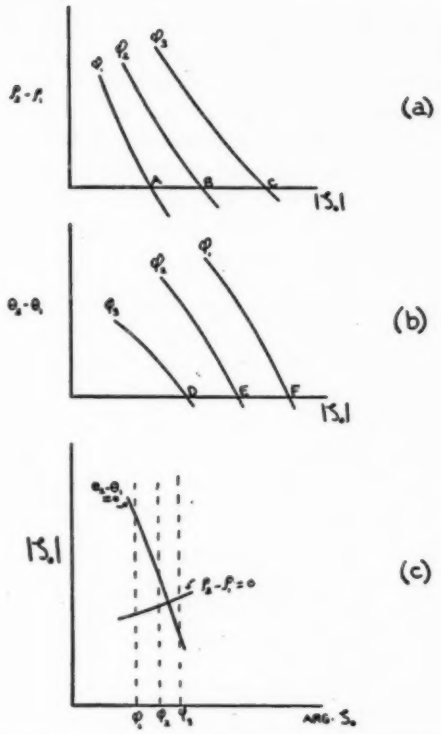

FIG. 4. (a) $\rho_2-\rho_1$ plotted against trial values of $|\zeta_0|$ for various values of φ, the argument of ζ_0; (b) $\theta_2-\theta_1$ plotted against trial values of $|\zeta_0|$ for various values of φ; (c) the curves of $\rho_2-\rho_1=0$ and $\theta_2-\theta_1=0$ plotted in the ζ_0 plane, the intersection of which is the solution.

arguments of ζ_0 were chosen in the range 0°–90°, and were spaced at 5° intervals. As for the absolute values, $|\zeta_0|$, the range was chosen from $|\zeta_0|=0$ to $|\zeta_0|=1.60$ and intervals of 0.10 were used.

The reason for choosing this range of $|\zeta_0|$ is as follows. In our work we shall be interested only in the solutions of Eqs. (11) and (13) yielding the lowest attenuation. If no discharge is taking place in the central region, the dielectric coefficient of the center is equal to unity and we have essentially a cylindrical wave guide. The mode for a cylindrical wave guide which is both circularly symmetric and is attenuated least is the TM_{01} mode for which $\zeta_0=2.405/3\approx 0.8$.[9] If one starts with this mode and changes K_c' continuously, it is possible to follow the solutions and they should be of lowest attenuation. If now the center conductor has $|K_c'|=\infty$, the mode of the cylindrical guide will either change to the TM_{01} mode of the coaxial line with $\zeta_0=\pi/2$, or become the TEM mode ($\zeta_0=0$). It seems more probable that a cylindrical guide excited with the TM_{01} mode will tend to go into the mode having a field configuration most nearly like it, if a center conductor is added with $|K_c'|=\infty$. In as much as the TM_{01} mode of the cylindrical guide has the same field configuration as the TEM mode of the "coax" (except for the axial electric field) we expect the TEM mode of the "coax" as $|K_c'|\to\infty$. But our work is definitely incomplete in its restriction to this transition.

Real K_c'

We first consider the conductivity equal to zero. Since γ can then either be a pure positive imaginary or a pure positive real if $\sigma=0$, ζ_0 must be either a pure positive imaginary or a pure positive real.

Let us consider ζ_0, real. For a particular K_i' we choose a trial ζ_0 and substitute this ζ_0 into Eq. (13) to find the corresponding ζ_i. With this particular pair, ζ_0, ζ_i we

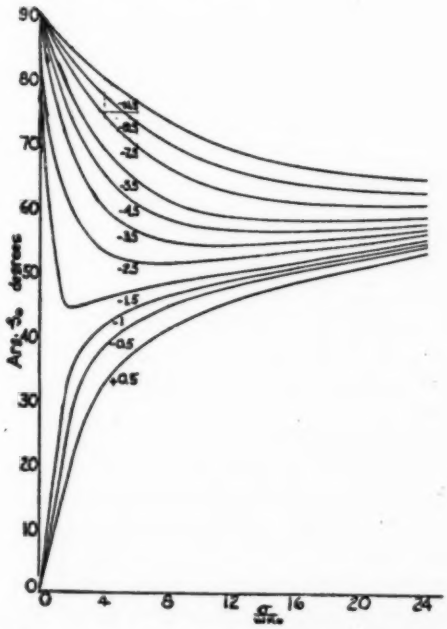

FIG. 5. The argument of ζ_0 is plotted as a function of $\sigma/(\omega K_0)$ holding K_i' constant for various values of K_i'.

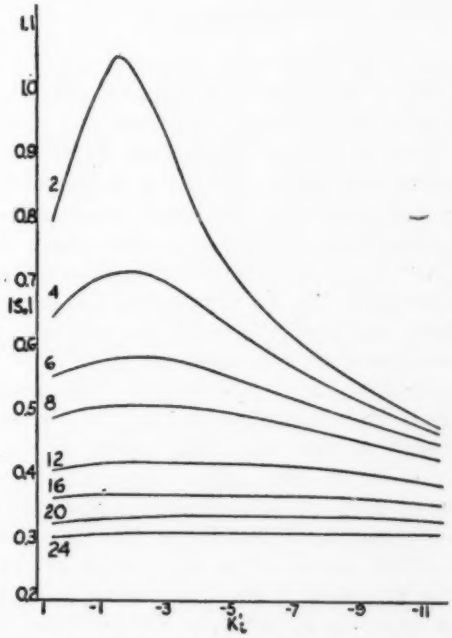

FIG. 6. The absolute value of ζ_0 is shown as a function of K_i' with $\sigma/(\omega K_0)$ taking on various constant values.

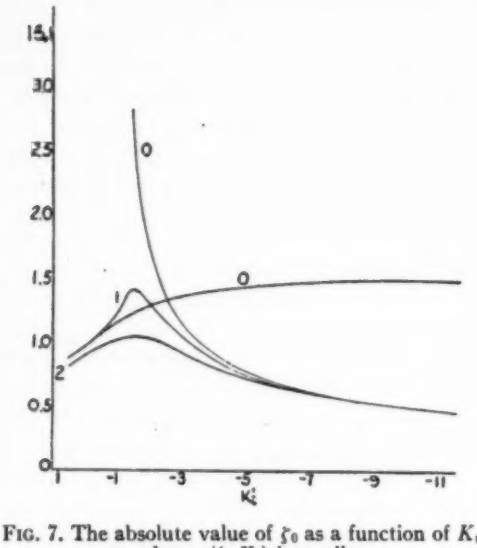

FIG. 7. The absolute value of ζ_0 as a function of K_i' when $\sigma/(\omega K_0)$ is small.

find both the left and right hand sides of Eq. (11), and when the difference between these is plotted against the trial ζ_0, we obtain a zero difference for the correct value of ζ_0. In this manner Fig. 2 is obtained. Values of K_i' from 0.5 to -11.5 inclusive with intervals of 1 were used here. Figure 2 shows that when no discharge is taking place in the center region ($K_i'=1$), $|\zeta_0|\simeq 0.8$ (TM_{01} mode of cylindrical guide), and when K_i' becomes extremely negative, $|\zeta_0|\to\pi/2$ (TM_{01} mode of coaxial line). Also plotted in Fig. 2 is the product $a\alpha$ (α is the real part of γ), obtained from the ζ_0 curve. Because of the values used here for b/a and λ_0/a these solutions yield completely attenuated waves.

Imaginary ζ_0

With ζ_0 imaginary and with the same method as above, Fig. 3 is obtained. This figure verifies what was found from Eqs. (7) and (10). Namely, for $K_i'=-1$, $\zeta_0=i\infty$ and that $\zeta_0\to 0$ (TEM mode) as $K_i'\to-\infty$. Also for K_i' slightly below -1, the propagation resembles that in a dielectric rod. One other important result can be obtained from Fig. 3; it is that above $K_i'=-1$, $(-1<K_i'\leqslant 1)$ no solution can be found for imaginary ζ_0.

Also shown in Fig. 3 is the product $a\beta$ plotted against K_i'. Solutions with ζ_0 a positive imaginary can yield only completely unattenuated waves.

It was stated previously that the TM_{01} mode of the cylindrical guide can either go into the TEM mode of the "coax" or into the TM_{01} mode of the "coax" as $|K_c'|\to\infty$. If the conductivity is zero and one started out with a cylindrical guide and makes K_i' progressively less than 1, continuing into negative values, we can either arrive at the TM_{01} mode of the "coax" ($\zeta_0=\pi/2$) as shown in Fig. 2 or we can make a discontinuous jump in ζ_0 at $K_i'=-1$ and then continue downward along the positive imaginary axis to the TEM mode of the "coax" ($\zeta_0=0$) as shown in Fig. 3. The latter alternative means that ζ_0 in Fig. 3 is really a continuation of the part of ζ_0 in Fig. 2 above $K_i'=-1$. This latter alternative, as will be seen below, gives rise to continuous curves when the conductivity is not zero. It is this case that will be investigated, that is, the case where the TEM mode of the "coax" is approached as $|K_c'|\to\infty$.

Complex K_c'

We are now ready to deal with the case where the dielectric coefficient is complex. The method used for real or imaginary ζ_0 is not useful here since the difference between the right- and left-hand sides of Eq. (11) is a complex number and cannot be plotted readily against the complex trial ζ_0. However, if the left-hand side of Eq. (11) is put into the form $\rho_1 e^{i\theta_1}$ and the right-hand side into $\rho_2 e^{i\theta_2}$, the following method can be used.

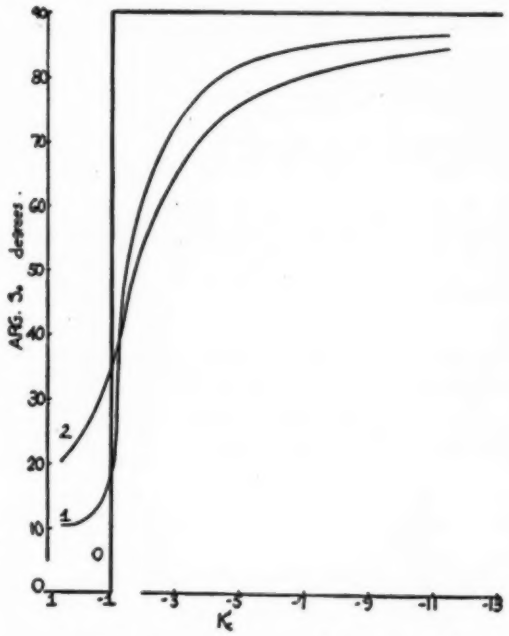

FIG. 8. The argument of ζ_0 as a function of K_i' when $\sigma/(\omega K_0)$ is held constant.

Plot $\rho_2-\rho_1$ as a function of $|\zeta_0|$ for various constant arguments of $\zeta_0(\varphi_1, \varphi_2, \varphi_3)$ and also plot $\theta_2-\theta_1$ in a similar manner (see Fig. 4(a), (b)). Then in Fig. 4(a), points A, B, C are points where $\rho_2-\rho_1=0$, and in Fig. 4(b) points D, E, F are points where $\theta_2-\theta_1=0$. When the curves of $\rho_2-\rho_1=0$ (determined by A, B, C) and of $\theta_2-\theta_1=0$ (determined by D, E, F) are plotted on the ζ_0 plane (Fig. 4(c)) we get an intersection where $\rho_1=\rho_2$ and where $\theta_1=\theta_2$. This is our solution, that is the value of ζ_0 which satisfies both Eqs. (11) and (13) for a particular K_c'.

The values of the imaginary part of K_c' were taken in the range 0 to -24 inclusive with steps of 2 and the range of the real part of K_c' was the same as before. Thus $-11.5\leqslant K_i'\leqslant 0.5$, $0\leqslant(\sigma/\omega K_0)\leqslant 24$.

At the start it was found best to begin with the imaginary part of K_c' small, so that the solution would lie not far off the real or imaginary axis, as the case may be. Then we progressively decrease the imaginary part of K_c' and follow our solution along. Thus we could narrow down the region in the ζ_0 plane where our solution occurred. We could then use 2 arguments of ζ_0 spaced 5° apart for our trial solution and 2 straight lines for the curves of $\rho_2-\rho_1=0$ and $\theta_2-\theta_1=0$. In this manner Figs. 5, 6, 7 were obtained.

Figure 5 which is a plot of the $\arg\zeta_0$ against $\sigma/(\omega K_0)$ for constant K_i' shows that as the imaginary part of K_c' decreases the argument ζ_0 approaches 67.5°. This was found previously from Eq. (7). It is also seen from Fig. 5 that curves of constant K_i' for $K_i' \geqslant -1$ start from 0° and for $K_i' \leqslant -1$ they start from 90°. At $K_i'=-1$ the curve goes down to 0° and then passes discontinuously up along the axis of ordinates to 90°. This is better seen from Fig. 8 which is a cross plot of Fig. 5. In this figure we note the discontinuous jump at $K_i'=-1$ for $\sigma/(\omega K_0)=0$. However, if $(\sigma/\omega K_0)\neq 0$, we obtain a continuous transition. This was mentioned previously when it was stated that the TM_{01} mode of the cylindrical guide ($K_i'=1$) will either become the

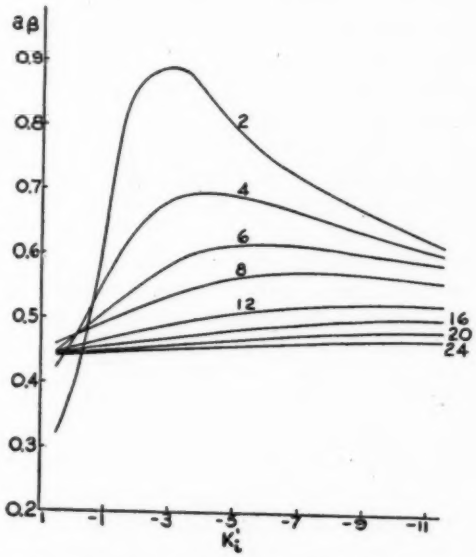

FIG. 9. The product $a\beta$ is plotted against K_i' when $\sigma/(\omega K_0)$ takes on various constant values.

TEM mode or the TM_{01} mode of the coaxial line as K_i' approaches $-\infty$.

Figures 6 and 7 which are plots of $|\zeta_0|$ against K_i' for constant $\sigma/(\omega K_0)$ show resonance type curves. That is, the peaks are steeper and narrower as the losses become smaller. Also the curves in Fig. 8 resemble the phase angle curves obtained in radio resonance measurements. This resonance behavior was hinted at in Eq. (10). Figure 6 also shows us that $|\zeta_0|$ approaches zero (TEM mode) as $|K_c'|$ goes to ∞. This is just the solution we wanted.

The solution in which the TM_{01} mode of the "coax" is approached as $|K_c'|\to\infty$ has not been investigated. This solution will yield waves of greater attenuation. Since no anomalies were found in the results here obtained, this solution either does not intersect with the solutions investigated or it is tangential at regions where the solutions become one and the same.

Figure 7 shows $|\zeta_0|$ plotted against K_i' for low values of $\sigma/(\omega K_0)$. The part of the curve for $\sigma/(\omega K_0)=0$ which approaches $\zeta_0=\pi/2$ (TM_{01} mode of "coax") is to be ignored for the solution of interest in the region $K_i' \leqslant -1$ because of what was said previously. The extreme steepness of the curve for $\sigma/(\omega K_0)=1$ indicates that numerical work in the low conductivity region is not as precise as for the higher conductivity regions. However, an over-all probable error in both $|\zeta_0|$ and $\arg\zeta_0$ is estimated to be about 1 percent and the maximum error in each is about 2 percent.

Figures 9–13 show plots of $a\alpha$ and $a\beta$ which were obtained from the curves of ζ_0. In Fig. 11 the curve for $\sigma/(\omega K_0)=0$, $K_i' \geqslant -1$ lies along the axis of the abscissae, i.e., $a\beta=0$. In Fig. 12 the curve for $\sigma/(\omega K_0)=0$ for the solution of interest is the one indicated by the arrows. This curve has a discontinuity at $K_i'=-1$ and then lies along the axis of the abscissae ($a\alpha=0$) for $K_i' \leqslant -1$. The other solution for $\sigma/(\omega K_0)=0$ yields a curve that approaches $a\alpha=1.52$ at $K_i'=-\infty$.

In Fig. 13, we have drawn a map of $a\gamma$ as a function of K_i'. That is, curves of constant K_i' and constant $\sigma/(\omega K_0)$ which intersect are plotted in the $a\gamma$ plane. (For some unknown reason) these curves seem to be nearly orthogonal to each other. This figure should be most useful for obtaining information at a glance.

We should mention that for $K_c'=1$ (cylindrical wave guide) we could have any of the higher circularly sym-

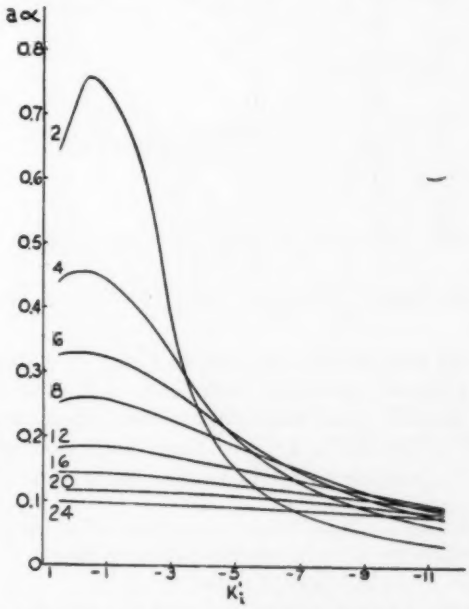

FIG. 10. The product $a\alpha$ is plotted against K_i' when $\sigma/(\omega K_0)$ takes on various constant values.

metric modes. That is, we could have started with any of the TM_{0n} modes of the cylindrical guide at $K_c'=1$. We have chosen to start with the TM_{01} mode because it has the lowest attenuation. To investigate these other solutions would involve tremendous labor and is at present not feasible. Besides, tables of the Bessel functions for complex arguments are not available for absolute values of the arguments of the Bessel functions beyond 10.

C. COMPARISON WITH EXPERIMENT

Kerr obtained standing waves by placing a shorting bar at one end of the wave guide and used a traveling E-probe and a standing wave detector to measure the dependence of the radial electric field E_r on the axial distance from the short. He intended to measure the attenuation, α and the phase constant, β, by this method. If the short is placed at $Z=L$, the theoretical dependence of E_r on the distance from the shorted end is:[2,3]

$$E_r \sim [\cosh(2\alpha x)-\cos(2\beta x)]^{\frac{1}{2}}, \quad x \equiv Z-L.\dagger$$

By comparing this with the experimental dependence of E_r on x, Kerr was able to determine α and β. By varying the direct current in the arc he obtained information on how α and β vary with arc current.

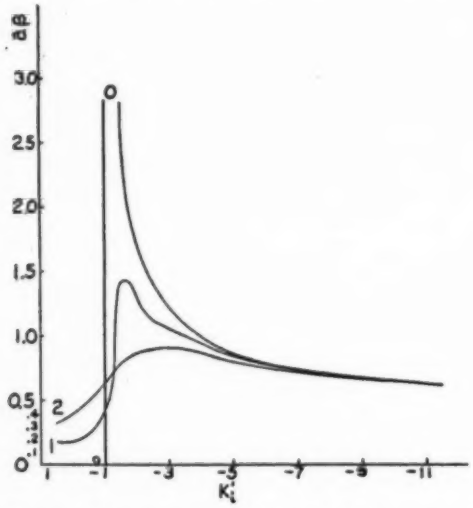

FIG. 11. The product $a\beta$ as a function of K_i' when $\sigma/(\omega K_0)$ is small.

It is the purpose of this work to find γ as a function of the complex dielectric coefficient, K_c', of the discharge. Thus if α and β are known from experiment the value of K_c' would be known. Therefore, knowing K_c', it may be possible to relate certain parameters of the discharge, such as electron mean free path, collision cross sections and the number of electrons per cc, with its measurable properties (see Appendix).

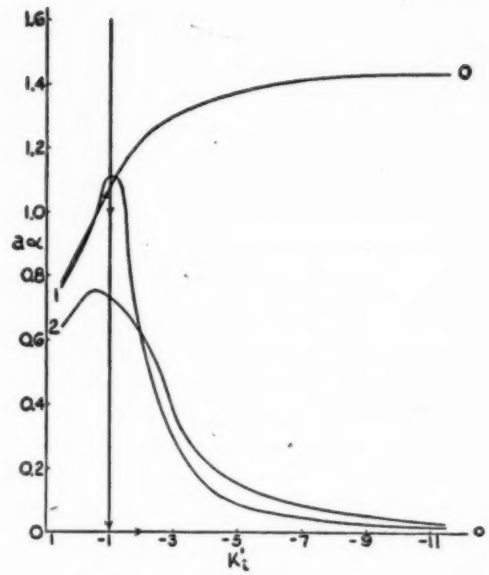

FIG. 12. The product $a\alpha$ as a function of K_i' when $\sigma/(\omega K_0)$ is small.

Available data are not as good as is desirable. Difficulties arise from leakage of the field through a hole made by the arc and because of the fluctuation of certain discharge parameters. The latter reason is most important since, as will be seen, the data indicate $\sigma/(\omega K_0)$ is small and good data are difficult to obtain in a region where the curves of Figs. 6 and 7 are steep. However, a definite trend is observed.

For zero arc current ($K_i'=1$), $\zeta_0 \simeq 0.7$ and as the current is increased ζ_0 remains substantially real, increasing to approximately unity at a current near 1 ampere; ζ_0 may have a very small imaginary component, but this is very difficult to measure. Upon increasing the arc current further, a discontinuity occurs with ζ_0 becoming nearly a pure imaginary (the $\arg\zeta_0$ remaining at 86°) and $|\zeta_0|$ decreases from about 1.3 at 1 ampere to about 0.6 at 1.4 ampere.

In terms of α and β this can be described as follows. At zero current β is zero and the wave is attenuated. As the current increases β remains either zero or is very small while α increases rapidly. Then we have (at the discontinuity) a sharp drop in α, while β becomes high suddenly. Finally, α becomes smaller still while β drops and approaches the free space value (TEM mode) at the highest current.

The facts can be explained by our results. Initially at zero arc current we have cylindrical guide with $\zeta_0 \simeq 0.8$. With the discharge present, at low currents, we have a low pressure discharge through which high frequency waves are passing. Therefore, we should expect K_c' to be real or nearly so (see Appendix). We can therefore explain the low current data with the part of Fig. 2 for $K_i'>-1$, i.e., ζ_0 rises to approximately unity as K_i'

† This is seen as follows. Since we now have waves traveling in both directions along the axis of the cylinder we have:

$$E_r \sim (B_1 e^{-\gamma Z} - B_2 e^{+\gamma Z}) f(r).$$

At $Z=L$, $E_r=0$ for all r and therefore $B_2/B_1=e^{-2\gamma L}$. If we choose $B_1=\frac{1}{2}$, we have: $E_r \sim \sinh(\gamma x)$. Now since E-probe measures $(E_r E_r^*)^{\frac{1}{2}}$ we have $(E_r)x$ dependent part $\sim(\cosh 2\alpha x - \cos 2\beta x)^{\frac{1}{2}}$.

decreases. The decrease in K_i' is due to the fact that the electron density is increasing as the arc current goes up (see Appendix).

The discontinuity between the low and high current regions indicates the conductivity is very low. This is so because as was seen previously, a violent jump in the $\arg\zeta_0$ from 0° to about 90° takes place at $K_i'=-1$ when the conductivity is low. The fact that $\sigma/(\omega K_0)$ is small and that $K_i'\approx-1$ is seen from the fact that just after the discontinuity $|\zeta_0|=1.3$ and the $\arg\zeta_0=86°$ (see Figs. 5, 7, 8). Then, finally as the current increases further $|\zeta_0|$ is decreasing and approaching $\zeta_0=0$ (TEM mode) since K_i' is going to high negative values. This is seen from the data at 1.4 amp. ($|\zeta_0|=0.6$, $\arg\zeta_0=86°$), which means $K_i'\approx-8$ and $\sigma/(\omega K_0)\approx 2$ (see Figs. 5 and 6).

The reason the conductivity, which was previously infinitesimal, has increased is because the pressure of the arc and the d.c. field maintaining it have increased with arc current (see Appendix).

Professor Allis[3] of M.I.T. has estimated the data at 1.4 ampere ($|\zeta_0|=0.6$, $\arg\zeta_0=86°$) to mean that $K_i'\approx-8$, $\sigma/(\pi K_0)\approx 2$. He used a power series approximation in the high current region. These results check ours semi-quantitatively.

One sees many practical aspects of the wave guide with a coaxial d.c. discharge. By controlling the discharge current one can vary the impedance of wave guide continuously. Also because of the fact that at a particular arc current, a rapid transition occurs between a completely attenuated wave and a propagated wave with small attenuation whose phase constant is a continuous function of arc current, this wave guide can be used as a radio frequency switch and as a modulator.

APPENDIX

Above we had assumed that Ohm's law held. Now we wish to justify this assumption theoretically using the methods of kinetic theory. We will show that $\mathbf{J}_{A.C.}=\sigma_c\mathbf{E}_{A.C.}$, where σ_c is a function of the d.c. field.

Consider the Boltzmann transfer equation:[15-17]

$$\partial f/\partial t+\mathbf{v}\cdot\nabla f+\mathbf{a}\cdot\nabla f=\delta f/\delta t|_c, \qquad (15)$$

where f is the distribution function of electron velocities$\equiv f(\mathbf{v}, \mathbf{r}, t)$; $\mathbf{v}$ is the velocity, $\mathbf{a}$ is the acceleration, $\mathbf{r}$ is the position vector in configuration space, ∇ and ∇ denote the gradients in configuration and velocity space respectively, and $\delta f/\delta t|_c$ denotes the rate of change in f due to encounters.

Let

$$f=f^{(0)}+(1/v)\mathbf{v}\cdot\mathbf{f}^{(1)}. \qquad (16)$$

This is the start of an expansion of f in spherical harmonics;[16] those spherical harmonics higher than the second are neglected. Then if Eq. (16) is substituted into Eq. (15) provided that $\mathbf{a}=(e\mathbf{E}/m)$ where e, m are the electron charge and mass, respectively, we obtain:

$$\frac{\partial f^{(0)}}{\partial t}+\frac{\mathbf{v}}{v}\cdot\frac{\partial\mathbf{f}^{(1)}}{\partial t}+\mathbf{v}\cdot\nabla f^{(0)}+\mathbf{v}\cdot\nabla\left(\frac{\mathbf{v}\cdot\mathbf{f}^{(1)}}{v}\right)+\frac{e\mathbf{E}}{m}\cdot\nabla f+\frac{e\mathbf{E}}{m}\cdot\nabla\left(\frac{\mathbf{v}\cdot\mathbf{f}^{(1)}}{v}\right)=\frac{\delta f^{(0)}}{\delta t}\bigg|_c+\frac{\delta}{\delta t}\left(\frac{\mathbf{v}\cdot\mathbf{f}^{(1)}}{v}\right)\bigg|_c. \qquad (17)$$

If we only consider encounters with molecules, then it can be shown that:[16, 18]

$$\frac{\delta(\mathbf{v}\cdot\mathbf{f}^{(1)}/v)}{\delta t}\bigg|_c=-\frac{\mathbf{v}\cdot\mathbf{f}^{(1)}}{vl}, \qquad (18)$$

where l is the gas kinetic mean free path. Upon using Eq. (18), Eq. (17) yields two equations; one contains terms linear in v_x, v_y, v_z and the other contains constant terms and terms containing v_x^2, v_y^2, v_z^2; v_xv_y, v_xv_z etc.

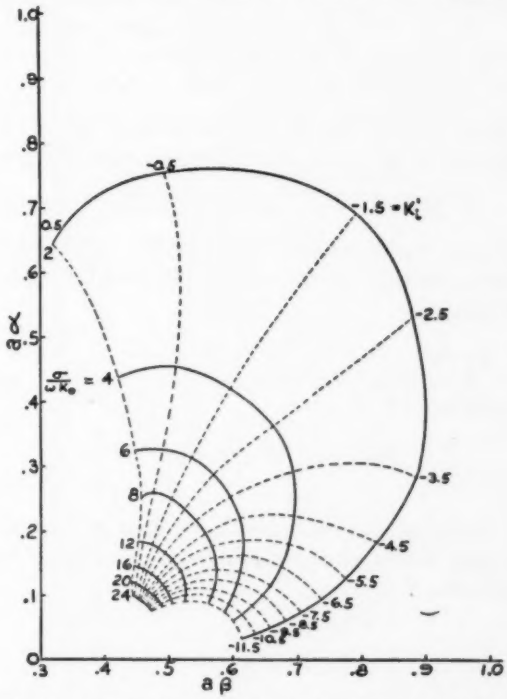

FIG. 13. Curves of constant K_i' and constant $\sigma/(\omega K_0)$ plotted in the $a\gamma$ plane.

The equation linear in v_x, v_y, v_z is:

$$\frac{\mathbf{v}}{v}\cdot\frac{\partial\mathbf{f}^{(1)}}{\partial t}+\mathbf{v}\cdot\nabla f^{(0)}+\frac{e\mathbf{E}}{m}\cdot\frac{\partial f^{(0)}}{\partial v}\frac{\mathbf{v}}{v}+\frac{\mathbf{v}\cdot\mathbf{f}^{(1)}}{l}=0, \qquad (19a)$$

and the remainder:

$$\frac{\partial f^{(0)}}{\partial t}+\frac{\mathbf{v}\cdot\nabla f^{(1)}\cdot\mathbf{v}}{v}+\frac{e\mathbf{E}}{m}\cdot\nabla\left(\frac{\mathbf{v}\cdot\mathbf{f}^{(1)}}{v}\right)=\frac{\delta f^{(0)}}{\delta t}\bigg|_c. \qquad (19b)$$

[15] S. Chapman and T. G. Cowling, *The Mathematical Theory of Non-Uniform Gases* (The Cambridge University Press, New York, 1939), Chapter 3.

[16] H. Margenau, Phys. Rev. **73**, 297–308 (1948).

[17] H. Margenau, Phys. Rev. **69**, 508–513 (1946)

[18] See reference 15, pp. 384 ff.

If our distribution is homogeneous (neglecting diffusion) $\nabla f^{(0)}=0$ and $\nabla\cdot\mathbf{f}^{(1)}=0$. Equation (19a) becomes after factoring out the $\mathbf{v}\cdot$ ($\mathbf{v}$ is arbitrary):

$$\frac{1}{v}\frac{\partial \mathbf{f}^{(1)}}{\partial t}+\frac{1}{v}\frac{\partial f^{(0)}}{\partial v}\frac{e}{m}\mathbf{E}=-\frac{\mathbf{f}^{(1)}}{l}. \tag{20}$$

If we average Eq. (20) over all directions of $\mathbf{v}$ we get no new result. However, averaging Eq. (19b) over all directions of $\mathbf{v}$ yields something different. We have:

$$\left(\frac{\mathbf{v}\cdot\nabla\mathbf{f}^{(1)}\cdot\mathbf{v}}{v}\right)_{\text{av}}=\frac{v}{3}\nabla\cdot\mathbf{f}^{(1)}=0,$$

and

$$\left[\nabla\left(\frac{\mathbf{v}\cdot\mathbf{f}^{(1)}}{v}\right)\right]_{\text{av}}=\frac{1}{3v^2}\frac{\partial}{\partial v}(v^2\mathbf{f}^{(1)}).$$

Now in the steady state $\partial f^{(0)}/\partial t=0$, if the electron density is to remain constant. Thus, Eq. (19b), when averaged, finally becomes:

$$\frac{1}{3v^2}\frac{\partial}{\partial v}\left(\frac{\mathbf{v}^2 e}{m}\mathbf{E}\cdot\mathbf{f}^{(1)}\right)=\left.\frac{\delta f^{(0)}}{\delta t}\right|_e. \tag{21}$$

Now suppose $\mathbf{E}=\mathbf{E}_{\text{d.c.}}+\mathbf{E}_{\text{a.c.}}=\mathbf{E}_0+\mathbf{E}_1e^{i\omega t}$. The field will induce the corresponding frequencies in $\mathbf{f}^{(1)}$ so that:

$$\mathbf{f}^{(1)}=\mathbf{F}_0{}^{(1)}+\mathbf{F}_1{}^{(1)}e^{i\omega t},\quad\text{where}\quad\mathbf{F}_1{}^{(1)}=\mathbf{u}+i\mathbf{w}.$$

$\mathbf{F}_1{}^{(1)}$ is complex because we might have a phase change. If we substitute the real parts of $\mathbf{f}^{(1)}$ and $\mathbf{E}$ into Eq. (21) we obtain:

$$\frac{1}{3v^2}\frac{\partial}{\partial v}\left[\frac{\mathbf{v}^2\mathbf{e}}{m}\text{ Real part }(\mathbf{E}_0+\mathbf{E}_1e^{i\omega t})\cdot\text{Real part }(\mathbf{F}_0{}^{(1)}+\mathbf{F}_1{}^{(1)}e^{i\omega t})\right]=\left.\frac{\delta f^{(0)}}{\delta t}\right|_e. \tag{22}$$

We must use the real parts here since $f^{(0)}$ is real. Also Eq. (20) yields after equating static and time dependent parts:

$$\mathbf{F}_0{}^{(1)}=-\frac{l}{v}\frac{\partial f^{(0)}}{\partial v}\frac{e\mathbf{E}_0}{m} \tag{23a}$$

$$\left(\frac{i\omega l+1}{v}\right)\mathbf{F}_1{}^{(1)}=-\frac{l}{v}\frac{\partial f^{(0)}}{\partial v}\frac{e\mathbf{E}_1}{m}. \tag{23b}$$

Instead of Eq. (23b) we have:

$$\mathbf{u}=-\frac{vl(\partial f^{(0)}/\partial v)(e\mathbf{E}_1/m)}{v^2+\omega^2l^2},\qquad\mathbf{w}=\frac{\omega l^2(\partial f^{(0)}/\partial v)(e\mathbf{E}_1/m)}{v^2+\omega^2l^2}.$$

By virtue of these results Eq. (22), when averaged over t ($f^{(0)}$ is independent of time) becomes:

$$-\frac{1}{3v^2}\frac{\partial}{\partial v}\left\{\frac{vle^2}{m^2}\frac{\partial f^{(0)}}{\partial v}\left[E_0{}^2+\frac{\frac{1}{2}E_1{}^2}{1+(\omega^2l^2/v^2)}\right]\right\}=\left.\frac{\delta f^{(0)}}{\delta t}\right|_e. \tag{24}$$

If $E_1\ll E_0$ whether $\omega l/v$ is large or small compared with unity, we can neglect the term containing $(E_1)^2$. This assumption is certainly true for a weak signal passing through a discharge maintained by a high d.c. potential. Also since the discharge is maintained by a high d.c. field, with collisions mostly inelastic, one can assume with some assurance that the rate of change of $f^{(0)}$ with encounters is independent of $E_{\text{a.c.}}$, the alternating field. Thus from Eq. (24), we see that $f^{(0)}$ is independent of $E_{\text{a.c.}}$.

Now the current density $\mathbf{J}=ne\bar{\mathbf{v}}$ where n is the electron density and $\bar{\mathbf{v}}$ is the average electron velocity. We find $\bar{\mathbf{v}}$ as follows:

$$\bar{\mathbf{v}}=\frac{1}{n}\int_0^\infty\int_0^\pi\int_0^{2\pi}\mathbf{v}fv^2dv\sin\theta d\theta d\varphi,$$

where θ, φ are the polar angle and azimuth in velocity space. However, since $f=f^{(0)}+(\mathbf{v}/v)\mathbf{f}^{(1)}$, we obtain

$$\bar{\mathbf{v}}=4\pi/3n\int_0^\infty\mathbf{f}^{(1)}v^3dv.$$

Thus:

$$\mathbf{J}=(4\pi e)/3\int_0^\infty(\mathbf{F}_0{}^{(1)}+\mathbf{F}_1{}^{(1)}e^{i\omega t})v^3dv,$$

and using Eqs. (23a) and (23b) we have:

$$\mathbf{J}=-\frac{4\pi e}{3}\int_0^\infty\frac{le}{vm}\frac{\partial f^{(0)}}{\partial v}\left[\mathbf{E}_0+\frac{\mathbf{E}_1e^{i\omega t}}{1+i\omega l/v}\right]v^3dv.$$

We see therefore that the alternating current density $\mathbf{J}_{\text{a.c.}}=\sigma_c\mathbf{E}_{\text{a.c.}}$ where:

$$\sigma_c=-\frac{4\pi e}{3}\int_0^\infty\frac{le}{vm}\frac{\partial f^{(0)}}{\partial v}\left[\frac{1}{1+(i\omega l/v)}\right]v^3dv. \tag{25}$$

Thus Ohm's law holds, since σ_c is independent of $E_{\text{a.c.}}$.

Since we have assumed that the discharge is maintained solely by the high d.c. field such that the ratio of inelastic to elastic collisions is high it should prove interesting to substitute an expression for $f^{(0)}$ which is suited to such a case, into Eq. (25). An expression for $f^{(0)}$ which is Maxwellian, holds[16] under the condition that the probability of an inelastic encounter is inversely proportional to the energy. This Maxwellian formula: $f^{(0)}=A\exp(-hv^2)$ is a special case of a more complicated expression, and it is used here for the sake of simplicity. Here, $h^2=[\frac{3}{2}m^2/l_{\text{in}}l(eE_0)^2]$, where l_{in} is the inelastic mean free path, and A is a normalization constant found to be $n(h/\pi)^{\frac{3}{2}}$. If the above Maxwellian expression is substituted into Eq. (43), we obtain an expression exactly the same as was found by H. Margenau,[17] except for the fact that the temperature of the electron gas is different. This expression is:

$$\sigma_c=\frac{4}{3}\frac{e^2ln}{(2\pi mkT)^{\frac{1}{2}}}[\bar{K}_2(x_1)-ix_1{}^{\frac{1}{2}}\bar{K}_{3/2}(x_1)], \tag{26}$$

where k is the Boltzmann constant, T is the absolute temperature, $x_1=[m(\omega l)^2/2kT]$ and where:

$$\bar{K}_p(x_1)=\int_0^\infty \frac{x^p e^{-x}}{x_1+x}dx \quad x=\frac{mv^2}{2kT}.$$

These $\bar{K}$'s have been shown[17] to be expressible in terms of the exponential integral, $E_i(-x_1)$, and the error function erf$[(x_1)^{\frac{1}{2}}]$. The only difference between our case and that of Margenau is that our temperature $T=(ll_{in}/6)^{\frac{1}{2}}(eE_0)/k$ as can easily be seen since $h=m/(2kT)$ for a Maxwellian distribution.

Now since $x_1=[m(\omega l)^2/2kT]$, we have

$$x_1=\frac{(6)^{\frac{1}{2}}}{2}\frac{m\omega^2}{eE_0}\frac{l^2}{(ll_{in})^{\frac{1}{2}}}. \tag{27}$$

With moderate d.c. fields, for high frequency waves traveling through a low pressure gas, $x_1\to\infty$. Again using Margenau's result for this limiting case, we find for our problem

$$J_{a.c.}=\frac{16}{3}\frac{e^2n}{m\omega^2 l}\left(\frac{eE_0}{2\pi m}\right)^{\frac{1}{2}}\left(\frac{ll_{in}}{6}\right)^{\frac{1}{2}}E_1\cos\omega t + \frac{e^2n}{m\omega}E_1\sin\omega t. \tag{28}$$

For moderate d.c. fields, and extremely high frequency waves passing through a very low pressure gas only the second term on the right of Eq. (28) is of importance.

Thus the imaginary part of conductivity $\sigma_I=-(e^2n/m\omega)$. The effective dielectric constant, $K=\epsilon+(\sigma_I/\omega)$, becomes:

$$K=\epsilon-(e^2n/m\omega^2). \tag{29}$$

But for most gases that are not composed of permanent dipoles and especially if the gas is of low density, ϵ has the value K_0, the dielectric constant of vacuum.[19] Thus the dielectric coefficient

$$K'=1-(e^2n/m\omega^2K_0). \tag{30}$$

We see therefore that at high electron densities, the dielectric coefficient is less than unity and may be negative.

The author wishes to express his appreciation to Professor Henry Margenau for suggesting this problem and for the indispensable assistance, advice and encouragement he has given him.

The author also wishes to express his gratitude to Professor W. P. Allis and D. E. Kerr of M.I.T. for their stimulating discussions of this problem.

[19] Leigh Page, *Introduction to Theoretical Physics* (D. Van Nostrand Company, Inc., New York, 1935), p. 383.

Magnetically Controlled Wave-Guide Attenuators

THEODORE MILLER
Westinghouse Research Laboratories, East Pittsburgh, Pennsylvania
(Received January 27, 1949)

It has been observed that the microwave power loss of a section of wave guide filled with iron powder material could be varied by subjecting the iron powder to an externally applied magnetic field. This paper describes some experiments performed with various kinds of iron powders. Measurements have been made with the magnetic field applied parallel to, and perpendicular to the plane of the magnetic component of the electromagnetic wave inside the guide. The possibility of ferromagnetic resonance is considered. A theoretical formula for the power loss exhibited by low conductivity iron powder attenuators is developed and compared with experimental measurements.

INTRODUCTION

EARLY in 1947 a series of experiments were undertaken at the Westinghouse Research Laboratories to determine the effectiveness of iron powder materials as *X* band wave guide attenuators. While performing certain tests, it was observed that the insertion loss of such attenuators could be varied by subjecting the iron powder to an external magnetic field. In the hope of developing practical magnetically controlled attenuators and wave guide amplitude modulators, a considerable amount of experimental data was collected on the effect of a magnetic field upon the microwave transmission properties of various iron powder slugs completely filling a section of *X* band wave guide excited in the fundamental TE_{01} mode. This paper will present and discuss some of this data. A theoretical formula for the attenuation of iron powder materials inside wave guides will be derived and compared with experimental measurements.

A search of the literature revealed a communication to Nature magazine by J. H. E. Griffith[1] in which is reported the effect of a magnetic field applied to a ferromagnetic film electroplated on the inside wall of a microwave cavity. In a paper by Charles Kittel[2] incidental reference is made to an M.I.T. Radiation Laboratory report describing the characteristics of iron powder cores at microwave frequencies.

More recently W. A. Yager and R. M. Bozorth[3] have published experimental data on the ferromagnetic resonant effect observed with a supermalloy foil in a microwave cavity operating at 24,050 megacycles and subjected to a magnetic biasing field of 4920 gauss. Their results confirm Kittel's[4] theoretical deductions concerning the ferromagnetic resonance effect at microwave frequencies.

Although the experimental procedures reported in this paper are in practice somewhat similar to that reported in the foregoing references (i.e. one observes the effect of a magnetic field on a ferromagnetic material at microwave frequencies), it is believed that the operation of the magnetically controlled iron powder attenuators does not depend primarily upon the ferromagnetic resonance effect. Instead it is thought that the application of the magnetic field varies the incremental permeability of the iron powders, and in this manner the hysteresis and eddy current losses at the microwave frequencies may be controlled by the magnetic field. However in certain cases, possible resonance effects do appear and are described in a subsequent section of this paper.

PREPARATION OF THE ATTENUATORS

The iron powder attenuators were made by mixing in discreet proportions various iron powders with polystyrene insulating material. Before mixing, the polystyrene was first dissolved in 75 cubic centimeters of toluene. After mixing, the solution was spread on a large flat dish, inserted into an oven held at a temperature of 100°C and dried for about 12 hours. The resulting brittle mixture was removed from the plate, inserted into a one-inch diameter mold, heated at a temperature of 140°C until the enclosed polystyrene mixture began to melt, and allowed to cool to room temperature under a pressure of 3000 pounds per square inch. After removal from the mold, the iron powder cylindrical ingot was cut into small slabs which could be inserted into a section of wave guide through narrow vertical slots cut in the side walls of the guide.

EXPERIMENTAL APPARATUS

The block diagram of Fig. 1 represents the wave guide apparatus and associated equipment used in the various experiments to be described. The variable magnetic field required for the experiments was conveniently obtained from a magnetron electromagnet. This magnet is wound with 6000 turns of number 18 wire. The pole faces are 0.75 in diameter, providing an air gap area of 1.727 square inches. The pole faces were set one inch apart and the air gap flux measured as a function of the coil current. The residual flux remaining in the air gap

[1] J. H. E. Griffith, Nature **158**, 670 (1946).
[2] Charles Kittel, "Theory of the dispersion of magnetic permeability in ferromagnetic materials at microwave frequencies," Phys. Rev. **70**, 281 (1946). The report in reference is Rad. Lab. Report No. 906 which to date has not been available to the writer.
[3] W. A. Yager and R. M. Bozorth, "Ferromagnetic resonance at microwave frequencies," Phys. Rev. **72**, 80 (1947).
[4] Charles Kittel, "Interpretation of anomalous Larmor frequencies in the ferromagnetic resonance experiment," Phys. Rev. **71**, 270 (1947).

TABLE I. Physical characteristics of carbonyle iron powders.

Grade	Iron content (%)	Carbon content (%)	Oxygen content (%)	Nitrogen content (%)	% retained by 325 mesh screen	Weight average dia microns	Particle density
L	99.7–99.9	0.005–0.03	0.1–0.2	0.005–0.05	up to 30	20	7.85
HP	99.7–99.8	0.01–0.3	0.1–0.3	0.01–0.1	0.5–2.0	10	7.86
C	99.4–99.8	0.03–0.12	0.1–0.3	0.01–0.1	0.5–2.0	10	7.86
E	97.9–98.3	0.65–0.80	0.45–0.60	0.6–0.7	Trace	8	7.77
TH	98.1–98.5	0.5–0.6	0.5–0.7	0.5–0.6	Trace	5	7.79
SF	98.0–98.3	0.5–0.6	0.7–0.8	0.5–0.6	Trace	3	7.81

after the coil current was reduced to zero was approximately 35 gauss.

The experiments were performed in standard *X* band wave guide with the magnetic field applied in one or the other of two directions. The "*b*−*b*" direction will refer to the situation in which the magnetic field is applied parallel to the broad dimension of the guide. The term "*a*−*a*" direction will be used to designate application of the magnetic field perpendicular to the broad dimension of the guide. Unless otherwise specified all measurements were made at a free space wavelength of 3.2 centimeters and an incident power level of 0.5 milliwatt.

EXPERIMENTS WITH CARBONYLE POWDERS

The first experiments consisted of measuring the microwave transmission characteristics of samples made with various carbonyle iron powders supplied by General Analine and Film Corporation. The physical characteristics of these powders as furnished by the manufacturer are shown in Table I. The samples were all 0.063 inch thick and were cut from ingots made by mixing 1.23 ounces of iron powder with 0.18 ounce of polystyrene. The attenuation loss and reflection coefficient of these samples were measured as a function of the magnetic field applied in the "*b*−*b*" direction. The initial reflection (i.e., reflection at zero magnetizing field) from each of the samples was "matched out" with a three stub tuner situated directly in front of the sample.

The curves of Fig. 2a indicate the performance of the various iron powders as magnetically controlled attenuators. The samples made with the smaller particle size iron powders apparently make the most effective attenuators. The curves of Fig. 2b illustrate the reflection characteristics of these samples.

Several samples were made from an insulated iron powder supplied by the Stackpole Company and designated by them as *G*-1 powder. This powder is the same as the carbonyle type *E* powder except for the particle insulation applied by an unknown Stackpole process. In order not to damage this insulation, no toluene was used in making an ingot from this iron powder. Instead the polystyrene was added to the iron in the form of finely crushed crystals. The two ingredients were dry mixed, and a test ingot made in the manner previously described.

The data in Fig. 3a show the attenuation characteristics of three different size samples made from an ingot consisting of 1.23 ounces of *G*-1 Stackpole iron powder and 0.18 ounce of polystyrene crystals. It is interesting to note that the initial insertion loss is almost directly proportional to the thickness of the sample, but as magnetic saturation is approached this proportionality no longer holds. The reflection properties of these samples are displayed in Fig. 3b. No explanation can be offered for the large values of P.S.W.R. exhibited by sample number seven.

FERROMAGNETIC RESONANCE

Possible ferromagnetic resonance effects were observed with an iron powder sample made from *G*-1 iron powder mixed with a thermo-setting resin. This powder was also obtained from the Stackpole Company and is designated as *G*-1 *MIX*. Since a resin binder was already available in this powder, it was not necessary to add any polystyrene in making the ingot. The attenuation and reflection characteristic of a test sample (0.063″ thick) was measured at two different wavelengths, and with the magnetic field applied in the "*a*−*a*" and the "*b*−*b*" direction. The performance of this sample when the magnetic field is applied in the "*a*−*a*" direction is shown in Fig. 4. For this direction of the magnetic field a pronounced peak can be observed in the attenuation characteristics. Such peaks are indicative of resonance absorption of microwave energy.

Kittel[5] has shown that for ferromagnetic resonance, the magnetostatic field applied normal to the magnetic

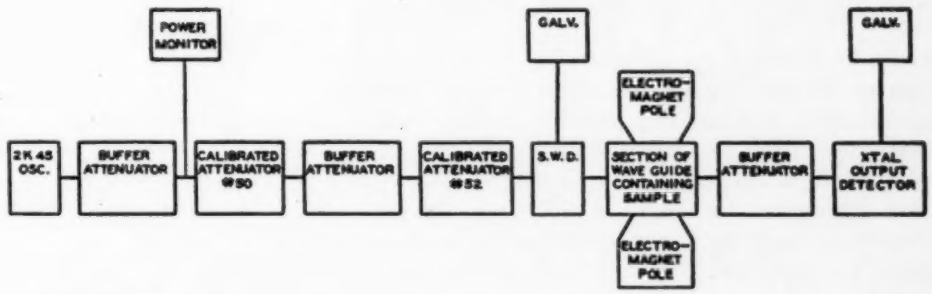

FIG. 1. Block diagram of wave guide apparatus.

[5] Charles Kittel, "Ferromagnetic resonance absorption," Phys. Rev. **73**, 155 (1948).

component of the microwave field must satisfy the following condition:

$$\omega_0=\gamma\{[H_z+(N_y-N_z)M_z]\times[H_z+(N_x-N_z)M_z]\}^{\frac{1}{2}},$$

where ω_0=angular microwave frequency; H_z=magnetostatic field strength; M_z=component of magnetization vector parallel to magnetostatic field; N_x, N_y, N_z =demagnetizing factors of sample in guide; and γ=electron spin gyromagnetic ratio ($\gamma/2\pi=2.80$ megacycles/oersted). Because of the difficulties involved in calculating proper values for the demagnetizing factors, and the uncertain assumptions that would have to be made in assigning a value to M_z, it is impractical to attempt to compute the resonant frequency condition for the iron powder sample. However from Fig. 4 it may be seen that as the microwave frequency increases the peaks of the attenuation curves occur at greater magnetostatic field strengths. This is at least in qualitative agreement with theory.

The attenuation and reflection characteristics of sample number 16 with the magnetic field applied in the "$b-b$" direction are shown in Fig. 5. No peak or resonance attenuation occurs for this direction of the magnetic field. In comparing Fig. 4 with Fig. 5 one is impressed with the tremendous difference in the reflection characteristics. In designing a magnetically controlled attenuator for which a very low reflection coefficient is desirable, it apparently would be advantageous to apply the magnetic field in the "$a-a$" direction.

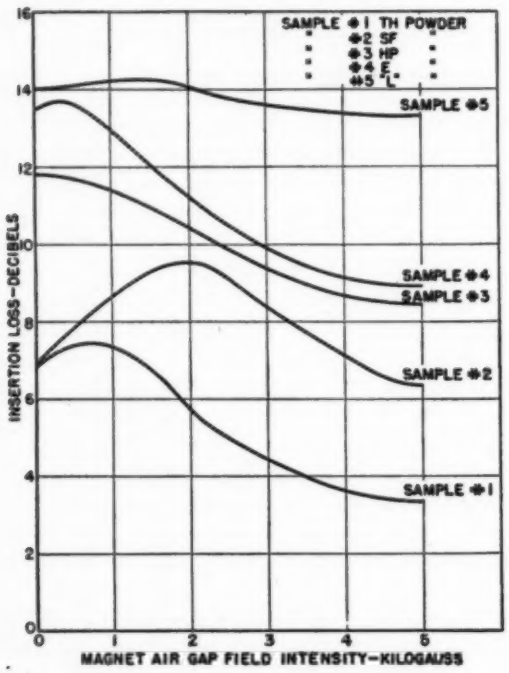

FIG. 2a. Insertion loss of samples made with carbonyle powders.

The static permeability of sample number 16 was measured by the ballistic galvanometer method[6] and found to be equal to 1.80.

EXPERIMENTS WITH PERMALLOY POWDER

Several samples were made from 3 micron diameter Permalloy powder obtained from the Inter Chemical Corporation of New York. These samples were cut from ingots made by introducing the iron powder into dissolved polystyrene as previously described. The attenuation and reflection characteristic of two of these samples are shown plotted in Fig. 6. The magnetic field was applied in the "$b-b$" direction. Sample number 10 was made from an ingot consisting of 1.23 ounces of Permalloy and 0.18 ounce of polystyrene; sample number 11 was cut from an ingot consisting of 0.50 ounce of Permalloy and 0.15 ounce of polystyrene. Because of the comparatively steep slopes of the attenuation curves, these samples appear to make the most effective magnetically controlled attenuators. This probably can be attributed to the high initial permeability of Permalloy powder which saturates at relatively small magnetizing field strengths.

THEORETICAL CONSIDERATIONS

At microwave frequencies a low conductivity dielectric loaded with ferromagnetic materials will exhibit a complex dielectric constant and a complex permeability.[7] This section of the paper will consider the theoretical power loss experienced by a TE_{01} wave propagating through a section of wave guide filled with

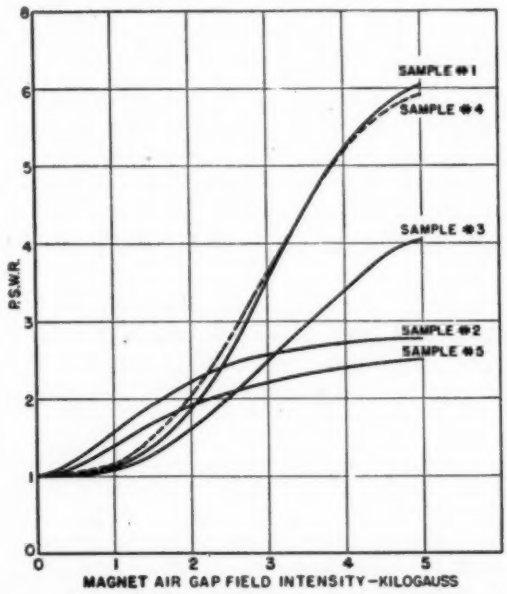

FIG. 2b. Reflection characteristics of samples made with carbonyle powders.

[6] Page and Adams, *Principles of Electricity* (D. Van Nostrand and Company, Inc., New York, 1931).

[7] J. B. Birks, "Measurement of the permeability of magnetic oxide materials at centimeter wave-lengths," Nature **158**, 671 (1946).

a loaded dielectric material. In view of the assumptions that must be made, acceptable correlation is obtained between the theoretical and the measured loss values.

Maxwell's equations for a wave traveling in a medium exhibiting complex electrical constants become in m.k.s. units

$$\left.\begin{aligned} \nabla\times\bar{E} &= -(\mu_1+i\mu_2)\partial H/\partial t \\ \nabla\times\bar{H} &= (\epsilon_1+i\epsilon_2)\partial E/\partial t \\ \nabla\cdot(\mu_1+i\mu_2)\bar{H} &= 0 \\ \nabla\cdot(\epsilon_1+i\epsilon_2)\bar{E} &= 0 \end{aligned}\right\}, \qquad (1)$$

where the subscripts 1 and 2 denote, respectively, the real and imaginary parts of the permeability and dielectric constant. Because of the extremely low conductivity of the medium under consideration, the conduction current term in Maxwell's equations may be neglected.

A solution of the wave equation, and application of the boundary conditions for a wave guide excited in the TE_{01} fundamental mode, yields the following definitions for the electric and magnetic field components of a wave traveling along the Z direction

$$Ey = Ke^{-\alpha Z}\sin(\pi x/b)\cos(\omega t-\beta Z)$$

$$H_x = -K\frac{(\mu_1-i\mu_2)e^{-\alpha Z}}{(\mu_1^2+\mu_2^2)b\omega}\sin\frac{\pi x}{b} \times\{\beta\cos(\omega t-\beta Z)+\alpha\sin(\omega t-\beta Z)\}$$

$$H_Z = \frac{-K\pi(\mu_1-i\mu_2)e^{-\alpha Z}}{(\mu_1^2+\mu_2^2)b\omega}\cos\frac{\pi x}{b}\sin(\omega t-\beta Z)$$

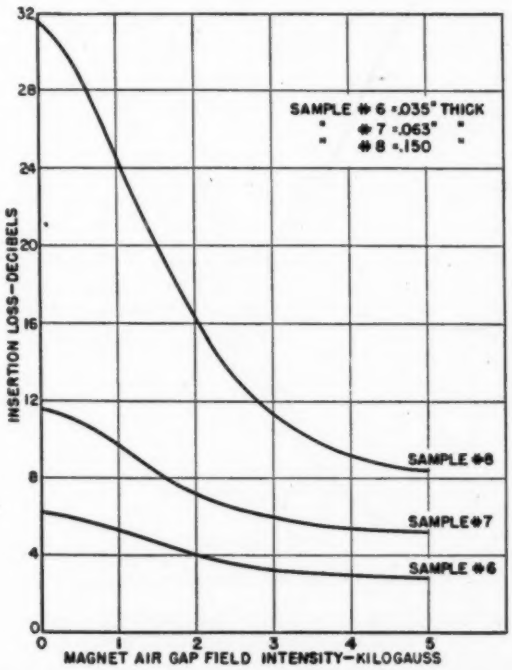

FIG. 3a. Insertion loss of three different size samples made with stackpole G-1 iron powder.

where b is the wave guide dimension along the x direction (broad dimension). The propagation constant $\gamma=\alpha+i\beta$ evaluates to

$$\gamma=[(\pi^2/b)-\omega^2(\mu_1+i\mu_2)(\epsilon_1+i\epsilon_2)]^{\frac{1}{2}}.$$

Separation of the real and imaginary parts leads to the following expressions for the attenuation constant and phase constant.

$$\alpha=[(\{\pi/b\}^2-\omega^2\{\mu_1\epsilon_1-\mu_2\epsilon_2\})^2 +(\omega^2\{\mu_2\epsilon_1+\mu_1\epsilon_2\})^2]^{\frac{1}{4}}\cos(\theta/2),$$

$$\beta=[(\{\pi/b\}^2-\omega^2\{\mu_1\epsilon_1-\mu_2\epsilon_2\})^2 +(\omega^2\{\mu_2\epsilon_1+\mu_1\epsilon_2\})^2]^{\frac{1}{4}}\sin(\theta/2),$$

where

$$\theta=\arctan\left(\frac{\omega^2\{\mu_2\epsilon_1+\mu_1\epsilon_2\}}{\{\pi/b\}^2-\omega^2\{\mu_1\epsilon_1-\mu_2\epsilon_2\}}\right). \qquad (2)$$

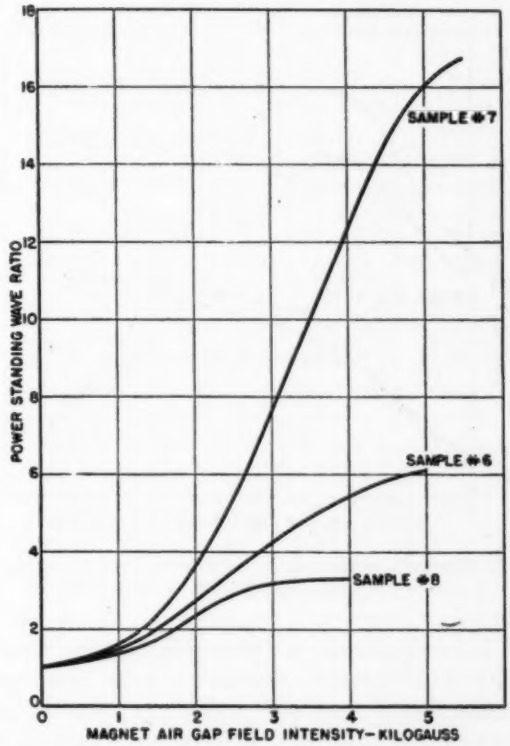

FIG. 3b. Reflection characteristics of samples made with stackpole G-1 iron powder.

The total instantaneous power flowing through the guide at any point may be obtained by integrating the Poynting vector over the cross-sectional area of the guide. Thus

$$Pi=\int_0^{x=b}\int_0^{y=a}(\bar{E}\times\bar{H})dxdy.$$

Substituting Ey and Hx for $\bar{E}$ and $\bar{H}$, and averaging by integrating over a complete time period, the average

power flow across a section of guide evaluates to

$$P=\frac{-K^2e^{-2\alpha Z}\mu_1\beta a\cdot b}{4(\mu_1^2+\mu_2^2)}.$$

"a" is the wave guide dimension in the y direction. Establishing the ratio of the average power at point Z to the average power at point $(Z+1)$ meters

$$P_Z/[P_{(Z+1)}]=e^{2\alpha}.$$

Converting this power ratio to decibels

$$\text{db}=(10/2.3)\log_e e^{2\alpha}.$$

Thus the decibel power loss per meter length of guide may finally be written as

$$\text{db}=20/2.3[(\{\pi/b\}^2-\omega^2\{\mu_1\epsilon_1-\mu_2\epsilon_2\})^2+(\omega^2\{\mu_2\epsilon_1+\mu_1\epsilon_2\})^2]^{\frac{1}{2}}\cos(\theta/2), \quad (3)$$

where θ is given by Eq. (2).

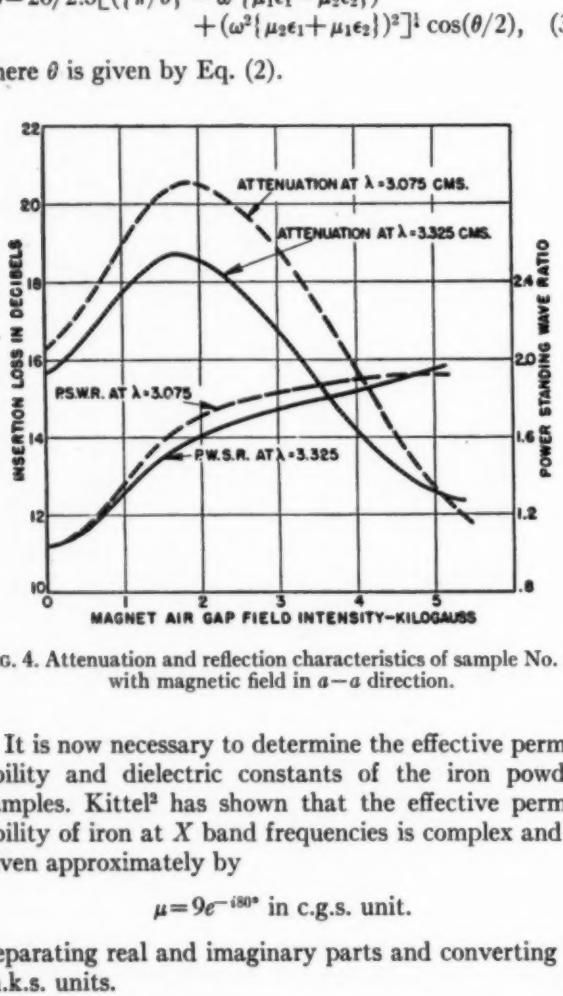

FIG. 4. Attenuation and reflection characteristics of sample No. 16 with magnetic field in $a-a$ direction.

It is now necessary to determine the effective permeability and dielectric constants of the iron powder samples. Kittel[2] has shown that the effective permeability of iron at X band frequencies is complex and is given approximately by

$$\mu=9e^{-i80^\circ} \text{ in c.g.s. unit.}$$

Separating real and imaginary parts and converting to m.k.s. units.

$$\mu_1=1.96\times10^{-6} \text{ henry/meter}$$
$$\mu_2=11.1\times10^{-6} \text{ henry/meter.}$$

A typical handbook value for the dielectric constant of polystyrene at X band frequencies is

$$\epsilon_1=21.7\times10^{-12} \text{ farad/meter,}$$
$$\epsilon_2=1.06\times10^{-14} \text{ farad/meter.}$$

From theoretical considerations based on scattering of an electromagnetic wave from spherical particles imbedded in a non-conducting medium, Lewin[8] derives the following formulas for the bulk constants of a loaded dielectric.

$$\epsilon_m=\epsilon_d[1+(3f/1-f)]$$

$$\mu_m=\mu_d\left(1+\frac{3f}{(\mu_p-2\mu_d)/(\mu_p-\mu_d)-f}\right)$$

where ϵ_m=dielectric constant of loaded dielectric; ϵ_d=dielectric constant of dielectric only; μ_m=permeability of loaded dielectric; μ_d=permeability of dielectric only; μ_p=permeability of iron particles at frequency under consideration; and f=ratio of volume of particles to total volume of mixture=0.504 for samples shown in Fig. 2a. Substituting the given values for the parameters in Lewin's formulas, and treating the real and imaginary parts separately, there are obtained the following values for the bulk constants of the loaded dielectric.

$$\epsilon_1=91.8\times10^{-12} \text{ farad/meter,}$$
$$\epsilon_2=4.48\times10^{-14} \text{ farad/meter,}$$
$$\mu_1=1.59\times10^{-6} \text{ henry/meter,}$$
$$\mu_2=3.54\times10^{-6} \text{ henry/meter.}$$

Substituting these constants into Eq. (3) and neglecting the possibility of ferromagnetic resonance, the loss

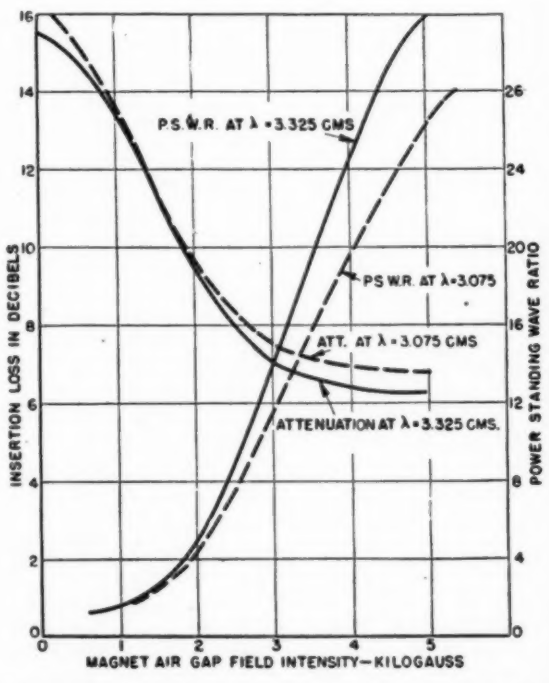
P.S.W.R. AT λ=3.325 CMS
P.S.W.R. AT λ=3.075
ATT. AT λ=3.075 CMS
ATTENUATION AT λ=3.325 CMS.
INSERTION LOSS IN DECIBELS
POWER STANDING WAVE RATIO
MAGNET AIR GAP FIELD INTENSITY—KILOGAUSS

FIG. 5. Attenuation and reflection characteristics of sample No. 16 with magnetic field in $b-b$ direction.

[8] L. Lewin, "The electrical constants of a material loaded with spherical particles," J. Inst. Elec. Eng. **94**, 65 (1947).

in the loaded dielectric becomes

Power loss = 7.91 decibels per millimeter (at zero magnetizing field).

Assuming that for magnetic saturation the real and imaginary parts of the effective permeability decrease to that corresponding to free space, and that the dielectric constant of the loaded dielectric is not a function of the magnetic field, the power loss may be computed under conditions of magnetic saturation and compared to some of the experimental curves shown in Fig. 2a. The loss at magnetic saturation evaluates to 5.89 decibels per millimeter. The sample thickness equals 1.6 millimeters. Consequently the computed loss without a magnetostatic field is 12.65 db and the computed loss at magnetic saturation is 9.32 db. These loss values may be compared to the measured values for sample number 3 in Fig. 2a which has an initial insertion loss of 11.8 db and a magnetic saturation loss of 8.4 db.

It is interesting to note that in most cases the theory predicts rather accurately the difference between the initial and minimum insertion loss values for the samples shown in Fig. 2a.[9] The most striking deviation from the value predicted by the theory occurs with sample No. 2. This may be caused by ferromagnetic resonance which might sustain the permeability at large magnetostatic field strengths.

The inability of the theory to determine the initial insertion loss for all of the samples, stems from the fact that the actual radii of the iron particles does not enter into Lewin's formulas—only the volume concentration.[10] If sufficient data were available it might be possible to compute an empirical constant which would take into consideration the variation in particle size. However such factors as sample homogeneity, particle geometry, and particle isolation would also have to be considered.

[9] The measurements made with sample number 5 cannot be compared with the theory because for this sample the iron particle size is several times greater than the skin depth at the frequency under consideration, and therefore only a small portion of the iron is effective in controlling the attenuation.

[10] Another factor not considered in the theory is the power loss associated with the circulating currents in the matching section. However measurements indicate that the maximum matching loss for any of the samples considered in Fig. 2a is only about 0.4 db.

CONCLUSION

The attenuators described in this paper require very large magnetizing forces of the order of five thousand ampere turns, and for this reason are not too well suited for practical applications. However, some work has been done toward reducing the strength of the required magnetic field, and several attenuators and amplitude modulators have been developed which require less than 1000 ampere turns of magnetizing force. It is planned to report on these attenuators in the near future.

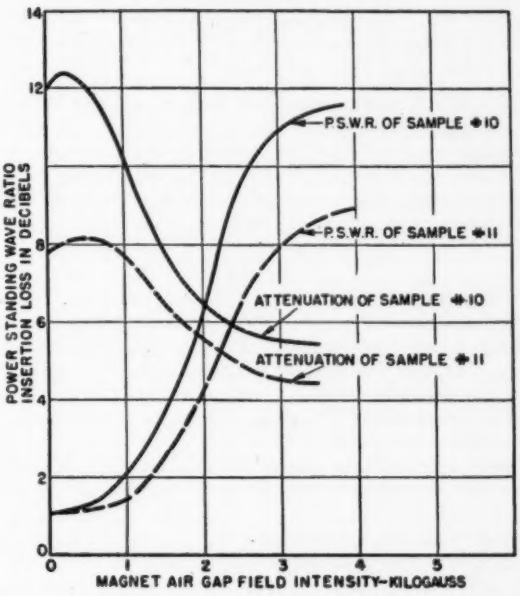

FIG. 6. Attenuation and reflection characteristics of samples made with Permalloy powder.

The author wishes to express his appreciation for the cooperation displayed by Mr. Moore of the General Aniline and Film Company in supplying many of the carbonyle powders used in the experiments. Acknowledgment must be made of the effective assistance of Mr. R. H. Webb* who helped procure much of the experimental data presented here. Thanks are also due Mr. M. A. Schultz* for his encouragement and interest in this investigation, and to Dr. D. K. Coles* for helpful discussions and theoretical interpretations of the data.

* Westinghouse Research Laboratories, East Pittsburgh, Pennsylvania.

Letters to the Editor

Electron Emission and Conduction Mechanism of Oxide-Coated Cathodes

R. Loosjes and H. J. Vink
Philips Research Laboratories, Eindhoven, Netherlands
June 10, 1949

In a recent article, Mahlman[1] encounters some difficulties in explaining his results on the basis of the assumption that an oxide-coated cathode can be treated as an excess-semiconductor. Some time ago we proposed[2] a conduction mechanism, of the oxide-coated cathode, which, we think, offers an explanation of the fact that according to his measurements

$$\varphi_{\text{thermion.}}+\tfrac{1}{2}E>\varphi_{\text{photoelectr.}},$$

$\frac{1}{2}E$ being the activation energy of the conductivity.

In our theory particular stress is laid on the fact that an oxide coating is an electron-emitting semiconducting solid with a *porous* character. Because of its electron emission at high temperatures (in particular>800°K), each grain of oxide in the porous coating is surrounded by a cloud of electrons. This means that all pores can be considered as filled with an electron gas the density of which can easily be calculated. On the assumption that the mean free path of these electrons is of the order of magnitude of the average pore diameter (a few microns), a conductivity of an oxide coating can be calculated which is of the same order of magnitude as that actually found in experiments.

It will be understood that the temperature dependence of the density of the electron gas and consequently of the conductivity will be the same as that of the thermionic emission. A calculation showed this to be correct in a first approximation.

Extensive experiments showed that the logσ against$1/T$-curves always had the form reproduced in Fig. 1. The bent is situated at a temperature of about 750°K. An obvious explanation of this form of the curves is that there are two conduction mechanisms in the oxide coating, connected in parallel, one with a low activation energy preponderating under 750°K, the other with a higher activation energy preponderating above 750°K. Because of this connection in parallel it is not allowed to calculate activation energies directly from the slope of one of the parts of the curve in Fig. 1. The true temperature dependence of each conduction mechanism can only be found if one bears in mind that the conductivity experimentally found is the sum of two separate conductivities. A typical example of the activation energies computed on this basis is given in Table I.

The rather good agreement between the values in columns 2 and 4 (compare with those of column 3) is a confirmation of our theory. We suppose the activation energies preponderating under 750°K (column 1) to be those of the conducting grains themselves.

Our explanation of the results of Mahlman is:

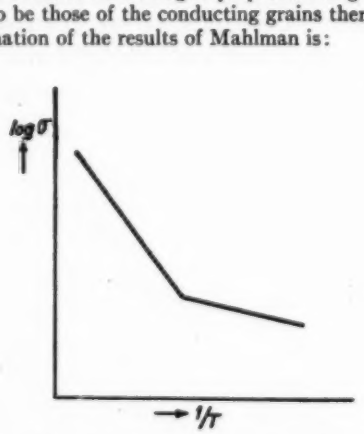

Fig. 1. Logσ, $1/T$—curve for an oxide coating.

Table I. Activation energies and work functions of one oxide-coated cathode in various degrees of activation.

	1 Activation energy preponderating under 750°K Volts	2 Activation energy preponderating above 750°K Volts	3 Apparent activation energy calculated directly from the slope above 750°K Volts	4 Thermionic work function Volts
Increasing detection ↓	0.22	0.98	0.84	1.07
	0.14	1.14	0.60	—
	0.12	1.24	0.54	1.10
	0.11	0.96	0.56	0.90
	0.10	0.96	0.54	1.02
	0.09	0.94	0.48	0.87

(1) That his activation energy of the conductivity is an *apparent* activation energy. The true activation energy will be some tenths of a volt higher as can be seen in Table I. It cannot be estimated from his measurements as he did not extend them below 750°K.

(2) That according to our opinion the true value of $\frac{1}{2}E$ is not 1.2 v but 0.2–0.4 v, as could be estimated from the degree of activation of his cathode and our experimental results. If no allowance is made for the Franck-Condon principle

$$\varphi_{\text{photoelectr.}}=\varphi_{\text{thermion.}}+\tfrac{1}{2}E.$$

As Mahlman found $\varphi_{\text{thermion.}}=1.5$ v, $\varphi_{\text{photoelectr.}}$ would be 1.7 to 1.9 v which is in striking agreement with the 1.8 v he observed. A paper with full details of our investigations is in preparation.[3]

[1] G. W. Mahlman, J. App. Phys. 20, 197 (1949).
[2] H. J. Vink, *Het geleidingsmechanisme in de oxyde-kathode*, thesis, Leiden University, 1948.
[3] To be published in Philips Res. Rep.

Note on Some Plastic Flow Effects in Steel

Orrin H. Clark and Ernest M. Lyman*
Socony-Vacuum Laboratories (A Division of Socony-Vacuum Oil Company, Inc.), Research and Development Department, Paulsboro, New Jersey
June 13, 1949

An application of interference fringe measurements to the study of plastic flow in steel has given some interesting results. In the course of studies of the lubrication of bearing metals, it became important to know the approximate magnitude of the depression existing at the center of a contact circle between two dissimilar steel pins pressed together under load sufficient to induce plastic flow in the softer one. The solution obtained by interference fringe measurements illustrates a method of studying deflections occurring in simple cases of plastic flow and is therefore described briefly.[1]

A photograph of the interference fringe contour map of a residual pit is shown in Fig. 1. The pit was made in a soft (Rockwell $B=90$) steel pin of $\frac{1}{4}$-in. diameter. Another $\frac{1}{4}$-in. steel pin with axis at right angles was pressed into the soft pin under 25 lb. The loading pin was hard (Rockwell $C=64$) and suffered no permanent deformation. The picture was taken with sodium light by laying an optical flat on the pit. A standard metallurgical microscope with vertical illuminator was used.

This contour map of course does not represent conditions under load, because of the elastic recovery. It is convenient in correcting for elastic recovery to consider it as taking place in two stages. The first stage is the shrinkage of the contact circle to the size of the residual pit. That is, under load, the contact circle exceeds the measured pit size by an amount consisting of an annular ring of elastic contact outside this region of permanent deformation. When unloading, the contact area first "peels off" the annular ring of elastic contact, both pins incurring vertical rise at the center in this stage. Further vertical rise takes place during the second stage of removal of the rest of the load.

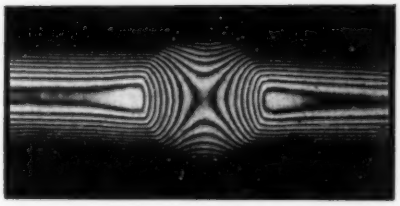

FIG. 1. Fringe pattern in pit left in soft pin after loading with hard pin.

The interference fringes give directly the difference in depth between the center and each edge, after unloading. The edges, however, suffer no vertical recovery during the second stage, since they are under no pressure. During the first stage the rise of the transverse edges can be calculated from the conventional sagittal formula, provided the curvature of the loading pin is not deformed appreciably, so that it may be used to give the arc. The fringes show that the edge depth in the residual pit does, in fact, correspond to the sagittal value given by using the loading pin's radius. Since the elastic contact annulus is very small and carries very little load, it is a good assumption that the curvature of the loading pin at the transverse edges is unchanged throughout.

The figures showing the correspondence of edge depth to the sagittal calculation are as follows.

Counting fringes, it is seen that there is a rise of six fringes from the transverse edges to the center, and a further rise of eight fringes from the center to the axial edges, making a total depth of fourteen fringes. Calculation of the depth of the arc from the measured radius of the loadung pin (0.310 cm) and the pit diameter (0.0315 cm) gives the result 4.00×10^{-4} cm. Each fringe being a depth of 2.95×10^{-5} cm, this corresponds to 13.6 fringes. Hence, the curvature of the pit after unpeeling is the same as the curvature of the loading pin.

It remains to calculate the edge depth under load. For this the diameter of the contact area under load is needed. This diameter was obtained by using Prussian blue as an indicator. Measurements on fresh pins gave a value of 1.051 for the ratio of total contact diameter to the diameter of the residual pit. Applying this ratio, the contact diameter under load was 1.051×0.0315 cm, or 0.0332 cm. The edge depth was then, by saggital formula, 4.45×10^{-4} cm. The center depth, after unloading, has been seen to be eight fringes, or 2.36×10^{-4} cm. The difference, 2.09×10^{-4} cm, consists of two parts, namely, the central elastic recovery of the soft pin when unloaded plus the central elastic deflection of the hard pin under load. These two parts are the vertical elastic displacements of two similarly shaped pins under the same load, having the same elastic properties, differing somewhat, however, in the stress distributions away from the contact surface. If these elastic displacements are assumed equal, the desired elastic recovery of the center of the soft pin is obtained as 1.05×10^{-4} cm. Under load the depth of the central depression was therefore 3.40×10^{-4} cm.

The necessity of assuming equal elastic deflections for pins of different hardness does not arise in cases where like pins are used. An example of this is illustrated in Fig. 2, which shows the interference fringe pattern obtained when both pins were soft. In this case there is a rise of eleven fringes from the transverse edge to the center and a further rise of four fringes to the axial edge. It is obvious that the seven-fringe asymmetry was equally caused by elastic recovery of each pin, and that therefore the recovery in the second stage of unloading was 3½ fringes, or 1.03×10^{-4} cm. For this combination the pit diameter was 0.0328 cm, and the factor given by Prussian blue measurements for increase due to elastic contact was 1.057. Applying the sagittal formula gives an additional elastic recovery for each pin of 0.28×10^{-4} cm, with a resulting total elastic recovery of 1.31×10^{-4} cm.

In the case of two hard pins, all deformation is elastic and the total elastic deflections are obtained by again applying the sagittal formula. The pit diameter was calculated to be 0.0266 cm from the standard formula of elasticity theory, and three checks with Prussian blue gave measurements of 0.0269, 0.0270 and 0.0270 cm. Using the calculated value, the central elastic deflection turns out to be 1.43×10^{-4} cm for each pin.

Comparing the combined elastic deflections of both pins in the three cases, hard-soft, soft-soft, and hard-hard, we get the values 2.10×10^{-4} cm, 2.62×10^{-4} cm, and 2.86×10^{-4} cm, respectively. Since the hard-soft case would be expected to be intermediate, it appears that the measuring error in the value obtained for elastic deflection in a single pin is of the order of 0.26×10^{-4} cm. This is about the amount of one fringe and is ascribed to uncertainty in matching fringes to the pit edges. While the Prussian blue measurements have little precision, their total contribution is too small to make this a major source of error.

* University of Illinois, Urbana, Illinois.

[1] It is interesting to observe that virtually the identical problem arose in the recent work of Holm, Holm, and Shobert, J. App. Phys. 20, 319–327 (1949). In a study of the theory of hardness, they needed to know the deflections in the case of a ball pressed into a plane. They arrived at a calculated result by assuming that the flattening of the ball and of the plate could each be considered separately and then combined.

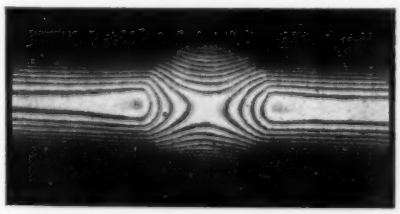

FIG. 2. Fringe pattern in pit left in soft pin after loading with soft pin.

Interpretation of X-Ray Patterns of Cold-Worked Metal*

B. L. AVERBACH AND B. E. WARREN
Massachusetts Institute of Technology, Cambridge, Massachusetts
(July 7, 1949)

WITH modern experimental technique it is possible to measure the shape of a powder pattern line with sufficient accuracy to justify an interpretation based on the shape of the line rather than using just the line breadth. By making full use of the shape of the line it is possible to get a great deal of information about the nature of cold work without making any *a priori* assumptions.

Starting with the same formulation used by Stokes and Wilson[1] we represent the position of cell $m_1m_2m_3$ by

$$Rm_1m_2m_3 = m_1a_1 + m_2a_2 + m_3a_3 + \delta m_1m_2m_3$$

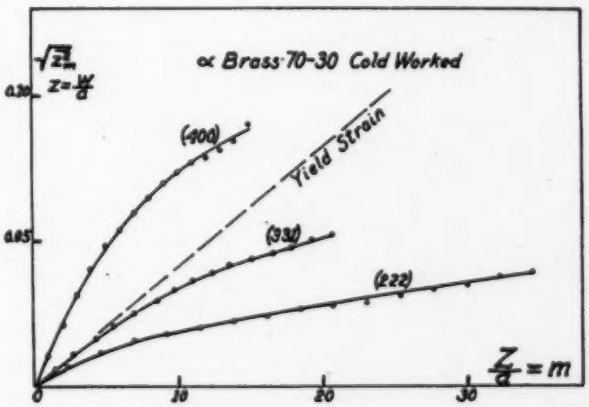

FIG. 1. Relative displacements *vs.* crystal distance from Fourier coefficients for powder lines of cold-worked α-brass.

where δ is an arbitrary displacement. The intensity from one crystal is then

$$I=F^2\sum_{m_1}\sum\sum\sum\sum\sum_{m_2'}\exp\left[\frac{2\pi i}{\lambda}(s-s_0)\cdot(R_m-R_{m'})\right].$$

Let $s-s_0=\lambda(h_1b_1+h_2b_2+h_3b_3)$ where $b_1b_2b_3$ are the reciprocal vectors and $h_1h_2h_3$ are continuous variables. With cubic crystals it is always possible to choose a new set of orthogonal axes so as to make any reflection of the type (00l). The intensity distribution in the (00l) line of a powder pattern is then given by the cosine Fourier series

$$P_{2\theta}=K\sum_{m=-\infty}^{+\infty}A_m\cos 2\pi mh_3 \tag{1}$$

where the variable h_3 is given by

$$h_3=2a_3\frac{\sin\theta}{\lambda},$$

and the coefficients A_m are given by

$$A_m=\langle\cos 2\pi lz_m\rangle_{\substack{Av\\ m_1=m_1'\\ m_2=m_2'}}. \tag{2}$$

If the $2\pi lz_m$ values are small, or if the probability of the z_m values is given by an error curve (2) becomes

$$A_m=\exp\left[-2\pi^2l^2(\bar{z}_m^2)_{\substack{m_1=m_1'\\ m_2=m_2'}}\right]. \tag{3}$$

Using crystal monochromated radiation and a Geiger-counter spectrometer, the intensity distribution in the line (00l) is measured for a cold-worked sample and for an annealed sample. The Fourier coefficients A_m, relating to cold-work broadening only, are then readily obtained from the two curves by the method of Stokes.[2] From each coefficient A_m, a value of $\bar{z}_m^2$ is computed using Eq. (3). Consider two unit cells $m_1m_2m_3$ and $m_1'm_2'm_3'$ with $m_1=m_1'$, $m_2=m_2'$ and $|m_3-m_3'|=m$. The distance between these cells is ma_3 and the component along a_3 of the relative displacement of the two cells is z_ma_3. The quantity $(\bar{z}_m^2)_{\substack{m_1=m_1'\\ m_2=m_2'}}$ is an average over all such pairs of cells. If strains in the material are uniform over large regions, a plot of $(\bar{z}_m^2)^{\frac{1}{2}}$ against m should give a straight line whose slope is the root-mean-square strain. Figure 1 shows results for 70–30 α-brass filings. The initial slopes give the true root-mean-square strains in the corresponding directions. It is evident that they are very closely in an inverse ratio to the corresponding values of Young's modulus, indicating that the root-mean-square stress is approximately isotropic.[3] The average initial slope is very close to the macroscopic yield strain for 70–30 brass. The departure of the curves from linearity offers a promising method for studying the non-uniformity of strains over regions of appreciable size and demonstrating the highly localized nature of the strains in cold-worked metal.

A treatment of powder pattern lines in terms of the Fourier coefficients A_m offers a very general and powerful method for handling cold-work broadening, particle-size broadening, and many other effects. A plot of A_m against m will distinguish between cold-work broadening and particle-size broadening. For a substance in which there is particle-size broadening only, the initial slope of the A_m *vs.* m curve gives an average particle size and the second derivative of the curve gives directly a size distribution. The integral breadth of a line β is given by

$$\beta=\frac{1}{\sum A_m}$$

and hence a measurement of line breadth gives only a small part of the information contained in the full set of Fourier coefficients.

* Experimental work supported by the ONR under Contract N5 ori-07832.

[1] A. R. Stokes and A. J. C. Wilson, Proc. Camb. Phil. Soc. **38**, 313 (1942); Proc. Phys. Soc. **56**, 174 (1944).
[2] A. R. Stokes, Proc. Phys. Soc. **61**, 382 (1948).
[3] C. S. Smith and E. E. Stickley, Phys. Rev. **64**, 191 (1943).
[4] Stokes, Pascoe, and Lipson, Nature **151**, 137 (1943).

Zirconium Carbide as a Thermionic Emitter

R. E. Haddad, D. L. Goldwater, and F. H. Morgan
Cathode Research Group, Bartol Research Foundation of the Franklin Institute, Swarthmore, Pennsylvania

June 6, 1949

As part of a broad program of investigation, the thermionic emitting properties of zirconium carbide are being studied. The zirconium carbide is cataphoretically coated onto tungsten wire and the cathode is then mounted in a guard-ringed diode. Values of A and b are obtained for the Richardson equation $I_s=AT^2\epsilon^{-b/T}$, ($b=11{,}605\phi$). First results yield values of $\phi=2.1(6)$ v,

$$A=0.2-0.5 \text{ amp./deg. K}^2/\text{cm}^2.$$

Two interesting values of the space-charge limited emission available are: at 1500° C_b, at least 0.6 amp./cm² d.c., at 1700°C_b, 6 amp./cm² pulsed.

In a subsidiary experiment, the spectral emissivity of zirconium carbide has been obtained for temperatures up to 1800°C, and at a wave-length of 0.655μ. The value obtained is 0.96 ± 0.04. Brightness temperatures given above can hence be regarded as true values.